# Resolving Local Magnetization Structures by Quantitative Magnetic Force Microscopy

Von der Fakultät Maschinenwesen

der

Technischen Universität Dresden

zur

Erlangung des akademischen Grades

Doktoringenieur (Dr.-Ing.)

angenommene Dissertation

von

Dipl.-Ing. **Silvia Vock**

(geb. Sasvári)

geboren am 01. Januar 1980 in Löbau

2014

Gutachter 1: Prof. Dr. Ludwig Schultz (TU Dresden und IFW Dresden)
Gutachter 2: Prof. Dr. Manuel Vázquez (CSIC, Madrid, Spanien)

Eingereicht am: 25.11.2013

Tag der Verteidigung: 09.05.2014

...Ich selbst sehe die Physik lieber als eine Sammlung von theoretischen Modellen. Sie beschreiben die Landschaft, sind aber nie die Landschaft selbst. Endgültige Antworten liegen darum schlicht außerhalb unserer Reichweite...

---

*Tony Rothman [Rot12]*

# Contents

# Introduction

The ingredients are remarkably simple: two interacting magnets, a scanner to move one of them and a computer to map the spatially resolved attractive or repulsive interaction. These basic components of a Magnetic Force Microscope (MFM) open up the possibility for studying the physics of magnetic materials on a nanometer scale.

The continuously growing demand for higher storage densities in magnetic recording technology increased the interest in magnetic properties of nanoobjects. The exploration of fundamental phenomena of these objects enabled the rapid development in the computer industry in the last decade. Consequently, the investigation in reduced dimensions requires magnetic imaging methods with very high resolution. Advanced techniques like the Differential and Holographic Transmission Electron Microscopy or the Polarized Scanning Electron Microscopy can achieve resolutions down to less than 10 nm. However, the complexity of the equipment and the time consuming sample preparation are major disadvantages of these methods [Por98].

In MFM several advantages for a standard usage add up. These are the simple instrumentation under ambient conditions, one of the highest resolution achievable in magnetic imaging, applicability to a variety of materials, low requirements concerning sample preparation, the possibility to study magnetic field and temperature dependent effects and finally its depth sensitivity with the prospect of three-dimensional imaging.

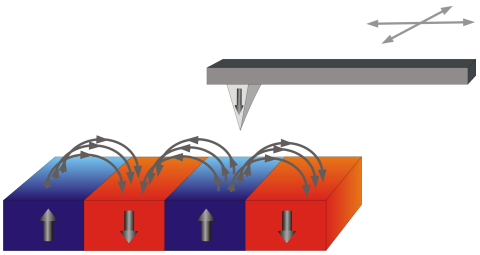

**Figure 0.1:** Scanning a magnetic probe over a domain pattern results in a position dependent repulsive or attractive force acting on the tip.

MFM belongs to the family of scanning probe techniques. The starting point for the development of various kinds of such techniques was set by Binning and Rohrer (Nobel prize for physics in 1986) in 1982 with the invention of the scanning tunneling microscope [Bin82]. These methods have in common, that they scan the surface of a sample with a probe and detect the interaction between them. Depending on the origin of interaction various kinds of chemical and physical properties with a resolution from 100 µm down to 10 pm can be acquired [Mey04].

The main idea of a MFM experiment is the imaging of a magnetic domain pattern by detecting the magnetostatic interaction between a magnetic tip and the magnetic sample (Figure 0.1). While the pure visualization of domains is relatively simple and straightforward, the quantitative deduction of the sample's magnetization configuration requires numerous additional considerations. The measured contrast in MFM is always influenced by the properties of the magnetic tip. Thus, the aim of quantitative MFM is to eliminate the tip effect from the acquired image and to reveal the underlying magnetic structure and magnetization strength of the sample.

There are several ways to obtain quantitative information from MFM images. In principle, the approaches can be divided into two groups. One is using simple parameterized models to describe the tip effect and the other one is based on a parameter free, global description of the real tip. The latter one has been introduced in the framework of a Fourier transform approach by the group of *Hug et al.* [Hug98, vS00]. However, the method is still not a standard practice since the numerical implementation remains challenging.

In this work both, a model based approach and a Fourier transform approach for quantitative magnetic imaging will be applied to reconstruct the underlying magnetization structure in different materials. First, an introduction to both methods will be given in Chapter 3. Based on the theory elaborated by *Hug et al.* a tip calibration procedure and a numerical deconvolution algorithm have been developed in the present work. This enables the characterization of different kind of MFM tips and conclusions on the resolution limit in MFM experiments.

Recently, iron filled carbon nanotubes (Fe-CNT) have been introduced as suitable probes for MFM imaging [Win06]. In Chapter 4 it will be shown that these probes, in contrast to commercially available standard MFM tips, can be well approximated by a magnetic monopole. This enables easy and straightforward quantitative imaging and further application to multi-component magnetic stray field detection.

Chapter 5 focuses on the identification of magnetic object sizes as an important application of the developed deconvolution approach. Two very different physical problems are addressed in this chapter: the diameter evolution of bubble domains in a Co/Pd multilayer and the characterization of an iron pnictide superconductor by means of the magnetic penetration depth.

The last chapter is devoted to a comprehensive characterization of CoFe nanowire arrays on a local and global scale. Such nanowire arrays are very suitable systems to study magnetostatic interactions in a nanoparticle system. A theoretical derivation of the present interaction fields is given and the results are compared to currently used models.

The experimental investigation of the local magnetization structure with the developed deconvolution method aims to a three-dimensional reconstruction of the magnetization structure at the ends of the individual nanowires embedded in the array. A statistical analysis of MFM measurements in an external field gives insight into the switching behavior of individual nanowires.

# 1 Contrast formation in Magnetic Force Microscopy

Magnetic Force Microscopy probes the interaction between a magnetic tip and a magnetic sample by detecting the deflection of the cantilever to which the tip is attached. To understand the contrast formation in MFM in detail, it is necessary to have a closer look on the present interaction forces and mutual interaction mechanisms between tip and sample during the imaging process. Beside the magnetic interactions a variety of other forces are present, when bringing two solids, like the probe and the sample, in close proximity. The characteristics of these interactions will be introduced in the first section of this chapter.

The magnetostatic description of the tip-sample system is fundamental for the understanding of contrast formation in MFM. Stray field calculation of magnetic volumes as well as the concept of magnetic charges will be the topics of the second section of this chapter.

As an important tool for the handling of stray fields, magnetic charges and interaction integrals, the Fourier transformation of these quantities will be described. The formulation of several magnetostatic laws simplifies enormously in the frequency space and will therefore appear in several parts of this thesis.

## 1.1 Type of interactions

### 1.1.1 Relevant interaction forces

Interactions relevant for an MFM experiment are those, which manifest themselves in a deflection of the cantilever to which the magnetic tip is attached. The origin of the force acting on the cantilever is strongly depending on the distance between probe and sample. A simple model to describe the interaction between two neutral atoms as a function of distance is the Lennard-Jones-potential

$$V_{LJ} = 4\epsilon \left[ \frac{\sigma}{r^{12}} - \frac{\sigma}{r^6} \right] \tag{1.1}$$

where $\epsilon$ is the depth of the potential well and $\sigma$ is the distance, where the interaction becomes zero. Even though this potential is limited to the case of pairwise interaction of atoms, it helps to understand the origin of the dominating forces in different operation modes in scanning force microscopy (details on this are given in Chapter 2). The characteristic form of the Lennard-Jones-potential is given in the diagram in Figure 1.1 (a) (green curve).

The $r^{-12}$ term describes the repulsive short-range interaction, when the probe atoms start to penetrate the sample surface. The repulsion has two origins. One is the Coulomb repulsion, due to the incomplete screening of nuclear charges caused by overlapping electron clouds. The second is the Pauli repulsion originating from the exclusion principle, according to which the electrons can only overlap when the energy of one electron is increased [Grü92]. This type of interaction is applied for topographic imaging of surfaces in the so-called contact mode in atomic force microscopy (AFM).

The $r^{-6}$ term dominates at large separations, typically of the order of several nanometers and leads to a decreasing negative potential and with this to an attractive interaction. The origin of this term is the van der Waals force, which is ever present in any environmental situation [Har90, Har91]. In the distance range, where the attractive force is dominant and large enough, the topography can be measured by non-contact AFM.

Short- and long-range interactions are always present, when bringing solids in sufficiently close proximity. Depending on the material involved in the experiment, other interaction potentials can superimpose the Lennard-Jones-potential. The electrostatic potential occurs between electric charges on the probe and the sample. Since in an MFM experiment these are unwanted effects, the electrostatic interaction is compensated by applying a bias voltage to the tip. In the case of a sample composed of different materials with one material

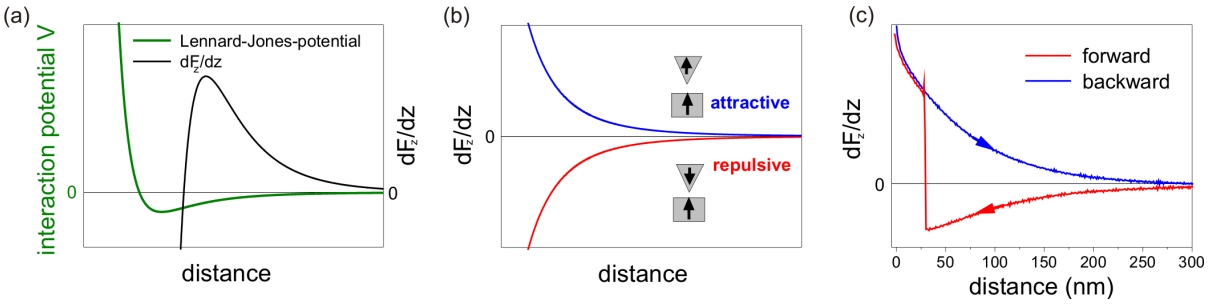


**Figure 1.1:** (a) Lennard-Jones potential (green) and its inverted second derivative giving $\frac{dF_z}{dz}$ (black) (b) Force gradients calculated for pure magnetic interaction in the repulsive (red) and attractive (blue) case. (c) Experimentally measured $\frac{dF_z}{dz}$-distance-curves at the same location, while approaching (red, forward) and withdrawing (blue, backward) from the surface.

being an insulator, a single bias voltage can not compensate the interaction on the whole

measurement region. In this case it is necessary to cover the sample with a conductive layer to enable charge equalization.

The interaction of interest for MFM is the long-range magnetic interaction. It is created by forces acting on the magnetic dipoles contained in the ferromagnetic material of the tip and the magnetic field produced by the magnetic sample. These interactions become dominant at larger distances, when short range interactions, such as the van der Waals interaction, fade out. In an MFM experiment usually force gradients $\frac{dF_z}{dz}$ are detected (the reason for this is explained in Subsection 2.1.2). Therefore the second derivative of the potential has to be considered (black curve in Figure 1.1 (a)). Magnetic interactions can be of attractive or repulsive type resulting in a positiv or negative $\frac{dF_z}{dz}$, respectively. Typical force gradients caused by pure magnetic interaction as a function of distance between tip and sample are shown in Figure 1.1 (b).

In the experimental situation magnetic and Lennard-Jones-type interactions are superimposed. In Figure 1.1 (c) measured $\frac{dF_z}{dz}$-distance curves are shown, where the magnetic tip is first approached (red curve) and then retracted (blue curve) from the sample surface. In this case, the interaction changes abruptly from repulsive to attractive during the approach, which means presumably the tip magnetization has switched into the opposite direction. The backward (blue) curve thus reveals a continuous attractive interaction.

### 1.1.2 Magnetic interaction mechanisms

The interaction of two magnetic volumes in close proximity can have different characteristics. Three categories can be separated [Hub98, Mey04]:

- **Negligible interactions: charge contrast.** There is no influence of the tip on the sample magnetization and vice versa. In this case the distribution of the stray field of the sample does not change depending on tip-sample distance.
- **Reversible modification: susceptibility contrast.** The probe and the sample magnetization can not be considered as rigid and therefore the tip magnetization can be influenced by the sample stray field and vice versa.
- **Strong interactions: hysteresis effects.** This type of interaction occurs if the stray field of the sample is so strong that it leads to irreversible modifications of the tip magnetization and vice versa.

Examples for charge contrast and hysteresis effects are given in Figure 1.2. The sample is a hard magnetic SmCo bulk material with a large domain size in the micrometer range. Applying a probe with a highly coercive coating with $\mu_0 H_c$ in the range of 500 mT (Asylum

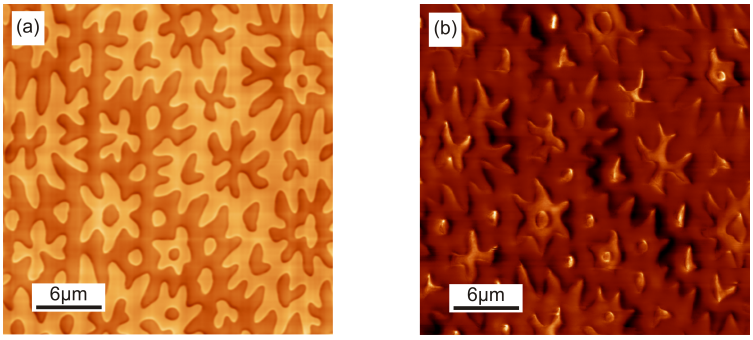


**Figure 1.2:** MFM images of a SmCo polycrystal of a grain with the anisotropy axis aligned perpendicular to the image plane measured with (a) a highly coercive tip and (b) a standard MFM tip with low coercivity.

Research, trade name: ASYMFMHC) enables the imaging with negligible interactions (see Figure 1.2 (a)). With tip and sample both being magnetized along the z-direction (perpendicular to the measurement plane) the image shows the typical domain contrast, where the up and down domains appear as plane bright and dark areas and are separated by a sharp transition. Figure 1.2 (b) illustrates the case of reversible modification within the tip acquired with a standard MFM tip with $\mu_0 H_c$ in the order of 30 mT (Nanosensors, trade name: MFMR). The resulting image shows almost no contrast difference between oppositely magnetized domains, while domain transitions appear pronounced. Due to the strong sample stray fields and low tip coercivity the tip always switches its magnetization in field direction and thus an attractive interaction is detected on top of both domain types. The only contrast is observed at domain transitions.

While the susceptibility contrast still allows a stable and reproducible imaging, the hysteresis contrast depends on the tip position history and leads, in general, to hardly analyzable images [Hub98]. Also the description of the reversible modifications is very challenging and largely unexplored [Hub98, vS00, Gar01]. Thus, in order to perform straightforward quantitative image analysis it is useful to avoid perturbations of any kind. A method which allows to judge the strength of tip-sample perturbations is presented in Section 3.6.

## 1.2 Basic magnetostatics of the tip-sample system

### 1.2.1 General magnetostatic expressions

A hard ferromagnetic volume possesses a fixed magnetization $\mathbf{M}(\mathbf{r})$. Starting from Maxwell's equations the stray field created by such a volume can be derived. The basic equa-

tions of magnetostatics in the absence of currents are [Jac75]:

$$\nabla \cdot \mathbf{B} = \nabla \cdot \mu_0(\mathbf{H} + \mathbf{M}) = 0 \tag{1.2}$$

and

$$\nabla \times \mathbf{H} = 0 \tag{1.3}$$

where $\mathbf{B}$ is the magnetic induction, $\mu_0$ the vacuum permeability and $\mathbf{H}$ the magnetic stray field. From equation (1.3) it follows that $\mathbf{H}$ has a scalar potential $\phi$ such that

$$\mathbf{H} = -\nabla\Phi. \tag{1.4}$$

Together with equation (1.2) this leads to the Poisson equation

$$\nabla^2\Phi = -\nabla \cdot \mathbf{M}, \tag{1.5}$$

which has the following solution for $\Phi$ in real space [Jac75]

$$\Phi(\mathbf{r}) = -\frac{1}{4\pi} \iiint \frac{\nabla' \cdot \mathbf{M}(\mathbf{r}')}{|\mathbf{r} - \mathbf{r}'|} \mathrm{d}^3\mathbf{r}'. \tag{1.6}$$

A real ferromagnetic material is bounded by a surface. Assuming a jump of $\mathbf{M}(\mathbf{r})$ to zero at the surface, the previous equation has to be extended such that [Jac75]:

$$\Phi(\mathbf{r}) = -\frac{1}{4\pi} \iiint \frac{\nabla' \cdot \mathbf{M}(\mathbf{r}')}{|\mathbf{r} - \mathbf{r}'|} \mathrm{d}^3\mathbf{r}' + \frac{1}{4\pi} \iint \frac{\mathbf{n}' \cdot \mathbf{M}(r')}{|\mathbf{r} - \mathbf{r}'|} \mathrm{d}^2\mathbf{r}' \tag{1.7}$$

where $\mathbf{n}$ is the outward directed surface normal of the sample. The integration in the first part is performed over the volume and in the second part over the surface of the ferromagnet. This equation constitutes a general description of the magnetic potential of arbitrary ferromagnetic volumes. Applying equation (1.4) and defining so called volume ($\rho$) and surface magnetic charges ($\sigma$) by

$$\rho = -\nabla \cdot \mathbf{M} \tag{1.8}$$

$$\sigma = \mathbf{n} \cdot \mathbf{M} \tag{1.9}$$

it follows for the stray field of ferromagnetic volumes [Mey04]

$$\mathbf{H}(\mathbf{r}) = -\frac{1}{4\pi} \iiint \rho(\mathbf{r}') \frac{\mathbf{r} - \mathbf{r}'}{|\mathbf{r} - \mathbf{r}'|^3} \mathrm{d}^3\mathbf{r}' - \frac{1}{4\pi} \iint \sigma(r') \frac{\mathbf{r} - \mathbf{r}'}{|\mathbf{r} - \mathbf{r}'|^3} \mathrm{d}^2r'. \tag{1.10}$$

In the special case of a homogeneous magnetization throughout the sample volume, the first part of equation (1.10) vanishes and only the surface integral over $\sigma$ contributes to

the stray field.

### 1.2.2 Description of the tip sample system

In the case of negligible mutual influence of the sample's and tip's magnetization, the force gradient experienced by the magnetic tip can be derived from the magnetostatic interaction energy (Zeeman energy) [Aha96, Hub98]

$$E = -\mu_0 \iiint \mathbf{M}_{tip} \cdot \mathbf{H}_{sample} \, \mathrm{d}V_{tip} = -\mu_0 \iiint \mathbf{M}_{sample} \cdot \mathbf{H}_{tip} \, \mathrm{d}V_{sample}. \tag{1.11}$$

Due to the reciprocity principle [Wri95] the integration can be performed either over the sample or the tip magnetization. Introducing a coordinate system (see Figure 1.3) in which $\mathbf{r}$ denotes the position of the tip's apex, while $\mathbf{r'}$ is a vector pointing to a position within the sample gives

$$E(x,y,z) = -\mu_0 \iiint \mathbf{M}_{sample}(x',y',z') \cdot \mathbf{H}_{tip}\big(x'-x, y'-y, z'-z\big) \, \mathrm{d}x'\mathrm{d}y'\mathrm{d}z'. \tag{1.12}$$

This formula constitutes the basis for understanding MFM contrast formation. The energy in each point $(x,y,z)$ above the sample surface is a 3-dimensional convolution of the magnetization of the sample with the stray field of the tip[1]. The convolution is a sliding weighted average of the function $M(x,y,z)$ with the weighting function H. The above formulation represents the conventional view of the sample-tip interaction energy based on the Zeeman energy. This interaction integral can be equivalently formulated in terms of magnetic volume and surface charges and the scalar potential $\Phi_{tip}$ of the stray field [Hub97,Hub98,Zue99]. Substituting $\mathbf{H}_{tip} = -\nabla\Phi_{tip}$ in equation (1.12) and integration by parts gives

$$\begin{aligned} E(x,y,z) = &-\mu_0 \oint \sigma_{sample}(x',y',z') \cdot \Phi_{tip}(x'-x, y'-y, z'-z) \, \mathrm{d}x'\mathrm{d}y' \\ &-\mu_0 \iiint \rho_{sample}(x',y',z') \cdot \Phi_{tip}(x'-x, y'-y, z'-z) \, \mathrm{d}x'\mathrm{d}y'\mathrm{d}z'. \end{aligned} \tag{1.13}$$

[1] The integral in equation (1.12) is mathematically a correlation operation. In MFM literature the contrast formation is mostly described as the result of a convolution. As correlation and convolution are similar in nature for the sake of simplicity in the following the term *convolution* will be used, when referring to MFM image formation. The difference will only become important in Section 3.1.3.

The integration is performed over the sample surface $A'_{sample}$ and the sample volume $V'_{sample}$. This description is known under the name of "charge microscopy" (compare Subsection 1.1.2).

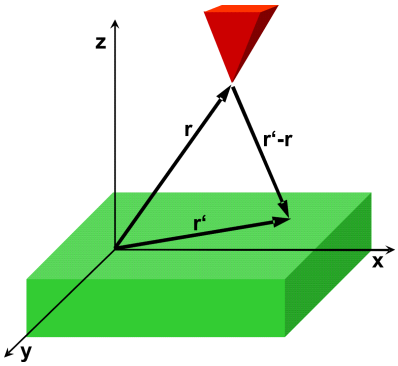


**Figure 1.3:** Definition of the coordinate system applied in the description of the magnetostatic energy of the tip-sample system.

In the dynamic measurement mode, which has been applied throughout the present work, the force gradient acting on the tip is detected (details about the measurement mode are given in Section 2.1.2).With the force being the negative gradient of the interaction energy $\mathbf{F} = -\nabla E$, equation (1.13) is transformed into

$$\begin{aligned}\nabla\mathbf{F}(x,y,z) = \mu_0 \oint \sigma_{sample}(x',y',z') \cdot \nabla\mathbf{H}_{tip}\,(x'-x, y'-y, z'-z)\;\mathrm{d}x'\mathrm{d}y' + \\ \mu_0 \iiint \rho_{sample}(x',y',z') \cdot \nabla\mathbf{H}_{tip}(x'-x, y'-y, z'-z)\,\mathrm{d}x'\mathrm{d}y'\mathrm{d}z'.\end{aligned} \tag{1.14}$$

Again for the special case of homogeneous volume magnetization the second integral vanishes. In this description the effect of the tip on the image formation is described by the tip's stray field gradient. Mathematically, this is the so-called convolution operator. The specific characteristics of the convolution operator have a large impact on the resulting imaging and will appear very often in the following explanations. Therefore it is useful to introduce an abbreviation for the stray field gradient of the tip. Similar to the notation in Fourier space, which will follow in Subsection 3.1.3 the notation for the convolution operator in MFM image formation is defined as Real Space Tip Function (RSTF).

### 1.2.3 Magnetostatics in Fourier space

The Fourier transformation of basic magnetostatic principles enables the derivation of some specific properties of the potential and of the field. The practical usefulness of these properties in Fourier space for the description of magnetic recording in general has been summarized by *Bertram* [Ber94] and the application to MFM image analysis has been

elaborated by *Hug et al.* [Hug98, vS99, vS00, Kap03, Mey04, Kap05a, Pil06, Pil07, Sch08, Sch10b]. These properties are essential to the method of MFM image analysis as applied in large parts of this thesis. Thus, the derivations will be given in detail in this section.

If a function $f(\mathbf{r})$ of the 2-dimensional variable $\mathbf{r} = (x, y)$ is considered, then the Fourier transform of $f$ is defined by the following integral, whenever it is convergent [Ber98]

$$\hat{f}(\mathbf{k}) = \int e^{-i\mathbf{kr}} f(\mathbf{r}) d\mathbf{r}. \tag{1.15}$$

Here is $d\mathbf{r} = dx, dy$ and $\mathbf{k} \cdot \mathbf{r} = k_x x + k_y y$. The integral extends for all variables from $-\infty$ to $+\infty$. The following inversion formula holds true, if also in this case the integral is convergent

$$f(\mathbf{r}) = \frac{1}{(2\pi)^2} \int e^{i\mathbf{rk}} f(\mathbf{k}) d\mathbf{k}. \tag{1.16}$$

The components of the vector $\mathbf{r}$ have the physical meaning of space variables and the corresponding components of the vector $\mathbf{k} = (k_x, k_y)$ are called space frequencies.

A simple description of the decay behavior of the magnetostatic potential can be found in Fourier space by the following considerations[2]. A magnetic volume extending into infinity in the x and y direction (a magnetic thin film), as sketched in Figure 1.4, is defined. The magnetization is assumed to be homogeneous throughout the thickness and therefore no volume charges need to be taken into account. The magnetostatic potential outside the

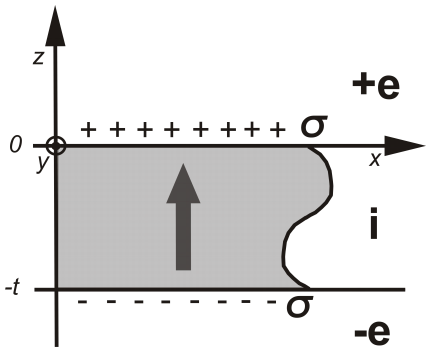


**Figure 1.4:** Sketch of the coordinate system and notations used for the derivation of the magnetostatic potential of a magnetic volume. The symbol $\sigma$ represents the surface charges, i stands for space inside the volume and +e and -e outside, t denotes the thickness. The volume is extended to infinity in the x and y directions.

magnetic volume in the region +e and -e ($z > 0$ and $z < -t$, respectively, see Figure 1.4) has to be derived. The exact form of $\Phi(\mathbf{k}, z)$ can be found from solving the Laplace

[2]The derivation has been performed with the help of N. Kiselev, present address: Forschungszentrum Jülich, Peter Grünberg Institut

equation ($\Delta\Phi = 0$), which in Fourier space reads:

$$\Delta_k \hat{\Phi}_{\pm e}(\mathbf{k}, z) = 0 \tag{1.17}$$

The boundary condition at the upper volume surface ($z = 0$) is given by:

$$\frac{\partial}{\partial z}\hat{\Phi}_i(\mathbf{k}, z)\bigg|_{z=0} - \frac{\partial}{\partial z}\hat{\Phi}_{+e}(\mathbf{k}, z)\bigg|_{z=0} = \sigma(\mathbf{k}) \tag{1.18}$$

and at the lower surface ($z = -t$) by:

$$\frac{\partial}{\partial z}\hat{\Phi}_i(\mathbf{k}, z)\bigg|_{z=-t} - \frac{\partial}{\partial z}\hat{\Phi}_{-e}(\mathbf{k}, z)\bigg|_{z=-t} = \sigma(\mathbf{k}). \tag{1.19}$$

A second boundary condition at the surfaces is given by:

$$\hat{\Phi}_i(\mathbf{k}, 0) = \hat{\Phi}_{\pm e}(\mathbf{k}, 0). \tag{1.20}$$

The potential vanishes at infinity:

$$\lim_{z\to+\infty} \hat{\Phi}_{+e}(\mathbf{k}, z) = 0. \tag{1.21}$$

$$\lim_{z\to-\infty} \hat{\Phi}_{-e}(\mathbf{k}, z) = 0. \tag{1.22}$$

The nabla operator is defined in Fourier space as $\nabla_k = \left(ik_x, ik_y, \frac{\partial}{\partial z}\right)$ and the Laplace operator is therefore given by $\Delta_k = \nabla_k^2 = \nabla_k \cdot \nabla_k = \left(-k_x^2 - k_y^2 + \frac{\partial}{\partial z}\frac{\partial}{\partial z}\right)$. Together with $k = \sqrt{k_x^2 + k_y^2}$ equation (1.17) can be rewritten as:

$$-k^2 \hat{\Phi}_{\pm e}(\mathbf{k}, z) + \frac{\partial^2}{\partial z^2}\hat{\Phi}_{\pm e}(\mathbf{k}, z) = 0. \tag{1.23}$$

The general solution of equation (1.23) is

$$\hat{\Phi}_{+e}(\mathbf{k}, z) = A_1 e^{kz} + A_2 e^{-kz}, \tag{1.24}$$

$$\hat{\Phi}_{-e}(\mathbf{k}, z) = A_3 e^{kz} + A_4 e^{-kz}. \tag{1.25}$$

Here $A_i$ are parameters which do not depend on z, but generally can be functions of the variable $\mathbf{k}$. From condition (1.22) it immediately follows that $A_1 = A_4 = 0$. By substituting the solution into the boundary conditions the exact form of $A_2$ and $A_3$ can be found.

The resulting equation for the potential above the upper surface finally reads:

$$\hat{\Phi}_{+e}(\mathbf{k}, z) = \frac{e^{-kz} \cdot \left(1 - e^{-kt}\right)}{2} \cdot \frac{\sigma(\mathbf{k})}{k}. \tag{1.26}$$

Herewith the 2-dimensional surface integral in the second part of equation (1.7) simplifies to a multiplication and accelerates the calculation of potentials of thin film domain structures enormously. An important statement of the above equation is the exponential decay of the potential with distance away from the charges. In the case of a thin magnetic layer with top and bottom charges this practically means, that a 2-dimensional *effective* surface charge map can be composed by summing up the layers with the application of the function $e^{-kt}$ to the lower layer (t denotes the thickness of the film, see Figure 1.4).

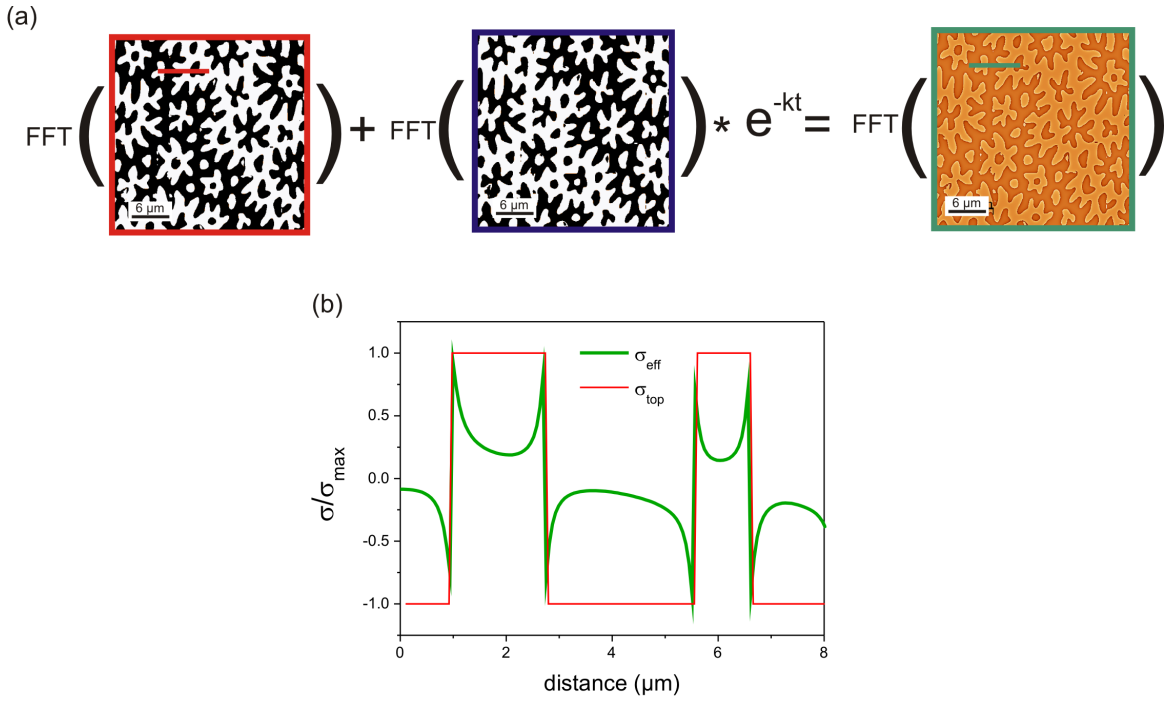


**Figure 1.5:** (a) Illustration of the calculation of a 2-dimensional effective surface charge map. The surface charges of the top and the bottom layer of the thin film are summed up. The bottom charge map is the inverse of the top charge map. The bottom layer is projected onto the surface by multiplying its Fourier transform with the decay factor $e^{-kt}$ (according to the derivation given in the text), where t denotes the thickness of the film. (b) Line section along the red and the green line drawn in the images of the charge maps of (a).

The effective surface charge map has the same potential and will therefore create the same stray field as the two separated layers. This mathematical transformation can later on help, when calculating the convolution product of the sample charges and the tip stray field gradient as given in equation (1.14). A visualization of this operation is shown in Figure 1.5. Furthermore, in regions outside the magnetic volume, where the Laplace equation

$(-k_x^2 - k_y^2 + \frac{\partial^2}{\partial z^2})\hat{\Phi}(\mathbf{k}, z) = 0$ holds, the Nabla operator becomes $\nabla_k = (ik_x, ik_y, k)$ and the stray field can be calculated from the potential by

$$\hat{\mathbf{H}}(\mathbf{k}, z) = - \begin{pmatrix} ik_x \\ ik_y \\ k \end{pmatrix} \hat{\Phi}(\mathbf{k}, z). \tag{1.27}$$

With this the scalar potential is fully determined by each of the components of the field [Mey04]. The converse argument is that from one field component the other two components can be calculated:

$$\hat{\mathbf{H}}(\mathbf{k}, z) = \frac{\nabla_k}{k} \hat{H}_z(\mathbf{k}, z). \tag{1.28}$$

This does not hold for the average value $H(k_x = 0, k_y = 0)$ [vS99]. This means, that the relative contrast of the images can be correctly obtained, but the absolute value of the signal can not be calculated this way. From the connection of the stray field and potential according to equation (1.27) it follows that the stray field also decays exponentially in Fourier space. This has consequences for the calculation of theoretical MFM signals as will be explained in Section 3.6.

All the above explanations refer to general properties of magnetostatic quantities in Fourier space. Their application to specific problems arising in MFM imaging will be discussed in Chapter 3. The main motivation for all these transformations is the fact, that discrete calculations can be very much simplified and accelerated this way. Furthermore, the reformulation of some physical relations, like in the case of formula (1.28), facilitates the handling of magnetic stray fields and comprehension of their properties.

# 2 Instrumentation

This chapter introduces the instrumentation applied for the investigations in this thesis. As MFM belongs to the family of Scanning Force Techniques (SFM) the first section contains the basic measurement principle and operation modes. While the first chapter dealt with the origin and description of the tip-sample interaction, this chapter focuses on the technical realization of acquisition of the relevant physical quantities.

Two different kinds of microscopes were used for the measurements discussed in this thesis. They differ in their measurement modes as well as in the condition under which they are operated: vacuum and ambient atmosphere.

Global magnetization measurements play an important role beside the local investigations to gain a full picture of the present magnetization status. For this Vibrating Sample Magnetometry (VSM) has been applied and will therefore be introduced in the last section of this chapter.

## 2.1 Scanning Force Microscopy (SFM)

### 2.1.1 Measurement principle and operation modes

A simplified picture of the basic measurement principle and the major components of a Scanning Force Microscope are given in Figure 2.1. The objective of the measurement technique is to detect the force on the cantilever due to the interaction between tip and sample. This is done by an optical beam deflection system. The probe is attached to a cantilever with reflective backside coating from which the laser beam is reflected onto a quadrupole photocell. The cantilever itself is attached to a piezoelectric transducer, so that the signals coming from the photodiode can be recorded and used as input to a feedback loop.

In the *static mode* of operation, the detected quantity is the bending of the cantilever. In the so-called *dynamic mode* the cantilever is oscillating near its resonance frequency. This offers the access to additional parameters, which are sensitive to tip-sample interactions such as amplitude, frequency and phase of the oscillation.

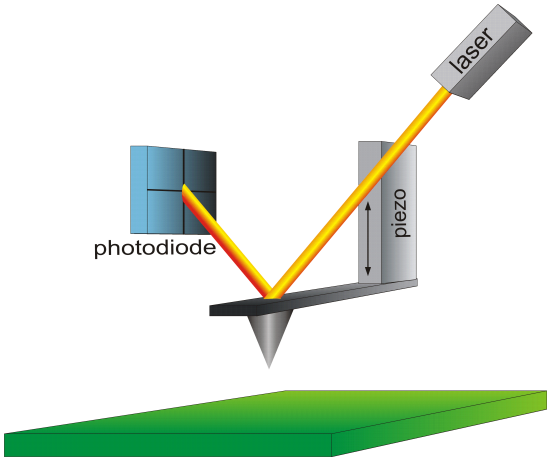


**Figure 2.1:** Schematic illustration of the basic SFM measurement principle based on an optical beam deflection system.

The dynamic mode itself can be further divided in different operation modes regarding the distance in which the probe is scanned over the sample. Again the Lennard-Jones potential can be used to illustrate the definitions of these modes (figure 2.2). In the repulsive region the tip is in *contact* and after the inflexion point is reached, *non-contact* is defined. If the probe jumps between contact and non-contact, the mode is called *intermittent contact* or *tapping mode* as the probe "taps" the sample surface. Operation in non-contact or intermittent contact mode is not exclusive of a given dynamic SFM method [Gar02].

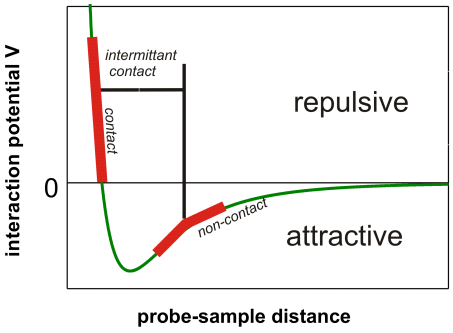


**Figure 2.2:** Diagram of the Lennard-Jones-potential and the classification of modes in dynamic SFM [Dan06].

### 2.1.2 Dynamic mode SFM

In order to be able to quantify the strength of the tip-sample interaction it is necessary to find an analytical expression, which links the dynamic properties of the oscillating

cantilever with the forces acting on the tip. This requires a closer look on the equation of motion of the vibrating cantilever. It has been shown, that the cantilever can be considered as a point spring-mass ( [Gar02] and references [18]-[32] therein). In this case the tip motion can be described by a non-linear, second-order differential equation [Tip00]

$$m\frac{d^2z(t)}{dt^2} + \frac{m\omega_0}{Q}\frac{dz(t)}{dt} + cz(t) = F_0\cos(\omega t) \tag{2.1}$$

where c, m and $\omega_0$ are the spring constant, the mass and the resonance angular frequency of the cantilever, respectively. $z(t)$ is the deflection of the cantilever from its idle state. The amplitude of the driving force is $F_0$ and $\omega = 2\pi f$ its angular frequency. The term $\frac{m\omega_0}{Q}\frac{dz(t)}{dt}$ describes the damping of the oscillation with Q being the quality factor.

The solution of equation (2.1) is composed of two parts, the transient term and the steady state term [Tip00]. The stationary solution, not depending on the initial conditions anymore, reads for a freely oscillating cantilever

$$z(t) = A_{free}\cos(\omega t - \phi_{free}). \tag{2.2}$$

The dependence of the amplitude $A_{free}$ on the excitation frequency can be calculated by [Gar02]

$$A_{free} = \frac{F_0/m}{\sqrt{(\omega^2 - \omega_0^2)^2 + (\omega_0\omega/Q)^2}} \tag{2.3}$$

and the phase shift $\phi_{free}$ by

$$\phi_{free} = \arctan\frac{\omega_0\omega/Q}{\omega^2 - \omega_0^2}. \tag{2.4}$$

The relationship between the phase shift and the driving frequency establishes that, at resonance, the phase lag is exactly 90°. Driving frequencies far below the free resonance produce zero phase shifts, whereas frequencies above resonance produce a phase shift of 180° [Gar02]. Approaching the tip to the surface leads to additional forces $F_{ext}$ caused by the interaction, which influence the vibrational dynamics. Assuming small displacements with respect to the idle position $Z_0$ allows a Taylor expansion and the resulting force reads

$$F_{ext} \approx \left.\frac{dF_{ext}(z)}{dz}\right|_{z=Z_0} z(t). \tag{2.5}$$

The equation of motion has to be extended by this additional external force and finally reads

$$m\frac{d^2z(t)}{dt^2} + \frac{m\omega_0}{Q}\frac{dz(t)}{dt} + \left(c - \frac{dF_{ext}(Z_0)}{dz})z(t)\right) = F_0\cos(\omega t). \tag{2.6}$$

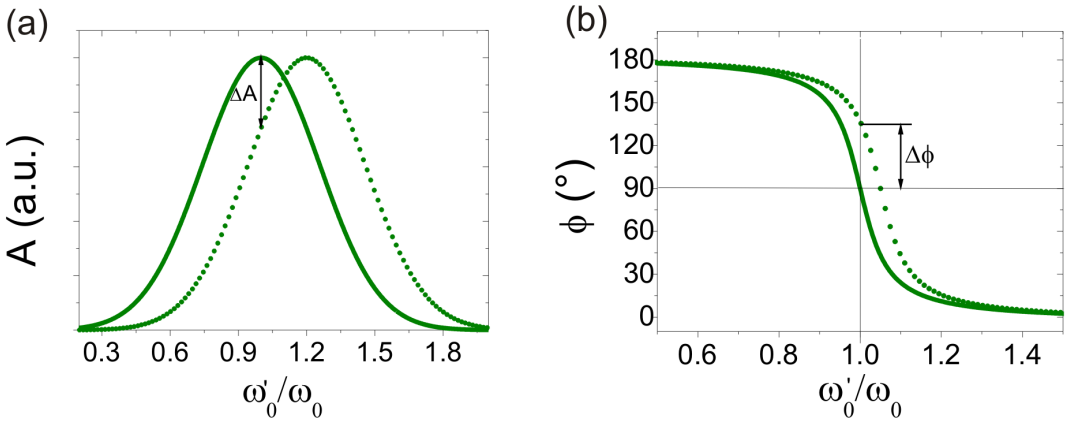


**Figure 2.3:** Basic principle of the force gradient detection in dynamic SFM mode. The cantilever oscillates with a fixed frequency $\omega_0$. The influence of an external force gradient (dotted line) results in a shift of (a) amplitude and (b) phase.

With this an effective spring constant can be defined as

$$c_{eff} = c - \left.\frac{dF_{ext}(z)}{dz}\right|_{z=Z_0}. \tag{2.7}$$

From this it follows, that an attractive tip-sample interaction with $\frac{dF_{ext}}{dz} > 0$ leads to an effectively softer and a repulsive interaction $\frac{dF_{ext}}{dz} < 0$ to a stiffer behavior of the cantilever. Further, this modification of the spring constant causes a shift in the resonance frequency from $\omega_0 = \sqrt{\frac{c}{m}}$ to $\omega_0^{'}$:

$$\omega_0^{'} = \sqrt{\frac{c_{eff}}{m}} = \sqrt{\frac{c - \frac{dF_{ext}}{dz}}{m}} = \omega_0\sqrt{1 - \frac{1}{c}\frac{dF_{ext}}{dz}}. \tag{2.8}$$

With $\frac{dF_{ext}}{dz} << c$ the right side of the equation can be written as $\omega_0(1 - \frac{1}{2c}\frac{dF_{ext}}{dz})$ (Taylor expansion) and the shift of resonance frequency is finally given by:

$$\Delta\omega \approx -\frac{\omega_0}{2c}\frac{dF_{ext}}{dz}. \tag{2.9}$$

With this the link between the force gradient $\frac{dF_{ext}}{dz}$ and the experimentally accessible quantity $\omega$ has been derived. From equations (2.3) and (2.4) follows, that a shift in $\omega_0$ also results in a modified amplitude and phase of the oscillation. The impact of a force gradient on the resonance curve is schematically illustrated in Figure 2.3. Beside the shift no size or shape modifications can be observed [Gar02].

## 2.2 Lift mode MFM

The microscope used for most of the experiments presented in this thesis is a Veeco Dimension 3100. It is an automated, combined AFM and MFM operated at ambient conditions. The Nanoscope version III controller provides the possibility to operate the microscope

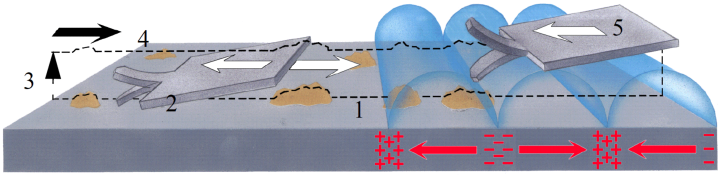


**Figure 2.4:** 1 and 2 : Cantilever traces surface topography on first trace and retrace. 3: Cantilever ascends to lift scan height. 4 and 5: Lifted cantilever profiles topography while responding to magnetic influences on second trace and retrace [HAN98].

in a so-called *Interleave* scanning modus. The interleave modus changes the scan pattern of the tip in a way, that each line is scanned twice. In the first scan, the measurement is performed in the *tapping mode* with the amplitude as input for the feedback. During the interleave scan, the feedback is turned off and the tip is lifted (*LiftMode*) to a user selected height above the surface to perform a far field measurement of the magnetic signal. The topographic or AFM data recorded during the first pass is used to keep the distance between surface and tip constant. This mode enables the isolation of purely MFM data from AFM data during one single measurement.

The signal measured in this microscope was always the shift in phase $\Delta\phi$ with a fixed drive frequency. The phase is connected to the frequency in equation (2.4) for a free cantilever oscillation. Replacing $\omega_0$ with $\omega_0' = \omega_0 + \Delta\omega$ according to the harmonic approximation, the value of the phase shift for a cantilever exposed to external interaction $\phi_i(\omega)$ at $\omega = \omega_0$ is given by [Mag97, Wha98]:

$$\phi_i(\omega_0) = \arctan\left[\left(\frac{1}{2Q}\right)\left(\frac{\omega_0}{\Delta\omega + 1}\right)\right] \approx \arctan\left(\frac{\omega_0}{2Q\delta\omega}\right). \tag{2.10}$$

As mentioned in the previous section the phase lag $\phi_{free}$ at resonance is $\pi/2$ for the free cantilever oscillation. From the above equation it follows, that the phase shift $\Delta\phi$ $= \phi_{free}(\omega_0) - \phi_i(\omega_0)$ at the driving frequency $\omega_0$ can be expressed as [Mag97, Wha98]:

$$\Delta\phi = \pi/2 - \arctan\left(\frac{\omega_0}{2Q\Delta\omega}\right) \approx 2Q\frac{\Delta\omega}{\omega_0}. \tag{2.11}$$

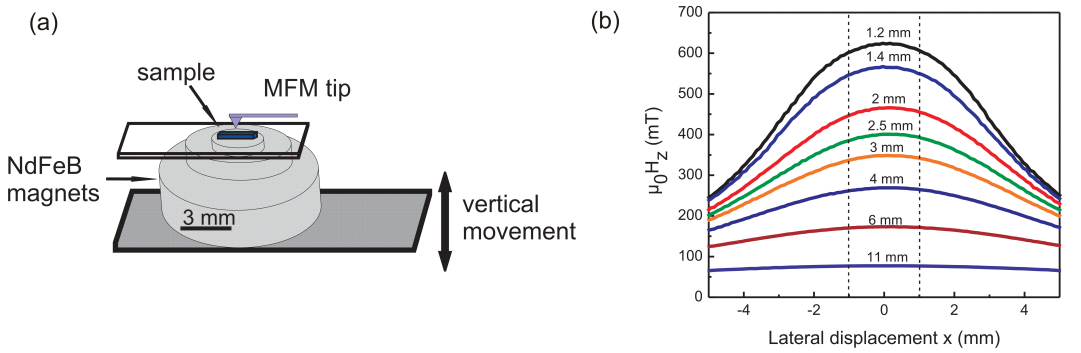


**Figure 2.5:** (a) Schematic drawing of the magnetic field stage used for magnetic field application during measurement, (b) Lateral $H_z$ characteristic at different distances measured by a Hall sensor [Bra10].

Finally, with equation (2.9) the force gradient is linked to the phase shift by

$$\Delta\phi \approx -\frac{Q}{c}\frac{dF_z}{dz} \tag{2.12}$$

The MFM data acquired by phase shift detection will always be given in degrees.

Field dependent measurements were also performed using this instrument. In order to apply a perpendicular magnetic field to the sample during the MFM measurement, a magnetic field stage was used, which has been constructed and applied on various in-field measurements previously by C. Bran [Bra10]. The setup consists of a pyramidal stack of NdFeB permanent magnets with their magnetic easy axis perpendicular to the sample surface, which can be lifted up gradually to approach the sample from below. The lateral field homogeneity is better than 1 % within a radius of 1 mm from the center of the magnet and the field strength in the central area can be varied from 0.02 T to a maximum of 0.6 T for a fully approached magnet as shown in Figure 2.5 [Bra10].

## 2.3 Non-contact MFM

Non-contact MFM was performed with a *Nanoscan High-Resolution MFM* (hr-MFM). The measurements were conducted at room temperature in a vacuum of $10^{-7}$ mbar. A large advantage of the setup is the freedom provided by the software *Scandirector*. It allows for example the modification of the general scan concept by the user so that beside $x-y$-scans also $x-z$ and $y-z$ scans are allowed. With this e.g. the tip-sample distance can be estimated by acquiring $\Delta f$-distance curves in various positions allowing a very precise plane correction (necessary if the sample is slightly tilted with respect to the scanning plane).

The operation in vacuum provides a sharper resonance curve and with this a higher Q-value. The signal-to-noise ratio is increased compared to measurements at ambient conditions.

Magnetic imaging is performed in a true non-contact mode at a constant height. This means that the tip never touches the surface and thus can not be damaged at its apex. However, the drawback of this method is the difficulty to separate topographic features from magnetic contrast. For rough samples the image has to be recorded twice with the tip magnetization inversed, which is very time consuming. The measurements performed with the hr-MFM were applied to a sample with a very flat surface with a roughness below 5 nm, so that the topographic influence could be neglected.

The magnetic contrast is detected via frequency modulation by a phase-locked loop controller, which shifts the excitation frequency such, that it follows the resonance of the cantilever. Effectively, the controller keeps the phase shift of 90° constant as it is the case in resonant oscillation. The frequency shift ($f = \omega/2\pi$) is given by

$$\Delta f \approx -\frac{f_0}{2c}\frac{dF_z}{dz} : \tag{2.13}$$

The measured quantity is given in units of Hz.

## 2.4 Vibrating Sample Magnetometry

Complementary to the local measurements global magnetization measurements are needed to obtain a full understanding of the magnetization state of the material under investigation. For this purpose Vibrating Sample Magnetometry (VSM) has been applied. The instrument used in this thesis is a *Quantum Design Physical Property Measurement System* (PPMS) with a VSM option as shown in Figure 2.6.

A vibrating sample magnetometer (VSM) measures an AC field produced by the moment of a vibrating sample, which is detected by pick-up coils. To analyze the obtained field the principle of reciprocity can be applied [Zie82]. It states that the magnetic flux $\Phi$ produced by a magnetic moment m in a coil of arbitrary geometry is equivalent to the field B (at the position of the moment) produced by the same coil carrying a current I. This principle allows the calculation of the flux of a dipole field using the Biot-Savart law. For arbitrary direction of m and B in free space the following equation holds [Zie82]

$$\mathbf{B} \cdot m = I\Phi. \tag{2.14}$$

For a moment moving with velocity v(t), the induced voltage is given by [Zie82]

$$U(t) = \frac{d\Phi}{dt} = \text{grad}\left(\frac{\mathbf{B}(\mathbf{r})}{I} \cdot m\right) = mG(\mathbf{r})v(t) \tag{2.15}$$

where $G(\mathbf{r}) = (d/dz)(B_m(\mathbf{r})/I)$ is called the sensitivity function. It represents the derivative along the direction of sample motion z of the field component $B_m$ parallel to the direction of moment produced by a fictitious unit current in the detection coils. The applicability of this equation is restricted to the case of a sample being sufficiently small compared to the coil diameter so that the approximation of a dipole field holds. In order to measure hysteresis loops an external field can be applied by additional superconducting coils, which produce a field parallel to the axis of sample motion.

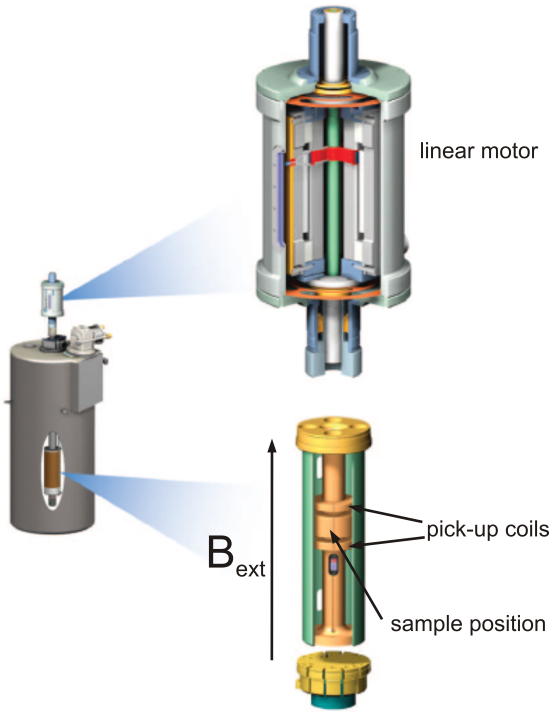


**Figure 2.6:** Schematic of a PPMS with VSM option (Quantum Design [VSM13]).

# 3 Quantitative Magnetic Force Microscopy

After introducing all relations and quantities necessary to understand the origin of the acquired data in an MFM experiment in Chapter 1 and 2, this chapter concentrates on the problem of applying these equations to analyze the data in a quantitative manner. For this reason the first section introduces the general problem of MFM image inversion, gives an overview on the solutions available in literature and explains in detail the approaches chosen in this thesis. The following sections focus on the practical realization of quantitative MFM applying existing methods and also a tip calibration procedure developed within this work based on the transfer function approach. Further, the used calibration samples and MFM probes are introduced and several additional procedures necessary for image analysis, such as noise measurements and tests of mutual tip sample influences are explained.

## 3.1 The challenge of MFM image inversion

### 3.1.1 Description of the problem and state of the art

Despite the well-known physical relations necessary to describe the contrast formation in MFM the inversion of the formulas and with this the connection of the measured quantities to magnetic information about the sample remains challenging. Since the magnetic fields have long-range nature the local MFM signal is always the sum of contributions originating from the interaction of the whole magnetically active tip volume and the stray field environment in which it is immersed. This manifests itself in the 3-dimensional convolution given in equation (1.14), which is rather difficult to inverse. Reasons for this are:

- The magnetic structure of the tip is a priori unknown.
- The inverse solution of a convolution integral of the given form (equation (1.14)) is not unique.
- Real experimental data is discrete and always contains noise leading to unphysical inverse solutions.

The first item refers to the fact, that the tip's magnetization is almost as unknown as the magnetization of the sample under investigation. It is clear, that the thorough knowledge of the imaging properties of the MFM tip is a very basic requirement for quantitative MFM.

The second difficulty arises from the contrast formation itself. The MFM procedure follows the classical form of imaging. A given object is transformed by an operator into an image. The operator can stand for a camera, a microscope or another measurement equipment. That the inverse solution even of an apparently simple linear imaging process is not unique is due to the loss of information, which is typical for the given direct problem [Ber98]. One reason for this is, that in space-invariant imaging systems, such as MFM, the imaging process has the effect of a low-pass filter which tends to zero at high frequencies and does not transfer information above a certain frequency due to lack of resolution. Additionally, if the operator contains zeros in a certain frequency range, objects, which differ only in this range will look alike. The extreme case of this scenario even leads to the phenomenon of invisible objects, which is illustrated in Figure 3.1. Secondly, and especially in MFM imaging it is not unlikely, that two very distinct objects have images, which are very close. *Vellekoop* et al. showed that an in-plane magnetized film can generally not be distinguished from an out-of-plane magnetized film without additional information. Here it is exactly the case, that these principally very different magnetization states produce, in a sufficiently large distance above the film, the same image [Vel98].

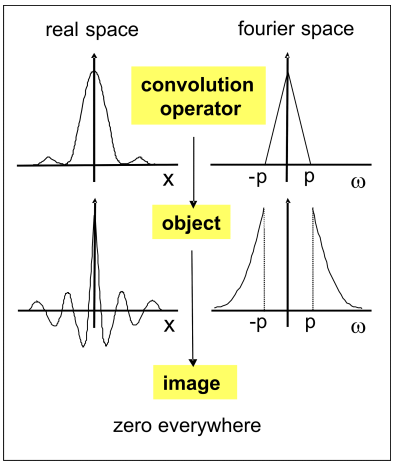


**Figure 3.1:** If a convolution operator containing zeros outside the interval (-p,+p) and is convolved (in real space)/multiplied (in Fourier space) with an object being nonzero exactly in this interval produces an image which is zero everywhere (after [Ber98]).

The last reason listed above can be understood by considering that under any real experimental conditions data are affected by noise. The inverse solution of the imaging process largely amplifies this noise and leads to physically unreasonable results as will be explained in more detail in Section 3.1.3.

The approaches available to overcome the above listed obstacles are reviewed in the following. By far the most attempts towards quantitative MFM are made by simplifying the magnetization of the tip in various ways such that it can be easily calibrated. One of the first groups were *Saenz et al.*, who described the probe in terms of its overall magnetic moment. The magnetic volume of the tip is assumed to be homogeneously magnetized and described by its dipole moment [Sae87]. The geometry is included by assuming a spherical or needle-like tip shape. Further simplification of the tip leads to the point dipole approximation. Already in 1988 *Mamin et al.* modeled the tip as a point dipole and could use the so gained information to qualitatively understand the measured MFM data [Mam88]. Later on *Hartmann*, *Lohau et al.* and *Kebe et al.* showed that the dipole should be located in the middle of the effective magnetic tip volume to achieve good agreement between measurement and models [Har89, Loh99, Keb04]. To utilize this model for subsequent quantitative MFM it is necessary to know the exact dipole moment and the position of this dipole within the tip volume. This can be achieved by calibration with well-known stray fields as presented in numerous publications [Kon97,Loh00,Loh01,Was02] and in the framework of this thesis (see Chapter 4). Another point probe approach models the tip as a monopole moment. This model applies best, if the tip is of elongated, needle like shape and only the magnetic charges at the bottom side of the probe close to the sample contribute to the MFM signal. Again, the tip is either calibrated with reference samples with known stray fields [Loh99, Keb04, Wei08, Jaa08, Voc10, Wol10] or, as used for quantitative MFM on superconductors, the monopole moment is taken as a fitting parameter [Str08, Lua09, Sha10b, Sha11].

A better description of the stray fields originating from real MFM probes can be achieved by extending the point probe approximation into a 2-dimensional charge pattern [McV01a, McV01b]. The authors show, that the extended charge distribution fits the stray fields determined by Lorentz microscopy of commercial MFM tips significantly better than a pure dipole or monopole model.

A large amount of very different approaches aiming to include the finite-size of the probe can be found in various publications. Even though, they are more time consuming, the resulting MFM signals are in general closer to reality than for a point probe. *Rugar* et al. modeled their self-made electrochemically etched nickel nanowire tips by approximating the geometry by a truncated cone with a spherical cap at the tip apex. Geometrical parameters were varied to fit the measured MFM signal [Rug90]. *Luan et al.* and *Kiselev et al.* assumed a truncated triangle [Kis08, Lua10] and *Nazaretski et al.* take the shape of the tip from a nonlinear curve fit to its SEM image [Naz09]. *Ovchinnikov et al.* extend the calculation to a realistic 3-dimensional geometry considering the probe as a nonmagnetic truncated cone covered by a magnetic layer [Ovc01] and *Hosaka et al.* treat the tip as a simple cone [SH94]. A detailed comparison between an analytical and numerical calculation

of the MFM response based on a tip model assuming a distribution of dipoles in the magnetic tip coating (extended dipole model) is given by *Engel-Herbert et al.* [EH06]. They find, that the computational effort using the numerical method is by far smaller than for the analytical one. Even more time-consuming, but coming closer to realistic magnetization distributions within the magnetic tip coating are micromagnetic simulations of the tip as done by *Oti* and *Tomlinson et al.* [Oti93, Tom97]. *Garcia et al.* also use a micromagnetic simulation of a conical magnetic shell as a tip model and they find, that the so calculated stray field is extremely similar to that of a monopole [Gar01]. Based on this, they simplify their MFM tip in their following work as monopole, where the two parameters strength and position are predefined by the simulation results [GM04].

A very recent publication by *Häberle et al.* introduces a so-called pseudo-pole model based on a 3-dimensional integration over an assumed cone geometry of the sensor [Häb12]. The authors claim, that the simple $1/z$ axial dependence of the tip stray field, which they find analytically, holds for small enough tip-sample separations and is accurate for the applied commercially available thin film MFM tip.

Even though the idea of MFM image restoration in Fourier space has been published earlier or parallel [Sch90, Mad96, Zhu98], the only method which goes without any fitting parameters and simplification is the so called transfer function approach first introduced in detail in 1998 for quantitative MFM by *Hug et al.* [Hug98]. This powerful method is based on a tip calibration and describes the MFM probe by means of its actually present magnetization distribution including all three dimensions of the tip. It has been successfully applied to different kind of magnetic problems and published in numerous articles by the workgroup [vS00, Kap03, Kap05b, Mar06, Pil07, Sch10b]. The procedure will be described in Section 3.1.3 and the difficulties coming along, together with a proposal for their solution, will be given in the following sections 3.1.3 and 3.2.

### 3.1.2 The point probe approximations

Provided that some experimental preconditions are satisfied, the MFM tip can be described by a point magnetic charge [Har89]. The decay length of a given sample stray field and the geometry of the probe determine the effective interaction volume. If the magnetization within this volume is homogeneous, the integral formulation[1] can be replaced by the overall magnetic moment making the integration unnecessary. This is only possible, if the effective interaction volume is close to the tip apex, where the magnetization is assumed to be uniform and predominantly along the probe axis. The magnetic response outside this

[1] The following explanations make use of the reciprocity principle mentioned in Subsection 1.2.2. This simply means, that the indexes in equation (1.14) are interchangeable. Thus, the integration is performed on the tip surface and over the volume.

fictitious domain is completely neglected. Within this approximation the force acting on the probe is given by [Har89, Har94]

$$\mathbf{F}(\mathbf{r}) = -\mu_0(q + \mathbf{m}\nabla)\mathbf{H_s}(\mathbf{r}) \tag{3.1}$$

where $\mathbf{H_s}$ denotes the stray field of the sample, $q$ the magnetic monopole moment and $\mathbf{m}$ the magnetic dipole moment of the probe. In dynamic operation mode the force gradient is detected [Keb04]:

$$\frac{dF_z}{dz}(\mathbf{r}) = -\mu_0 \left[ q\frac{\partial H_z}{\partial z}(\mathbf{r}) + \left( m_x \frac{\partial^2 H_x}{\partial z^2}(\mathbf{r}) + m_y \frac{\partial^2 H_y}{\partial z^2}(\mathbf{r}) + m_z \frac{\partial^2 H_z}{\partial z^2}(\mathbf{r}) \right) \right] \tag{3.2}$$

The pure dipole tip approximation ($q = 0$ in the above equation) was first applied to model the MFM response to longitudinal recording media by Mamin et al. [Mam88]. To get agreement between model and experiment the dipole had to be located much further away from the sample surface than the actual location of the tip apex. This can be understood by the fact, that the effective dipole moment has to be positioned into the center of the effective tip volume, which is influenced by the decay length of the sample stray field [Har89] (compare sketch in Figure 3.2 (a)). This practically means, that the parameters need to be determined for various domain sizes. In the case of the monopole model, the

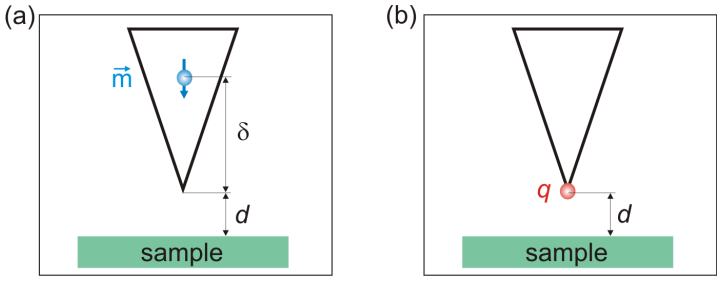


**Figure 3.2:** Sketch of the dipole (a) and monopole (b) model. The dipole is situated in the center of the interacting tip volume with the distance $\delta$ above the tip apex. The lift height is denoted by d.

effective monopole should sit right at the end of the tip (see Figure 3.2 (b)). However, experimental tip calibrations have shown, that also the monopole moment requires a small displacement away from the tip apex to fit the data properly [Loh99, Keb04, Wol10, Voc10]. The concept of the point probe approximation has been shown to achieve very satisfying results for special cases. Nevertheless, this is only a rough estimation, where the mentioned preconditions have to be fulfilled.

### 3.1.3 The transfer function approach

#### Theoretical description

Working in Fourier space simplifies the 3-dimensional convolution integral in formula 1.14 largely. The convolution theorem states that [Kli01, Pre92]:

$$\mathcal{F}\left\{\int_{-\infty}^{\infty} f(x')g(x-x')\mathrm{d}x'\right\} = \hat{f}(k_x)\cdot\hat{g}(k_x) \tag{3.3}$$

where $\mathcal{F}$ symbolizes the Fourier transformation. Considering a magnetic sample without volume charges, only the first term in equation 1.14 needs to be calculated. As the measured physical quantity in MFM is the force gradient, the gradient of equation 1.14 is Fourier transformed with respect to the x- and y-coordinates. This leaves only the sum over the surface charge distribution on the top and bottom side of the magnetic volume, while the integration over $x'$ and $y'$ (the sample surface $A'_{sample}$) simplifies to a multiplication as given by:

$$\nabla\hat{\mathbf{F}}(\mathbf{k},z) = -\mu_0 \sum \nabla\hat{\mathbf{H}}_{tip}(\mathbf{k},z-z')\hat{\sigma}_{sample}(\mathbf{k},z') \tag{3.4}$$

where $\mathbf{k} = (k_x, k_y)$. Including the exponential decay behavior of stray fields in Fourier space (compare Section 1.2.3) and referring to the coordinate system defined in figure 1.3 the stray field gradient is given by $\nabla\hat{\mathbf{H}}_{tip}(z-z') = \nabla\hat{\mathbf{H}}_{tip}(z)e^{+kz'}$ and the above equation can be rewritten[2]:

$$\begin{aligned}\nabla\hat{\mathbf{F}}(\mathbf{k},z) &= -\mu_0\nabla\hat{\mathbf{H}}_{tip}(\mathbf{k},z)\sum e^{kz'}\hat{\sigma}_{sample}(\mathbf{k},z') \\ &= -\mu_0\nabla\hat{\mathbf{H}}_{tip}(\mathbf{k},z)\hat{\sigma}^*_{sample}(\mathbf{k}).\end{aligned} \tag{3.5}$$

The summation over the top and bottom surface is replaced by the effective sample surface charge $\hat{\sigma}^*_{sample}$. The Fourier transform of the stray field gradient of the tip $\nabla\hat{\mathbf{H}}_{tip}$ is the so-called tip transfer function (TTF = $\hat{f}(k_x, k_y)$), which is equivalent to the convolution operator (real space tip function: RSTF = f(x,y)) in real space. The TTF *transfers* the influence of the sample on the tip into a force gradient.

The next step is to describe, how the force gradient is transfered into the imaged contrast given by a frequency shift $\Delta f$ or phase shift $\Delta\phi$. For this purpose *Hug et al.* introduce a so-called *Instrument Calibration Function* ICF [vS00]. The definition of such a function simplifies the calibration procedure by summarizing all properties, such as the spring constant and the canting of the cantilever and the properties of the oscillation (Q, $f_0$). The

[2]The positive sign in the exponent results from the definition of the coordinate system.

ICF defines the imaging properties of the system for a given feature wavelength [Mey04]:

$$\Delta\hat{\phi}(\mathbf{k}, z) = \mathrm{ICF}_{\Delta\phi}(\mathbf{k}, z) \cdot \hat{\sigma}^*_{sample}(\mathbf{k}), \tag{3.6}$$

$$\Delta\hat{f}(\mathbf{k}, z) = \mathrm{ICF}_{\Delta f}(\mathbf{k}, z) \cdot \hat{\sigma}^*_{sample}(\mathbf{k}). \tag{3.7}$$

This makes the exact knowledge of the TTF in principle unnecessary for quantitative MFM. Nevertheless, sometimes it is of importance to have a good estimate of the stray field produced by the MFM tip. Therefore the exact form of the ICF is given in the following part.

In Section 3.1.2 it was already introduced, that the detected component of the force gradient is given by $dF_n/dn = \mathbf{n}\nabla(\mathbf{n} \cdot \mathbf{F})$. The component of force, that contributes to the cantilever deflection is $F_n$ and the component of the force gradient is the one normal to the cantilever [Rug90]. In the experimental situation the cantilever is usually tilted with respect to the surface normal by some degrees (between 10° and 12°), which has a noticeable effect on the measured image (see Figure 3.3 (a)). The canting between lever and surface normal is given by the angle $\theta$, which is included in the vector $\mathbf{n} = (0, sin\theta, cos\theta)$. Considering the canting in equation (3.6) and inserting equation (1.28) gives:

$$\frac{d\hat{F}_n}{d\ n} = -\mu_0 \hat{\sigma}^*_{sample}(\mathbf{k}) \cdot \mathbf{n}\nabla\mathbf{n}\frac{\nabla}{k^2}\frac{\partial\hat{H}^{tip}_z}{\partial z}(\mathbf{k}, z). \tag{3.8}$$

This equation suggests to define a lever canting function LCF of the following form[3]:

$$\mathrm{LCF}(\mathbf{k}, \theta) = (\mathbf{n}\frac{\nabla}{k})^2. \tag{3.9}$$

In Figure 3.3 the effect of the lever canting is visualized. The scan direction was parallel to the x-axis and $\theta = 12°$. The canting of the lever has been corrected by dividing the measured image by the LCF. The effect of the canting manifests itself in an asymmetry of the domain contrast, which is clearly reduced after removing the canting.

The full definitions of the two ICFs can be now given by (see equations (2.12) and (2.13)):

$$\mathrm{ICF}_{\Delta\phi} = -\mu_0\frac{Q}{c}\mathrm{LCF}(\mathbf{k}, \theta)\frac{\partial\hat{H}^{tip}_z}{\partial z}(\mathbf{k}, z) = -\mu_0\frac{Q}{c}\mathrm{LCF}(\mathbf{k}, \theta)\mathrm{TTF}(\mathbf{k}, z), \tag{3.10}$$

$$\mathrm{ICF}_{\Delta f} = -\mu_0\frac{f_0}{2c}\mathrm{LCF}(\mathbf{k}, \theta)\frac{\partial\hat{H}^{tip}_z}{\partial z}(\mathbf{k}, z) = -\mu_0\frac{f_0}{2c}\mathrm{LCF}(\mathbf{k}, \theta)\mathrm{TTF}(\mathbf{k}, z). \tag{3.11}$$

In accordance to the formerly introduced notation for the tip stray field gradient as convo-

[3] In all works published by *Hug et al.* the definition of LCF is the square root of the definition given here. Since there were no static measurements in this work it is reasonable to define the LCF as stated above.

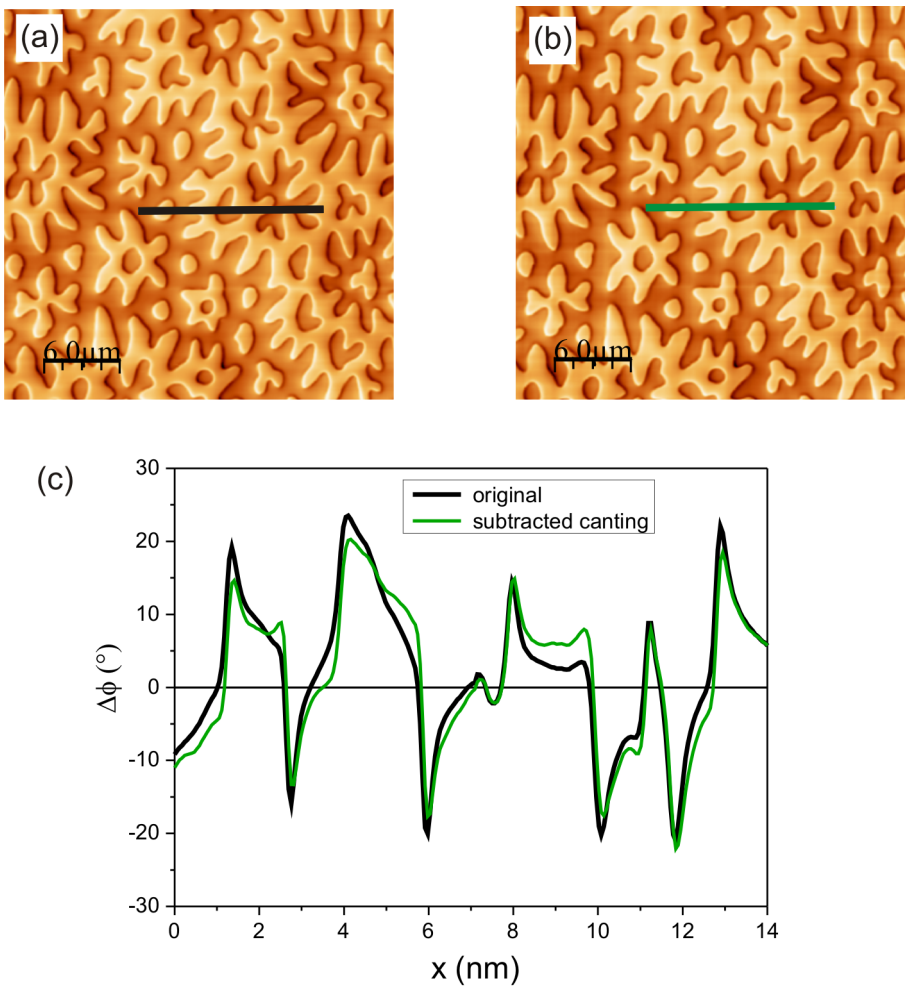


**Figure 3.3:** The effect of the lever canting. (a) Measured MFM image with a cantilever canting of 12° with respect to the fast-scan axis along the x-direction. (b) Removed canting by division of image *a* by the LCF. (c) Line profiles in image (a) and (b) along the marked line.

lution operator (RSTF), we define the abbreviation **RSICF** for the real space instrument calibration function:

$$\mathrm{TTF}(\mathbf{k}, z) \xrightarrow{IFT} \mathrm{RSTF}(\mathbf{r}, z) = \frac{\partial H_z^{tip}}{\partial z}(\mathbf{r}, z), \tag{3.12}$$

$$\mathrm{ICF}(\mathbf{k}, z) \xrightarrow{IFT} \mathrm{RSICF}(\mathbf{r}, z). \tag{3.13}$$

The RSTF symbolizes the pure tip property, while the RSICF includes the instrument specific characteristics. For a quantitative MFM study, where the calibration and the measurement are performed with the same instrument, it is sufficient to determine the RSICF.

### Practical considerations: the need of a specific deconvolution algorithm

With the introduction of the transfer functions, which are responsible for the contrast formation in MFM, it seems now obvious, how the frequency and phase shift equations (3.6) and (3.7) can be solved inversely in Fourier space: by division with the ICF. Nevertheless, any attempt to directly implement this approach numerically will fail for experimentally measured data and in many cases also for ideal model data. Explanations on the principal difficulty of inverse solutions of such convolution problems were given in the first section of this chapter. The most important obstacle for the inversion constitutes the fact, that the ICF can contain zeros, making the direct division impossible. And even if this is not the case and the division is possible, due to the discrete nature of the problem, it can be that the numerical noise corrupts the signal, so that no physical meaningful conclusion can be drawn from the inverse solution even though it is mathematically correct. This is for example the case, if the ICF gets too small in the high frequency range. Furthermore, in measured data additional experimental noise is present and the situation becomes even worse, so that also for highly resolving ICFs the images can not be inversed directly. In Figure 3.4 these problems are illustrated for the simple case of a square-shaped object and a RSICF(x,y) which has the form of a Gauss function. The matrices contain $200^2$ pixel and two different RSICFs were assumed with Gauss functions of width w = 5 pixel and w = 1.4 pixel, respectively. Images have been calculated by convolving the object with the RSICF. In one case statistical noise (10 % of the original signal) has been added to the so obtained artificial MFM image to illustrate the huge impact on the solvability of the problem. The reason for the noise amplification can be seen, when considering a simplified form of the equation for contrast formation including the degradation process due to noise [Sib05]:

$$\hat{\mathrm{I}} = \hat{\mathrm{N}}(\hat{\mathrm{O}} \cdot \mathrm{ICF}) \tag{3.14}$$

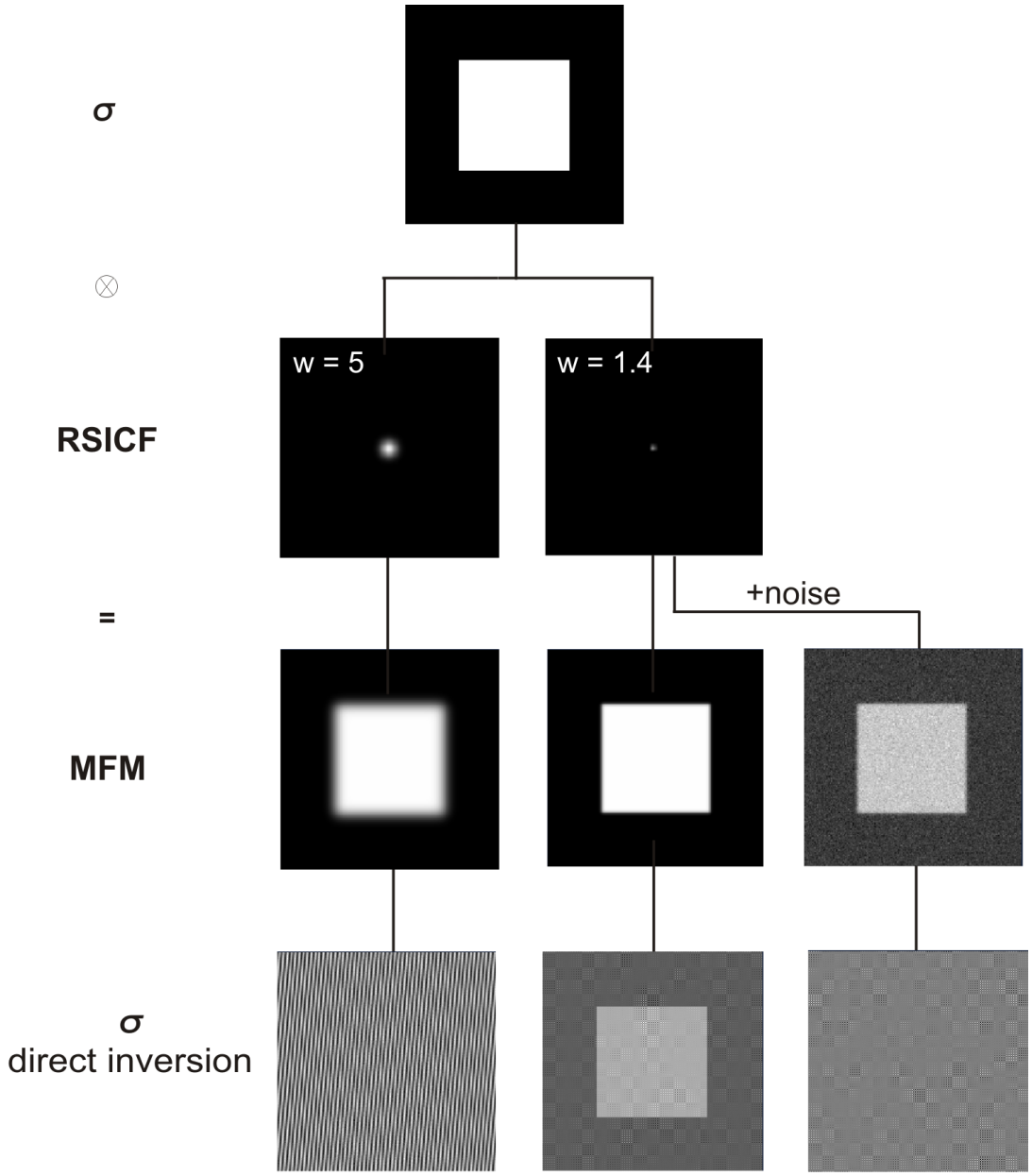


**Figure 3.4:** The difficulties arising from the direct division of an artificial MFM image by a Gaussian type ICF in Fourier space. The artificial MFM images were produced by convolving a square-shaped object with a Gauss function of width w = 5 pixel and w = 1.4 pixel. The results of a direct inversion by division of the image with the ICF are given in the last row. A meaningful result is only achieved in the case of a very sharp RSICF and in the absence of noise (last row, middle image). The other two cases show only noise.

where $\hat{I}$, $\hat{N}$, $\hat{O}$ stand for the Fourier transforms of the MFM image, the noise and original magnetic object, respectively. The inverse solution includes the division by $\hat{N}$, which typically contains small numbers leading to huge fluctuating numbers in the result. Only in the absence of noise and if the original square object is only slightly blurred by the RSICF, a solution can be obtained by direct division.

The problem of image restoration is a well-known issue, especially in light microscopy, where the aim is the increase of resolution in images, which have been blurred by a light source, that is not an ideal point source. Various deconvolution procedures have been developed for the special requirements of this kind [Ber95, Sib05, CLA10]. However, for the special case of MFM only one publication by *Candocia et al.* [Can04] could be found, which explicitly concentrates on finding a suitable deconvolution algorithm for MFM. The deconvolution approach is set up as a constrained optimization problem, but with the main focus on resolution rather than quantitative data evaluation.

Due to the above discussed practical difficulties of the numerical implementation of the transfer function theory introduced by *Hug et al.* [Hug98], the first step towards quantitative MFM had to be the selection of an appropriate deconvolution algorithm. The Wiener invert filter was found to be a well suited and simple method.

### The Wiener invert filter

The Wiener invert filter is a deconvolution approach that relies on a filter developed by the mathematician Norbert Wiener in 1942 [Wie42]. The filter was originally developed to exclude noise from random vibrating mechanical or electrical systems. While the Wiener filter is applied for the denoising of a detected signal, the Wiener invert filter or Wiener deconvolution aims the reconstruction of a blurred signal by including the noise characteristics of the system.

The Wiener deconvolution belongs to the statistical methods. Its basic feature is that it takes the random nature of the noise into account. It works in the frequency domain, attempting to minimize the impact of deconvolved noise at frequencies which have a low signal-to-noise ratio. The basic assumptions are that the noise is of Gaussian type with zero expectation value and that the noise and the object are independent [Ber95]. That this holds for MFM imaging will be proven by noise measurements given in Section 3.3.

The Wiener restoration technique estimates an object $\hat{O}$, such that $ICF * \hat{O}$ approximates the MFM image in a least square sense [Sib05]. The filter operation is given by [Ber95]:

$$\hat{O}(\mathbf{k}) = I(\mathbf{k}) \left[ \frac{\mathrm{ICF}^*(\mathbf{k})}{|ICF(\mathbf{k})|^2 + \frac{N(\mathbf{k})}{O(\mathbf{k})}} \right]$$

where $\frac{N}{O}(\mathbf{k})$ denotes the noise to signal ratio. This ratio is given as frequency dependent but can be approximated by a constant noise to signal ratio [Bán05, Bán06]. In the following the ratio will be referred to as the Wiener filter input parameter $\epsilon$.

In order to make the Wiener filtering compatible with the task of quantitative MFM, the algorithm had to be embedded in a procedure taking account of the specific requirements in MFM. This will be explained in detail in the following section.

## 3.2 Tip calibration: Adapted Wiener deconvolution

### 3.2.1 Details of the procedure

The calibration of the MFM probe constitutes a crucial part for quantitative MFM. Only the thorough knowledge of the tip properties can enable the correct deconvolution of the measured data. In this section, the focus is on the calibration by the transfer function method, as this is the only method, which allows the correct description of any kind of tips and is applicable in a very general way. The calibration within the point probe approximation will be explained in Chapter 4, where this approach is applied on special tips behaving very similarly to point probes.

In the framework of the transfer function approach a tip calibration procedure has first been introduced by *van Schendel* in his PhD thesis [vS99]. Since the deconvolution procedure used in this work differs from that of *van Schendel* the calibration routine is also modified. The numerical implementation was done within the development environment *SigMath* [Sas13b]. The algorithm for the Wiener invert filter was included from the Clarity open source library [CLA10][4]. Changes were only made concerning the zero-padding[5], which has been adjusted to the given magnetic problem (e.g. changed to padding with -1).

The single steps of the procedure are given in a form of a flowchart in Figure 3.6 with the main steps highlighted by numbers. The images resulting from the processing steps are given in Figure 3.7 (numbers according to Figure 3.6). In the following the description of the single steps refers to both figures. The first basic requirement for a calibration is a well-known reference sample with known effective surface charge map $\sigma^*_{eff}$ (or for the reciprocal case: the stray field). The used reference samples are introduced in detail in the next section. The calibration samples are thin films with an out-of-plane magnetization and zero remanence. This allows to apply a discrimination level to their MFM image, by

[4]The embedding of the Clarity library into the SigMath environment was done by Prof. Z. Sasvári (TU Dresden).

[5]The term *zero-padding* refers to the extension of a matrix by adding zeros.

setting a zero level exactly in the minimum between the two peaks of their histogram (step 1). The result is a binary charge map of the upper side of the film with step-like transitions between the domains (the step transition is given in Figure 3.5, blue solid line).

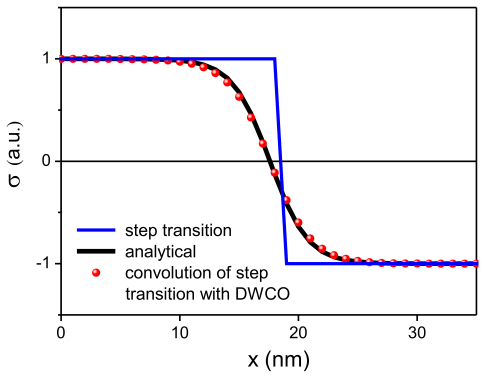


**Figure 3.5:** Comparison of the step-like domain transition (blue) with an analytically calculated (after equation 3.16) transition (black) and the transition obtained after applying the DWCO on the step-like transition.

To come closer to the real magnetization structure of the reference sample it is possible to include a Bloch type transition between the domains (step 2). Therefore, it is assumed, that such a wall correction can be achieved by the convolution of the binary charge map with a domain wall convolution operator (DWCO = f(x,y), in Fourier space: domain wall transfer function - DWTF = $f(k_x, k_y)$) such that [vS99][6]:

$$\sigma_{domains}(x, y) = \sigma_{binary}(x, y) \otimes \mathrm{DWCO}(x, y) \tag{3.15}$$

where $\sigma_{binary}(x, y)$ is the charge map with infinitely sharp transitions, $\sigma_{walls}(x, y)$ is the charge map with Bloch type transitions and $\otimes$ symbolizes the convolution operation. The form of a single planar 180° Bloch wall is given by [Hub98]:

$$\sigma(x) = \tanh\left(\frac{\pi x}{\delta_w}\right) \tag{3.16}$$

with the wall width for thin films with strong perpendicular anisotropy ($Q > 1$) defined as

$$\delta_w = \pi\sqrt{A/K_u} \tag{3.17}$$

[6]The idea was first introduced by *van Schendel* in his dissertation [vS99]. He offers an equation of the Fourier transform of the Bloch type wall, which has been expanded to the second dimension assuming rotational symmetry. The applicability was shown in the dissertation, as well as in a following dissertation in the same work group [Pil06]. Unfortunately, it was not possible to reproduce the result with the given function, therefore a domain wall convolution operator was derived in a similar way as proposed by *van Schendel*, but here in real space.

where $A$ is the exchange constant and $K_u$ the uniaxial anisotropy constant. The infinitely sharp transition is described with a scaled and shifted unit step function u: $2(u(x) - 0.5)$ [WIK13]. The extension of a Bloch type transition to the second dimension by assuming rotational symmetry finally gives [MAT]

$$\mathrm{DWCO}(x, y) = \left(\cosh\left(\pi\sqrt{x^2 + y^2}/\delta_w\right)\right)^{-1}. \tag{3.18}$$

The agreement between the so calculated domain transition and the analytical form as given in equation 3.16 is shown in Figure 3.5. The advantage of this convolution method is the possibility to include domain walls with a given geometry into domain patterns of almost arbitrary shape. The approximation stays valid as long as the domain width is large enough, so that the walls do not influence each other and are not too curved [vS99, Pil06]. The effect on the calibration image is shown in step 2 in Figure 3.7.

Step 3 in the calibration includes the bottom side charges of the thin film by multiplying $\hat{\sigma}(\mathbf{k})$ with the thickness factor $(1 - e^{-kt})$, where $t$ denotes the film thickness. The inverse Fourier transform gives the effective surface charge map $\sigma^*_{sample}$ as shown for step 3 in Figure 3.7.

With the so acquired $\sigma^*_{sample}$ of the reference, the MFM image can now be deconvolved with the Wiener invert filter to obtain the RSICF (step 4). In the previous section the input parameter $\epsilon$ of the Wiener invert filter was introduced. The parameter $\epsilon$ depends on the noise-to-signal ratio of the measurement. Since this is in general not known precisely, the parameter has to be optimized. This was done using a grid search and applying a root-mean square criteria. For this the Euclidean distance matrix $||N||_2$, also called $\mathrm{L}^2$ norm, of the original input image and the reconvolved image simMFM is calculated by

$$||N||_2 = \sqrt{\frac{1}{N}\sum_{i}^{N}\sum_{j}^{N}(\mathrm{MFM}_{i,j} - \mathrm{simMFM}_{i,j})^2} \tag{3.19}$$

and minimized. To suppress the noise present in the calculated RSICF it is further possible to average the values lying on a circle with the same radius making use of the rotational symmetry of the RSICF (circular averaging). The so obtained 1-dimensional vector can be subsequently circularly expanded, resulting in a smoother RSICF (step 5). The circular averaging is only advisable if the lever canting is negligible or is corrected and the RSICF shows a good rotational symmetry. Another possibility of reducing noise is to measure several MFM images on the reference sample and to average over the calculated RSICFs. In Figure 3.7 the RSICF is again convolved with $\sigma^*_{sample}$ (step 6). The comparison of the resulting image with the original input image as well as the comparison of the line profiles in the diagram in Figure 3.7 reveals an almost perfect recovery.

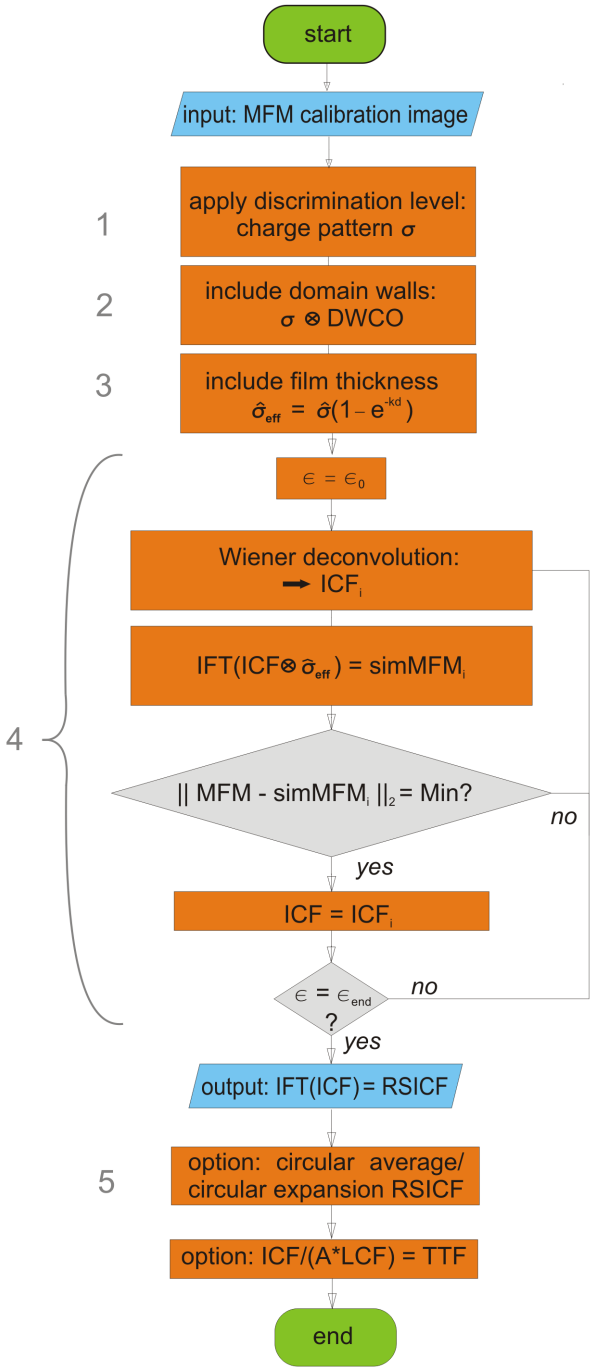


**Figure 3.6:** Flowchart of the calibration procedure including a modified Wiener invert filter as explained in the text. The abbreviation simMFM stands for the simulated MFM image obtained by reconvolving the surface charge pattern $\sigma(x, y)$ with the previously deduced RSICF(x,y). The abbreviation IFT stands for the inverse Fourier Transformation and $A$ in the last step of the flowchart denotes the prefactor depending on whether the frequency shift $\Delta$f or the phase shift $\Delta\phi$ is measured (compare Section 3.1.3).

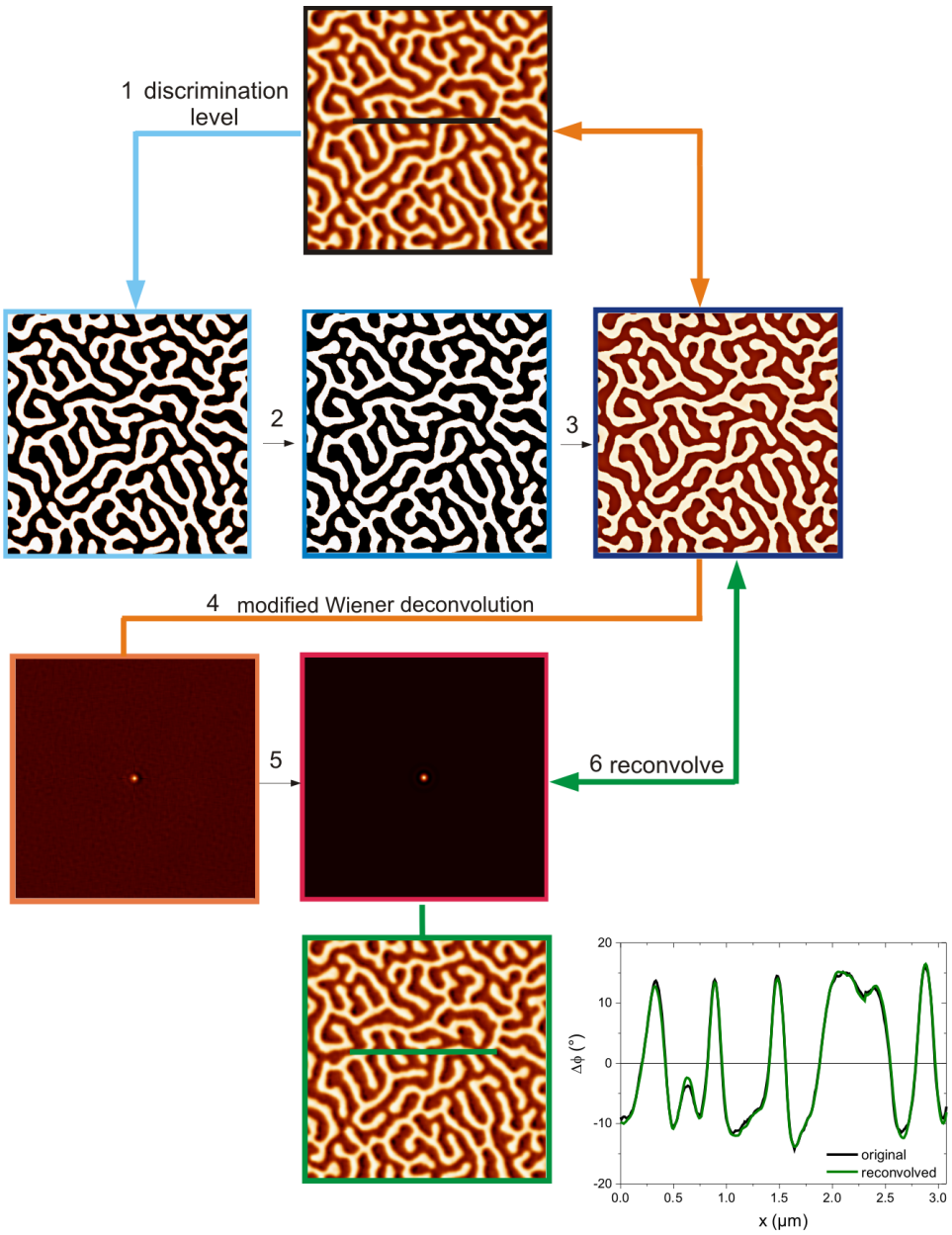


**Figure 3.7:** Visualization of steps contained in the calibration procedure using the example of a CoPt multilayer thin film reference sample: 1 application of the discrimination level to the MFM image of the reference sample, 2 convolution with the DWCO, 3 including the bottom charges resulting in $\sigma^*_{sample}$, 4 deconvolution with the modified Wiener invert filter of the MFM image with $\sigma^*_{sample}$, 5 circular averaging of the RSICF and expansion of the average vector, 6 reconvolution of $\sigma^*_{sample}$ with the circular averaged RSICF. The diagram shows a comparison of a line profile in the original MFM image (black) and the reconvolved MFM image (green).

### 3.2.2 Evaluation of possible errors

Quantitative conclusions from MFM images applying the introduced procedure are only meaningful, if the error in the calibration and evaluation method can be estimated. The occurring errors are of different origin and nature. Two main sources have to be separated: the errors due to the numerical deconvolution procedure and the experimental errors. The pure numerical errors can be estimated by calculating the RSTF as described in Section 3.2. The obtained RSTF is then again convolved with the charge map to simulate the MFM image. The results are given in Figure 3.8. Calculating the difference between these two images and applying the $L^2$-norm as defined in equation (3.19) to the difference image and to the original image gives an error of 7.6 %. This error is a result of the numerical inaccuracies due to the Fourier transformation of a finite non-periodic signal, rounding errors due to limited accuracy available in the computer and errors due to the low pass nature of the TTF. The latter means, that the TTF function has a certain frequency band limit. If the surface charge map contains frequencies beyond this band limit these frequencies will get lost and it is not possible to reconstruct them. An improvement of the numerical error could only be achieved for the rounding errors. The Wiener invert filter algorithm as provided by the Clarity library [CLA10] works with float numbers, which have only half the accuracy of double numbers.

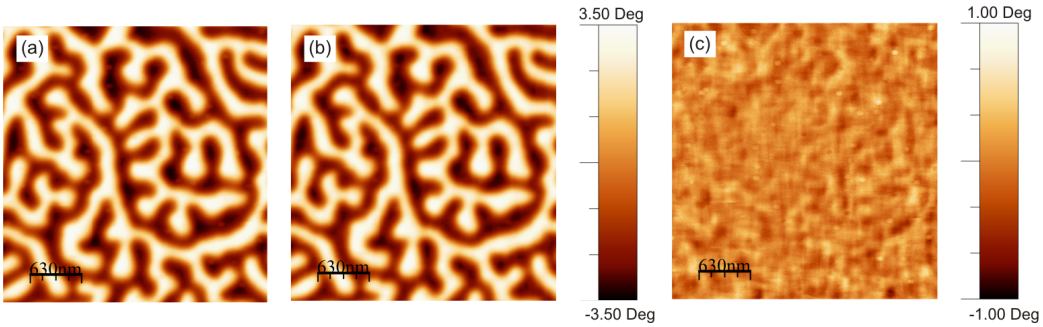


**Figure 3.8:** Simulation of an MFM image by convolution of the effective surface charge map with a RSICF obtained from the calibration procedure introduced in Section 3.2 and comparison with the measured image: (a) experimental MFM image, (b) simulated MFM image, (c) difference image

The experimental error for the measurements at the DI 3100 instrument is estimated by measuring the RSTF several times on the same reference sample in varying positions. The chronological order of the maximum value of the obtained RSTFs of two independent measurements with two different tips is given in Figure 3.9 (a) and (b). The series given in Figure 3.9 (a) includes a dismounting and remounting of the tip from the tip holder after measurement number 13. The effect of this procedure is clearly visible in a jump of the measured RSTF maxima. The remounting of the tip seems to introduce major

changes in the obtained maximum value of the RSTF through slight orientation changes of the cantilever. Until the origin of the influence on the RSTF is not clarified in detail, it is advisable to perform the quantitative MFM imaging always together with the tip calibration in one experiment to avoid larger errors.

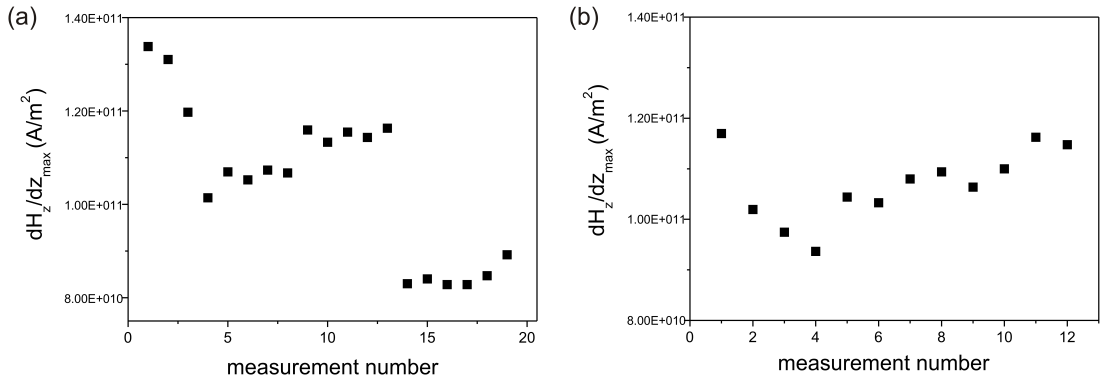


**Figure 3.9:** The maximum value of the RSTF ($dH_z/dz$) is plotted as a function of the measurement number. The chronology of two different ((a) + (b)) MFM experiment series obtained with two MFM probes is shown. The series in (a) includes a remounting of the tip, clearly visible in the jump of the RSTF maximum value (measurement number 13). The y-axis is stretched for better visibility.

The chronological sequences in the interval 1 to 13 and 1 to 12 in Figure 3.9 (a) and (b) indicate much smaller variations after a certain setting time. This may be ascribed to electronic instabilities, time needed for the laser as well as for the piezo scanners to stabilize after switching on the microscope. For a quantitative MFM experiment these larger errors can easily be avoided by measuring and evaluating several RSTF's until the results start to stabilize. However, there still seems to be a systematic increase of the RSTFs maximum value with time. The reason for this remains unclear. Due to this slope it is not useful to measure several RSTFs and average them as proposed by *van Schendel et al.* [vS00]. The error is rather minimized if the measurement on the unknown sample is as close as possible to the calibration measurement.

Even though it is obvious, that the error can be minimized by taking the specific properties of the experimental situation into account an error is calculated in the following assuming a statistical variation of the RSTFs. The real error will be smaller, when it is possible to follow the instructions given above for precise quantitative MFM imaging.

In order to quantify the error caused by varying RSTF's the standard deviation for the

whole matrices has been calculated by:

$$\sigma_{RSTF}(x,y) = \sqrt{\frac{1}{n-1}\sum_{i}^{n}\left(RSTF_i(x,y) - \langle RSTF(x,y)\rangle\right)^2} \tag{3.20}$$

where $n$ is the number and $\langle RSTF(x,y)\rangle$ the average of the acquired matrices. A line section through the maximum of the average and the standard deviation of the RSTF's from the whole measurement sequence in Figure 3.9 (b) is shown in Figure 3.10. The error related to the variation of the RSTFs has been calculated by convolving $\sigma_{RSTF}$ with the effective charge pattern. This results in a simulated error image with the units of a MFM measurement. Relating the root mean square (rms) value of the error image to the rms value of a measured MFM image (as given in Figure 3.8 (a)) gives a relative error of 3.3 %. This error value does not include systematic errors like a wrongly estimated effective surface charge map. The accuracy of the assumed surface charges is determined by the accuracy of the VSM measurement of the reference sample and the correctness of the assumption of a fully perpendicular magnetization alignment within the domains. A smaller systematic error has to be taken also into account for the inaccurate knowledge of the real domain wall width.

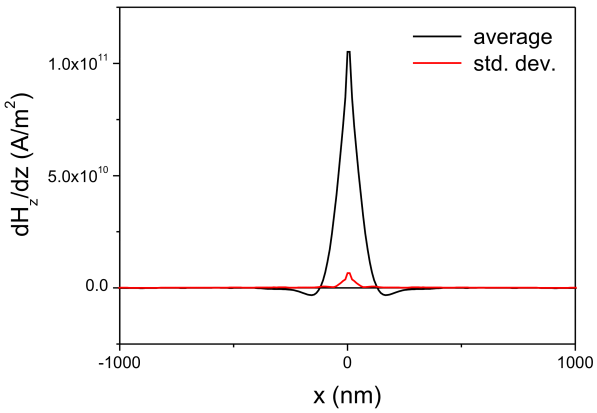


**Figure 3.10:** The average of the circular averaged RSTFs given in the chronology in Figure 3.9 (b) (black curve) and their standard deviation (red curve).

Summing up the above error considerations gives an estimated accuracy for the RSTF of about 10-15 %.

The next step for quantitative MFM image evaluation is to apply the so obtained RSTF to an unknown sample. A direct deconvolution would again lead to the numerical inaccuracies as discussed above. To avoid this all available knowledge about the investigated object must be combined in order to construct a reasonable model with few free parameters.

Then, a MFM image is calculated in a forward convolution with the RSTF and the model parameters are optimized in an iterative procedure until a match between measured and simulated MFM image is found. Direct deconvolution should only be used, if no a priori information about the sample is available.

## 3.3 Noise measurements

The applicability of the deconvolution procedure as introduced in Section 3.2 strongly depends on the nature of the noise present in the MFM image. One important source for noise is the oscillation of the cantilever due to thermal excitation. The minimal detectable force gradient is given by [Mey04]:

$$\left(\frac{\partial F}{\partial z}\right)_{min} = \frac{k}{\pi A_{osc}}\sqrt{\frac{2k_B T \Delta\omega}{\pi \omega_0 c Q}} \tag{3.21}$$

where $A_{osc}$ denotes the oscillation amplitude, $k_B$ the Boltzmann constant, $T$ the temperature and $\Delta\omega$ the bandwidth of the recorded deflection. The above equation makes clear, that a reduction of thermal noise can be achieved by measuring at low temperatures and under conditions which lead to a narrower resonance curve of the cantilever and therefore larger $Q$ values. In vacuum the $Q$ value is increased by several orders of magnitude [Nan11, Kap05a]. However, under experimental conditions, the sensitivity of the instrument is limited by the electronic noise of the detection system rather than by thermal noise [Mey04].

In order to identify the nature of the noise present in MFM, noise measurements have been performed. This can be done in various ways. One way is to set the scan range of the image to zero and to record the signal in a single point over a distinct time interval. Another possibility is the scanning of a nonmagnetic surface (here: $SiO_2$ substrate) in a realistic scan range, including the effect of the scanning procedure in the noise formation. The results of both approaches are given in Figure 3.11. Except for Figure 3.11 (a) the histograms of the noise measurements all show almost perfect Gaussian behavior. In Figure 3.11 (a) the noise data as acquired by scanning a 5 µm by 5 µm area of a $SiO_2$ substrate in the DI 3100 instrument under ambient conditions is given. Besides a pepper-salt pattern along the fast scan direction (parallel to the top/bottom side of the image) the noise image reveals jumps along the slow scan direction, which do not behave normally distributed. This manifests itself in a deviation from a perfect Gaussian bell-shaped distribution function (diagram in Figure 3.11 (a)). The reason for these line offsets may be attributed to the drift of the piezo scanner in z-direction. The jumps can be removed by applying a

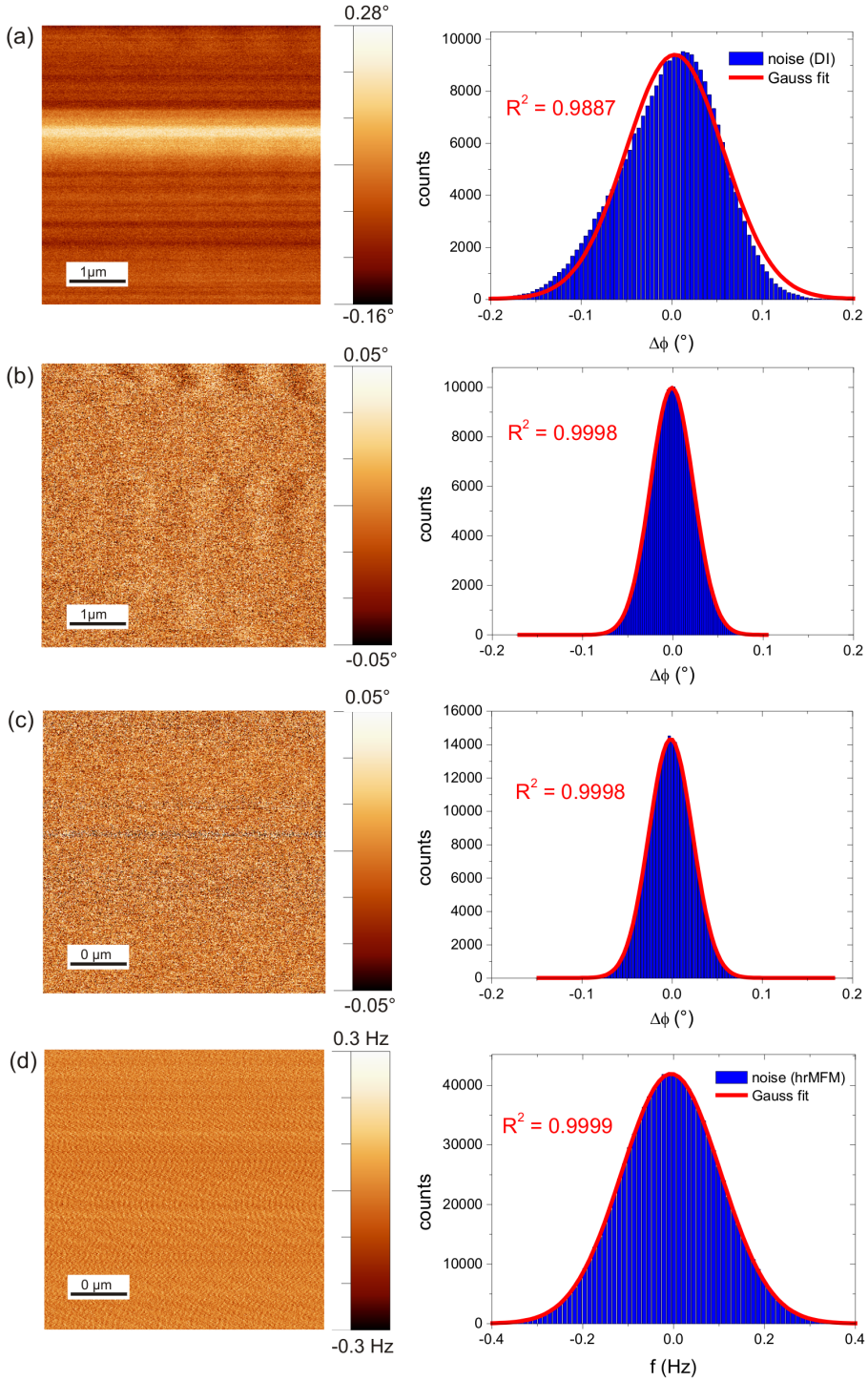


**Figure 3.11:** Noise measurements and their corresponding statistical properties (histograms). *DI 3100 MFM instrument*: (a) raw noise data acquired by scanning above a nonmagnetic $SiO_2$ substrate, (b) post processed noise image of (a), (c) noise image acquired by setting the scan range to zero (post processed), *hr-MFM instrument*: (d) raw noise data acquired by setting the scan range to zero. The parameter given in the diagram is $R^2$ - the quality of the fit ($R^2 = 1$ means a perfect fit).

so-called flattening procedure, where each scan line is fitted to a polynomial, which is subtracted. Furthermore, the average level of the scan lines is set equal to remove offsets. The flattening procedure is a quite invasive post processing operation and should be avoided, when performing quantitative MFM. However, if the scanner instabilities are large, the deconvolution can become almost impossible and only a flattening can help to improve the result. In the present work, the flattening was avoided in all quantitative MFM analysis unless particularly mentioned.

With the scanner uncertainties removed, the noise image still shows small overlayed higher frequencies in Figure 3.11 (b). The influence on the histogram is however negligible. Evaluating the noise characteristic without the scanner influence in lateral directions results in Figure 3.11 (c). The Gaussian behavior is similar to that of the scanned image. For comparison the scanned noise image is given for the hr-MFM instrument operated in vacuum. Here, the raw data is shown without any post processing. The image reveals some overlayed larger frequencies, but the histogram shows a better Gaussian shape with an $R^2$ value of 0.9999 than the histograms acquired in the DI 3100 instrument. As no jumps between the scan lines can be observed, it can be concluded, that the scanner works more stable and the z-drift is reduced compared to the DI instrument.

The above findings on the nature of the noise validate the application of a deconvolution procedure based on Wiener filtering.

## 3.4 MFM probes and their specific characteristics

For each MFM experiment the MFM probe has to be carefully chosen according to the magnetic properties of the sample and the information to be obtained. If the magnetic signal coming from the sample is very weak, the MFM tip should contain enough magnetically active material, so that the resulting signal is above the noise limit. If the magnetic signal of the sample is large enough, then the probe should be optimized regarding its resolution. For this a sharp tip coated with a thin magnetic layer is advantageous. While a sample with low coercivity requires a tip with a low moment in order to prevent an influence of the tip stray field on the sample magnetization, a sample with strong stray field requires a highly coercive tip.

The possibility to calibrate MFM tips enables the comparison of tip properties, such as their stray field geometry at arbitrary distances. Standard commercially available MFM tips have a pyramidal shape and are coated with a magnetic layer. A widely used tip is the pyramidal shaped MESP tip fabricated by Bruker (SEM image in Figure 3.12 (a)).

The silicon tip is coated with a magnetic Co-Cr layer. The tip radius is given by the manufacturer with 70 nm to maximum 100 nm.

A tip optimized for high lateral resolution is the hr-MFM tip of Team Nanotech. The probe is a cone shaped tip coated with a Co-alloy and a diameter smaller than 50 nm (Figure 3.12 (b)).

The SSS-MFMR tip manufactured by Nanosensors is also a tip optimized for high resolution. The end of the pyramid has an increased aspect ratio at the last few hundred nanometers of the tip. The enlarged SEM image in Figure 3.12 (c) (bottom image) shows a spike like pyramid end. The guaranteed tip radius is given by Nanosensors with 30 nm.

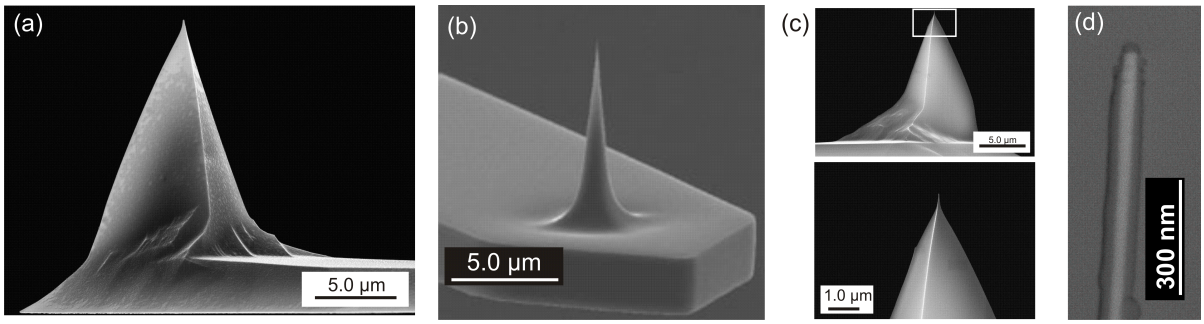


**Figure 3.12:** SEM images of the tips described in the text: (a) MESP tip, (b) hr-MFM tip, (c) top: overview of SSS-MFMR tip, bottom: enlarged tip end as marked by the white box in the top image, (d) FeCNT tip, the iron filling appears bright

Iron filled carbon nanotubes attached to standard AFM cantilevers are recently introduced MFM probes and are prepared by T. Mühl and coworkers at the IFW Dresden[7] (SEM image in Figure 3.12 (d)). Their specific properties will be introduced in detail in Chapter 4 and are here included only for comparison. The radius of the iron filling determined by SEM is 32 nm .

To quantify the performance of MFM tips, the calibration procedure introduced in the sections before proves as a powerful method. With each MFM tip a calibration measurement was conducted and the RSTF was subsequently deduced. To have a more intuitive physical quantity as the stray field gradient or effective surface charge, the stray fields of the tips were calculated from the RSTF directly at the end of the tips (z = 0 nm) and in a common MFM lift height (z = 50 nm). The results are shown in Figure 3.13 (a) and (b). For comparison the stray field of a magnetic point monopole and dipole in the same distance of 50 nm is given. In a distance of 0 nm the dipole and monopole can be considered as a delta function.

[7]prepared by Ch. Reiche in the group of Dr. T. Mühl, Leibniz Institute for Solid State and Materials Research Dresden - Institute for Solid State Research

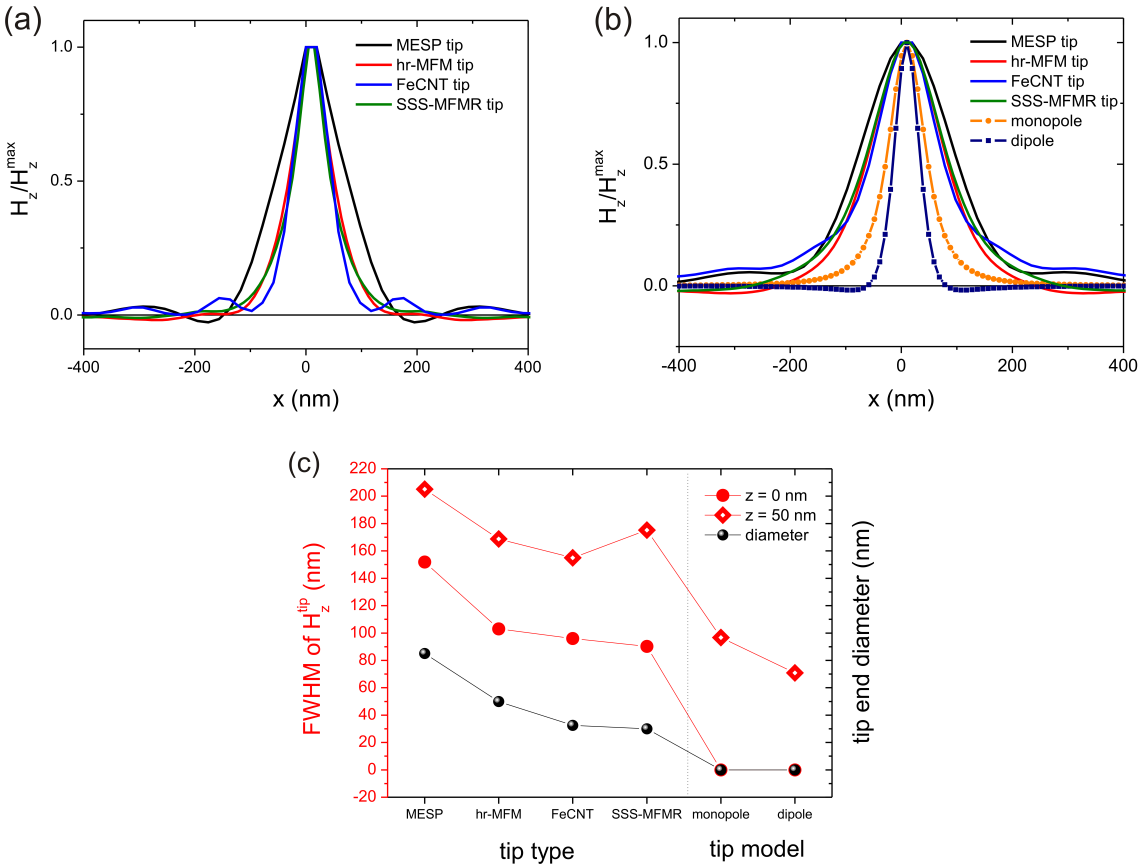


**Figure 3.13:** Normalized stray fields for the different tip types described in the text in a distance of (a) $z = 0$ nm and (b) $z$ =50 nm (here the stray fields for a monopole and dipole are added for comparison). (c) FWHM (red symbols and line) and tip diameter (black symbols and line) for the different tip types.

The stray fields of the hr-MFM, MESP and SSS-MFMR tip at zero distance, and the hr-MFM and SSS-MFMR tip also at 50 nm distance, possess two minima beside their maximum. This is the typical stray field geometry of a dipole as can be seen in Figure 3.13 (b). The stray field geometry of the FeCNT tip does not show this sign inversion, which is typical for a monopole behavior. In the case of an FeCNT tip this is expected due to the high aspect ratio and will be further proved in detail in Chapter 4. A quantification of the imaging properties of the so calibrated tips can be done for example considering the full-width half maximum (FWHM) of the stray fields [Kap05a]. The respective values are given in Figure 3.13 (c) for distances of $z = 0$ nm and $z = 50$ nm. In the same diagram, the diameters of the tips as given by the manufacturer or measured by SEM, are shown. The expected relation between the geometrical property of the tip apex and the stray field at the very end of the tips is obvious. Interestingly, for the FWHM values at distances further away this explicit dependency is broken. This can be understood, when considering the 3-dimensional extension of the tip geometry, which is gaining more influence at further distances. From the available commercial tips at the distance relevant for MFM imaging (z = 50 nm), the hr-MFM tip shows the best performance in the FWHM sense. This is the tip mainly used throughout this thesis.

The FWHM value alone can not be directly connected to the resolution of a MFM tip. The stray field contains also other frequencies, which are responsible for the resolution. In general, it can be easily seen from the theory of tip-sample interaction, that the resolution limit cannot be defined by characterizing the tip alone. Defining a resolution limit makes only sense for a specific MFM experiment where the signal strength of the sample is included. Absolute statements of manufacturers in a sense of guaranteed resolution are meaningless without the knowledge of the sample to which the tip will be applied and how large the noise level of the instrument is. However, a lower limit of resolvable wavelength could in principle be given by a cutoff frequency, which is difficult to determine in an absolute and instrument independent manner.

Figure 3.14 illustrates how a resolution limit can be estimated for different MFM experiments. Two MFM images of different samples are shown with different tips and in different lift heights. The circular magnetic object[8] imaged in Figure 3.14 (a) exerts a very low stray field and therefore the measured signal is very weak. The noise is clearly visible in the image. Contrary to this, the image of the reference sample (b) shows a strong contrast and noise is not visible on a first glance. Plotting the circularly averaged power spectrum densities (PSD) for both measurements enables the estimation of a resolution limit. The PSD of the circular magnetic object (Figure 3.14 (c)) shows a signal peak and a noise tail at higher frequencies. The intersection of the extrapolated noise and signal can be

[8]This is a patterned Co/Pt multilayer supplied by Dr. C. Hassel, address at that time: Universität Duisburg-Essen, AG Farle.

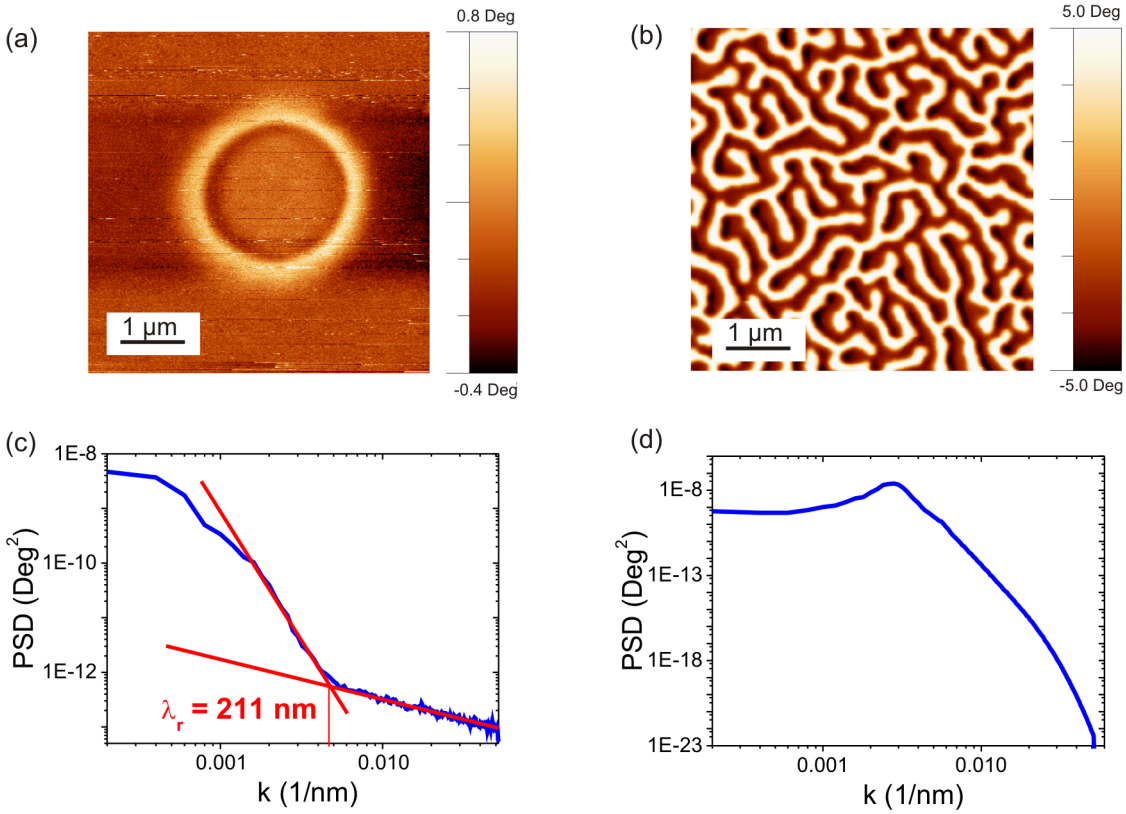


**Figure 3.14:** Comparison of the resolution of two different MFM images. (a) MFM image of a circular magnetic object, (b) MFM image of the reference sample, (c) circularly averaged power spectrum density (PSD) of (a) and resolution estimation by extrapolating the noise tail back into the signal region, (d) circularly averaged PSD of (b).

defined as a resolution limit. From this point on the noise dominates the signal. For the given example this leads to a minimum resolvable wavelength of 211 nm. The half of this wavelength gives the minimum distance of two features, which can be distinguished in this MFM image.

The PSD of the image of the reference sample (d) does not show any noise tail at high frequencies. Obviously the signal for all measured wavelengths of the reference sample is above the noise level. This means, that this MFM experiment resolves all wavelengths up to the step size (the scan size of the image divided by the number of recorded points) of the measurement, which was 10 nm in this measurement.

## 3.5 Calibration samples

The samples used as references in this work are magnetic multilayers with strong perpendicular anisotropy. The multilayers consist of Co/Pt stacks in one sample and Co/Pd stacks in the other sample. Both films are purely ferromagnetically coupled and the balance between the ferromagnetic exchange, anisotropy and dipolar energy results in the well-known labyrinth-domain pattern [Hel07] for both samples.

In order to quantify the strength of the perpendicular anisotropy the dimensionless Q-factor can be calculated from the ratio $K_u/K_d$, where $K_d = J_s^2/2\mu_0$ is the maximum energy density for a fully perpendicular magnetization in the thin film and $K_u$ the uniaxial perpendicular anisotropy as measured for the particular film [Hub98]. For $Q > 1$ the magnetization is aligned along the surface normal of the multilayer. The film architectures and the corresponding magnetic properties are given in Table 3.1. The Co/Pd sample was

**Table 3.1:** Reference samples used in the present work, where t denotes the total thickness of the magnetic layer.

| **architecture** | **t [nm]** | $\mathbf{M_s}$ $[\frac{\mathbf{kA}}{\mathbf{m}}]$ | $\mathbf{Q} = K_u/K_d$ |
|---|---|---|---|
| Pd(20nm)[Co(0.4nm)/Pd(0.7nm)]$_{80}$+Pd(6nm) | 88 | 710 | 1.7 |
| Pt(5nm)[Co(0.4nm)/Pt(0.9nm)]$_{100}$+Pt(2nm) | 130 | 554 | 2.7 |

provided by *O. Hellwig* (HGST - Western Digital). The magnetic multilayer was deposited onto a $Si_3N_x$ coated Si substrate by magnetron sputtering using a con-focal sputter-up geometry in a ATC 2200 system from AJA International [Hel07]. The Co/Pt sample was provided by *D. Makarov* (Institute for Integrative Nanosciences - IFW Dresden). The magnetic multilayer was deposited onto a Si-$SiO_2$ substrate by magnetron sputtering.

## 3.6 Detection of tip-sample modification

The assumption of a rigid tip and sample magnetization during the whole MFM measurement is a basic precondition for the applicability of the quantitative evaluation procedure introduced in this thesis. A method to check the validity of this is to test if the decay behavior of the measured signal follows the exponential law given in equation (1.26) [vS99]. This is done by acquiring MFM images at exactly the same position but in varying heights. The MFM image obtained at lower lift height can then be used to calculate the MFM image at further distance applying the theoretical decay behavior in Fourier space. If the equation holds, the difference between measurement and calculation should be zero. Unfortunately, the positioning errors due to lateral drift of the piezo scanner, especially in the DI 3100 instrument operating under ambient conditions, are so large, that no conclusion could be drawn from simply subtracting the images. Therefore, only single lines along the fast scan direction are subtracted after careful alignment. The result is given in Figure 3.15. The first measurement was taken at 30 nm distance (black line in Figure 3.15) and the second in 50 nm distance (blue line). The MFM signal in 50 nm distance is calculated from the 30 nm measurement (red line) and the comparison reveals a very good agreement. The deviations can originate from both numerical inaccuracies and tip-sample interactions. Since no larger deviations can be observed, it can be concluded, that the tip and sample magnetization are very likely to be rigid. Nevertheless, this test is not a proof, only a strong hint, that tip-sample interactions can be neglected.

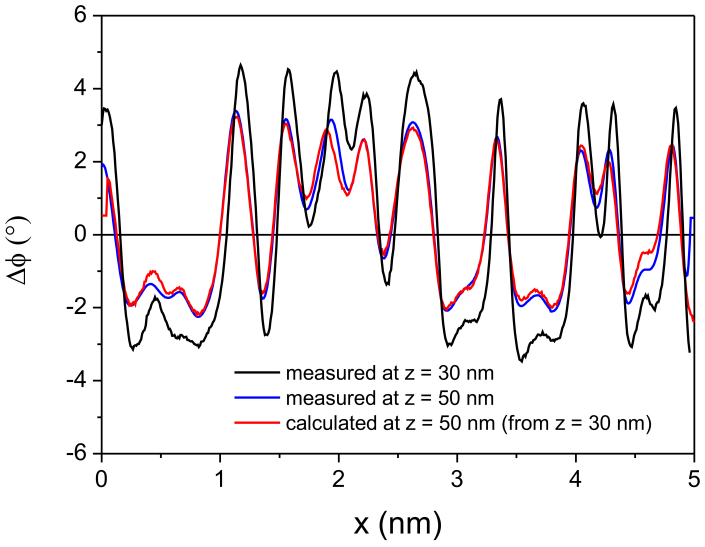


**Figure 3.15:** Comparison of measured MFM signal obtained on the reference sample (compare Figure 3.14 (b)) with 50 nm lift height with the MFM signal calculated from an MFM measurement on the same lateral position but in 30 nm lift height.

# 4 Quantitative MFM with iron filled carbon nanotube sensors

The idea to use iron filled carbon nanotubes (Fe-CNT) as MFM probes was first introduced in 2006 by the group of *T. Mühl* [Win06]. As already discussed in the previous chapter (Section 3.4) these probes reveal a great potential for high spatial resolution. Besides, the carbon shells around the iron nanowires provide a high wear resistance and oxidation protection. This results in an extraordinary long lifetime of the probes and very stable magnetic properties [Wol08]. However, the most important property, which makes the Fe-CNTs so interesting for the use as MFM probes is the high aspect ratio of the iron nanowire. With this the magnetic poles at the wire ends are well separated and it can be presumed that the part interacting with the stray field of the sample behaves as a magnetic monopole [Voc10]. The first part of this chapter introduces a method to prove the monopole behavior of these novel MFM probes (Section 4.1). The availability of an MFM probe with real monopole behavior can reduce calibration efforts enormously and enables a fast and straightforward quantitative MFM image evaluation within the point probe model (introduced in Section 3.1.2). An application of this will be given for the local magnetization determination of a Co/Pt/Ru multilayer (Section 4.1.3).

Besides the advantages for quantitative MFM, a monopole-like Fe-CNT probe opens the way for other interesting applications not realizable with conventional tip shapes. A bimodal MFM method was introduced recently by *Mühl et al.* [Müh12]. Depending on the flexural vibration mode of the cantilever, the Fe-CNT probe is sensitive to magnetic field derivatives parallel or perpendicular to the sample surface. Applying the theory described in the first chapter (Section 1.2.3) enables the comparison of the measured contrast with a calculated MFM signal. The results of this are discussed in the second section of this chapter (Section 4.2).

## 4.1 The monopole character of Fe-CNT sensors

### 4.1.1 Calibration within the point probe approximation

It is known from the work of *Lohau et al.* [Loh99] and *Kebe et al.* [Keb04] that the calibration parameters of standard commercial MFM tips within the point probe approximation are not independent from the applied calibration structure. Therefore the focus of the following experiments is to test this dependency for an Fe-CNT probe and to compare its behavior to that of a commercial MESP type tip.

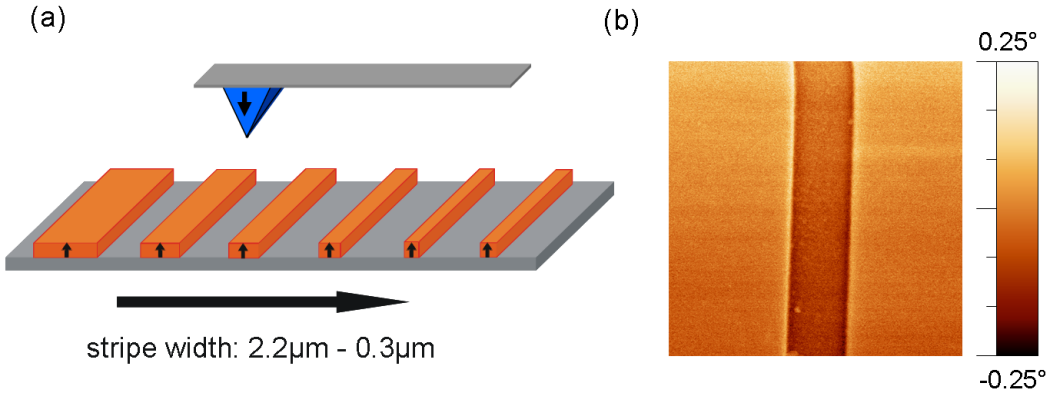


**Figure 4.1:** (a) Sketch of the calibration sample consisting of 6 CoPt stripes with varying width. (b) MFM image of a 2.2 µm stripe.

*Lohau et al.*, *Kebe et al.* and *Wolny et al.* calibrated MFM tips with the stray fields of current carrying wires. These can be well described analytically by applying Biot-Savarts-law [Loh99, Keb04, Wol10]. The present work utilizes ferromagnetic structures as calibration samples. More precisely, 6 $(Co/Pt)_7$ multilayer stripes with varying width from 2.2 µm down to 300 nm and a height of 14 nm (see the sketch in Figure 4.1 (a)) were chosen. These stripes possess a well defined stray field and are therefore suitable reference structures.

The reference sample was prepared by alternating electron beam evaporation of Co and Pt and high resolution electron beam lithography plus lift-off by C. Hassel[1] [Has06]. In-plane magnetoresistance measurements revealed an effective perpendicular magnetic anisotropy constant of $K_{eff} = 1.05$ x $10^6$ J/m$^3$ and a saturation magnetization of $M_s = 1080$ kAm$^{-1}$ was obtained by SQUID measurements (conducted by C. Hassel). With this a $Q$ value of

[1] adress at that time: Dr. C. Hassel, Universität Duisburg-Essen, AG-Farle: Struktur und Magnetismus nanoskaliger Systeme

about 1.5 [$Q = K_{eff}/\frac{1}{2}\mu_0 M_S^2$] is found, which indicates that flux closure domains should not be present. The remanent state after perpendicular saturation is single domain as can be clearly seen in the exemplary MFM image of the 2.2 µm wide stripe (Figure 4.1 (b)). Before the measurement the tips and stripes were magnetized in the same direction, thus an attractive interaction is expected. In earlier calibration measurements it turned out that the difference in electrostatic potential between the CoPt stripes and the substrate lead to a non-negligible effect on the measured curves. With the deposition of a few nanometers of carbon on top of the whole sample, the potential could be equalized between substrate and stripes.

The stray field gradient of the perpendicular magnetized stripes is calculated by numerically summing up the surface charges at the top and bottom layer of the magnetic thin film. Therefore the second part of equation (1.10) is utilized in a discretized form. The lateral distribution of the charges has been deduced from the measured topographic signal (the AFM image) by applying a discrimination level. With this it is possible to model and fit whole MFM line sections to the measured data, going beyond the single point fits introduced by *Lohau et al.*, *Kebe et al.* and *Wolny et al.* [Loh99, Keb04, Wol10].

Within the monopole model the equation for the MFM signal reads:

$$\Delta\phi(x,y,z) = -\mu_0 \frac{180^\circ}{\pi} \frac{Q}{c} q \frac{\partial H_z}{\partial z}(x,y,z+\delta_q) \tag{4.1}$$

and for the dipole model:

$$\begin{aligned}\Delta\phi(x,y,z) = -\mu_0 \frac{180^\circ}{\pi} \frac{Q}{c} \Bigg[ & m_x \frac{\partial^2 H_x}{\partial z^2}(x,y,z+\delta_m) \\ & + m_y \frac{\partial^2 H_y}{\partial z^2}(x,y,z+\delta_m) \\ & + m_z \frac{\partial^2 H_z}{\partial z^2}(x,y,z+\delta_m) \Bigg].\end{aligned} \tag{4.2}$$

For the fit according to the dipole model the direction of the vector **m**, its length and its position $\delta_m$ within the tip are set as free parameters. In the case of the monopole model the fit parameters are only q and $\delta_q$.

The Fe-CNT tip used for these experiments was prepared by chemical vapor deposition (CVD) and attached to a standard AFM cantilever by *F. Wolny*[2] [Wol08]. The Fe-CNT consists of a carbon shell with an iron filling of 2 µm in length and a radius of approximately 16 nm (see Figure 3.12). The commercial tip chosen for the comparative study was a MESP type tip as introduced in chapter 3 (Section 3.4 and Figure 3.12). Both tips were

[2]adress at that time: IFW Dresden, Institute for Solid State Research

magnetized along the axis perpendicular to the cantilever plane. The MFM measurements described in this section were carried out with the DI 3100 instrument in the tapping/lift mode.

### 4.1.2 Calibration results and discussion

An exemplary fit of MFM lines obtained with the MESP type tip and the Fe-CNT tip with the monopole and dipole model is shown in Figure 4.2. The measured MFM signal is averaged over approximately 50 lines to improve the signal-to-noise ratio. Both measured lines show similar characteristic features. Two peaks with inverse sign appear at the borders. Exactly at the sides of the stripe the signal is zero. To fit the measured MFM line of the MESP type tip within the dipole model an additional tilt of the moment (with respect to the sample normal) was included (19°) to account for the asymmetry of the peaks. This angle is a superposition of the cantilever tilt due to the measurement setup, which is in the range of 10°-12°, and the asymmetric shape of the pyramid which results in a small additional in-plane component of the tip stray field. The maximum deviation between the MESP type tip and the point dipole model can be observed in the center of the stripe. This can be attributed to the extended volume of the magnetic material of the MESP tip, which collects stray field contributions of the sample from further distances. With this a non-zero signal is detected in a region, where the stray field gradient itself is expected to be close to zero. However, the dipole model is the better choice out of the two point probe models for the MESP type tip. Only this model includes the vector characteristic of such a pyramidally shaped tip magnetization. The fit of the MFM signal obtained with the Fe-CNT tip shows an almost perfect agreement with the monopole model.

Both tip types have been fitted with both models, respectively. The results of the calibration procedure are summarized in Figure 4.3. Tip calibration parameters m, q and $\delta$ are plotted on a logarithmic scale as a function of the magnetic structure size to accommodate the large span of values resulting from the fit procedure. The MESP type tip shows an increase of the dipole moment and the corresponding $\delta$ with increasing structure size (Figure 4.3 (a) and (b)). The same is true for the monopole model (Figure 4.3 (c) and (d)). The tip parameters of the Fe-CNT tip show a slight increase with increasing stripe width within the dipole model (Figure 4.3 (a) and (b)) and stay constant within the monopole model (Figure 4.3 (c) and (d)).

The calibration results are as expected and, for the MESP type tip, in good agreement with values reported earlier for comparable tips [Keb04, Loh99]. They can be understood by means of a changing effective tip volume caused by an increasing decay length of the stray field when increasing the stripe (domain) width. Therefore the magnetic point charge

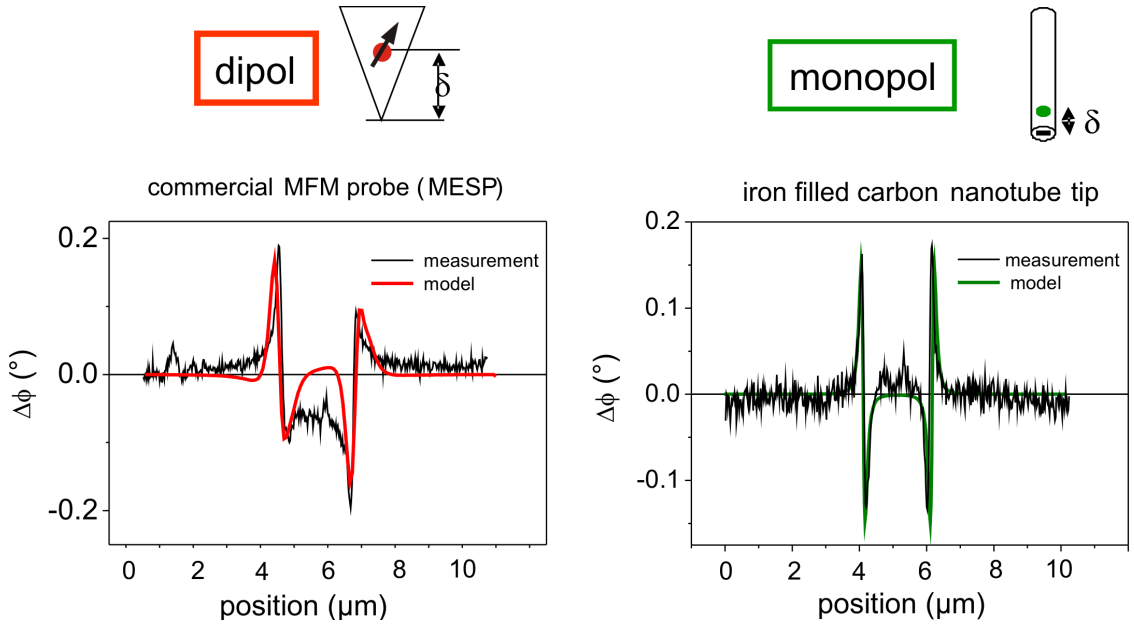


**Figure 4.2:** Exemplary fits of averaged line scans over the CoPt stripe with the dipole and monopole model for the MESP tip and the Fe-CNT probe.

position, which is located in the middle of the effective volume, moves upwards, increasing both $\delta$ and the tip moment. This behaviour holds for all tips which do not resemble a true point pole: the values for moment (m or q) and displacement ($\delta$) necessary to describe the tip response to the sample represent the properties of an extended tip by localizing these into one point. In case of varying stray field geometries the interaction volume in the tip is changing and therefore requires modified tip parameters [Loh99]. This makes the application of the point probe approximation to standard MFM tips rather difficult, since the tip has to be calibrated for each stray field configuration separately. In contrast to that, the Fe-CNT tip comes close to a true point monopole, whose properties are not expected to vary for different stray field geometries. These considerations are confirmed by the calibration data in Figure 4.3 (c) and (d). The charge and $\delta$ are constant for the Fe-CNT tip within the monopole model. Moreover the magnitude of the monopole moment $q = (0.8 \pm 0.2)$ x $10^{-9}$ Am is comparable to that expected from geometrical considerations ($q_{geom} = M_s^{Fe} \pi r_{tip}^2 = 1.4$ x $10^{-9}$ Am). Considering the thickness of the nanotube's carbon shell which is in the range of 30 nm a delta of $85 \pm 30$ nm is reasonable. Small diameter variations at the end of the iron filling can cause the deviation from the cylindrical geometry model. Within the dipole model (Figure 4.3 (a) and (b)) m and $\delta$ increase slightly, which results from the magnetostatic definition of the point dipole and the lateral extension of the iron filling (2 $\mu$m) in z direction. In contrast to this the iron filling with a radius of only 16 nm constitutes an almost perfect monopole in the x-y plane relative to the stripe dimensions ranging from 300 to 2200 nm.

From the above findings it can be concluded that for the Fe-CNT tips the monopole approximation is an absolutely adequate model which describes the tip entirely. This description is expected to stay valid as long as the nanowires diameter is much smaller than the characteristic lateral feature size of the sample's stray field distribution. Furthermore the length of the nanowire must be larger than the decay length of the sample's stray field [Hug98, Müh12].

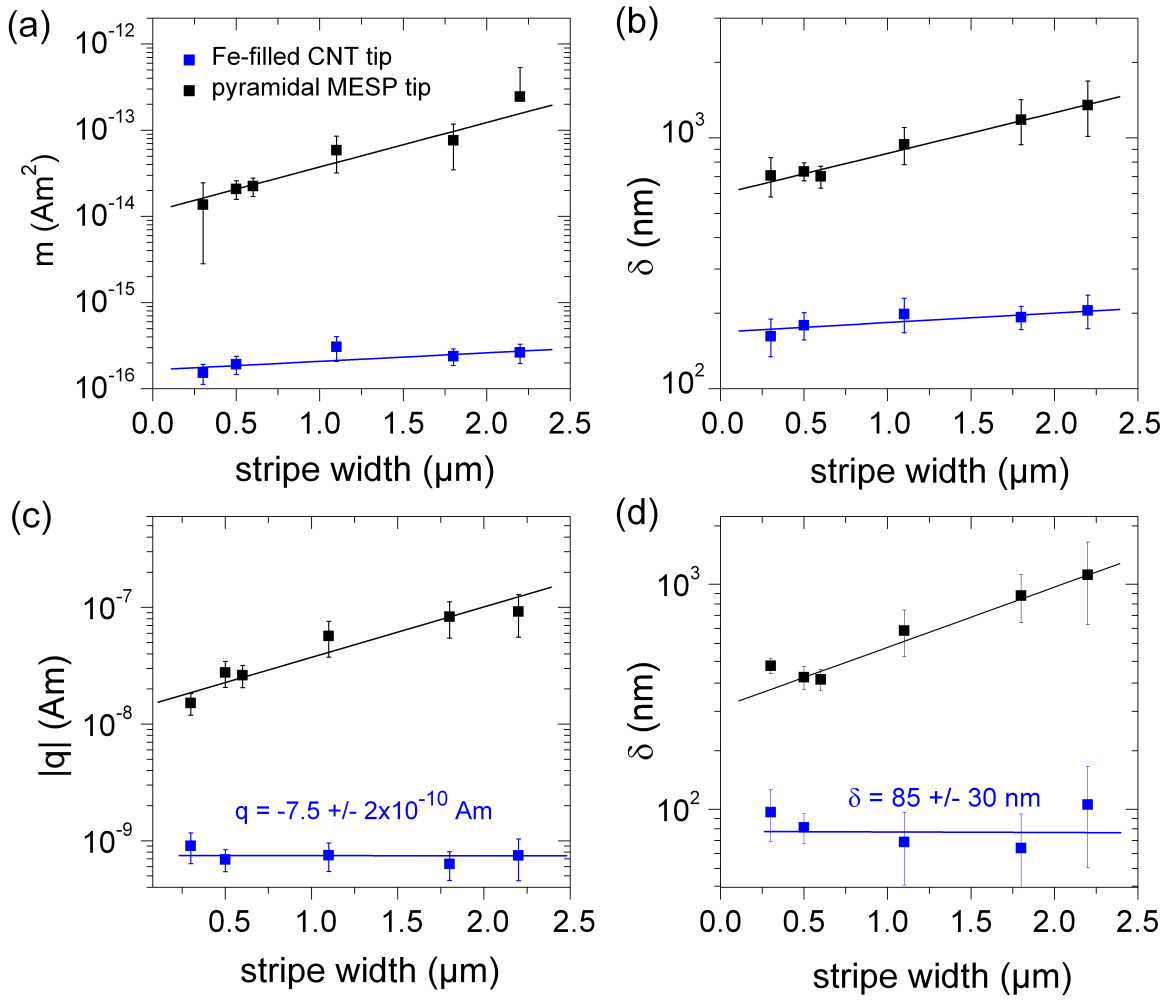


**Figure 4.3:** Calculated dipole (a) and monopole moments (c) and corresponding $\delta$ values ((b) and (d)) for the MESP tip and the Fe-filled CNT tip at an average lift height of 60-80 nm. Within the dipole model a tilt of 19° of the moment in the MESP tip was found and kept constant during the whole calibration procedure.

### 4.1.3 Quantitative MFM on a [Co/Pt]/Co/Ru multilayer

With the knowledge of the tip properties and its independence on the domain size, the Fe-CNT tip is used for quantitative imaging on a [Co/Pt]/Co/Ru multilayered thin film with the following architecture: $[(\mathrm{Co}(0.4\ \mathrm{nm})/\mathrm{Pt}(0.7\ \mathrm{nm}))_8/\mathrm{Co}(0.4\ \mathrm{nm})/\mathrm{Ru}(0.9\ \mathrm{nm})]_{18}$. The film was grown on a 2 nm Pt buffer layer and covered by 2 nm Pt (sputter deposited at 1 x $10^{-3}$ mbar Ar pressure and the following deposition rates: Ru = 2.5 nm/min, Pt = 4.4 nm/min, Co = 3.1 nm/min) (prepared by R. Kaltofen, IFW-Dresden). The ferromagnetic Co/Pt multilayer stacks possess a high perpendicular anisotropy. Despite the nonmagnetic spacer layer which mediates an antiferromagnetic interlayer exchange coupling between these ferromagnetic layers, in zero field the sample is in a ferromagnetic band domain state, where the perpendicular magnetization is correlated in vertical direction throughout the whole film, but forms neighboring domains with opposite magnetization direction and a domain width of about 180 nm (comparable to the sample described by *Bran et al.* [Bra09a]). The MFM image is shown in Figure 4.4 (a).

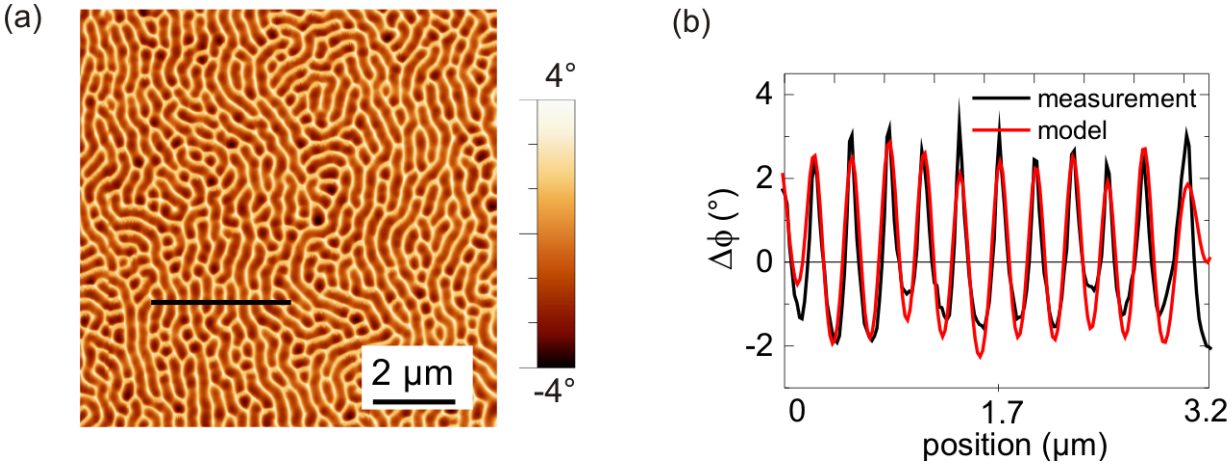


**Figure 4.4:** (a) MFM image of [Co/Pt]/Co/Ru mulitlayer in the ferromagnetic band domain state. (b) The simulation was performed along the black line drawn in the image. The diagram shows the comparison of the MFM signal with the simulation.

For the quantification of the measured MFM signal the procedure described previously is applied in the same manner but now keeping the tip properties constant and using the sample magnetization as fit parameter. In this case the sample stray field was calculated from a charge pattern that was derived by applying a discrimination level to the MFM data. The model assumes zero width domain walls. As tip parameters the mean monopole moment $q_{mean} = -7.5 \cdot 10^{-10}$ Am and the mean displacement $\delta_{mean} = 85$ nm were applied. The results of the modelling can be found in Figure 4.4. Optimum agreement is found when a sample magnetization $M = 440 \pm 135$ kA/m is assumed. This value can be compared to global VSM measurements which reveal a value of $M_s = 650 \pm 65$ kA/m. Obviously an

average deviation of each domain from the perfectly perpendicular magnetization orientation, expected from the interface anisotropy, is resolved. This is to a small extent caused by the non-vanishing width of the domain walls. The main contribution, however, comes from the competition between stray field ($K_d$) and anisotropy energy ($K_u$). Only for large perpendicular anisotropy $Q = K_u/K_d \gg 1$ the magnetization in a band domain structure is expected to lie fully perpendicular to the surface within each domain. For smaller $Q \geq 1$, the sample adopts a non-homogeneous magnetization structure with considerable in-plane components [Sti10]. In an early model assuming a one-dimensional charge pattern on the surface of an infinite plane *Williams et al.* [Wil49] estimated the influence of the effective permeability $\mu^* = 1 + K_d/K_u$ on the stray field energy and thus the magnetization within each domain. They derived a correction factor $a = 2/(1 + \sqrt{\mu^*})$ by which the perpendicular component of the magnetization is expected to change for $\mu^* \neq 1$. The perpendicular uniaxial anisotropy of the $[\mathrm{Co/Pt})/\mathrm{Co/Ru}]_{18}$ multilayer was determined by measuring the VSM in-plane (hard) and out-of-plane (easy) hysteresis loops and subtracting the shape anisotropy $K_d = J_s^2/2\mu_0$ from the area enclosed by the hard and easy axis loop [Bra09b]. The resulting correction factor is $a = 0.8$, which comes close to the value obtained from the quantitative MFM measurement, where $a = 0.7$.

The quantitative MFM analysis clearly identifies the non-perpendicular domain state, not obvious in a simple qualitative measurement. This demonstrates the necessity of a complementary measurement technique beside the volume averaging VSM for an overall interpretation of the magnetization status from a microscopic point of view and identifies Fe-CNT MFM probes as ideal monopole sensors for easy quantitative MFM measurements.

## 4.2 Inplane sensitive MFM with Fe-CNT sensors

### 4.2.1 Bimodal MFM technique

Several attempts have already been made to extend the MFM sensitivity additionally to the parallel or in-plane component (x or y-direction) of the stray field gradient [Abr88, Grü90, Fol00, Sas05]. All approaches have in common, that they orient the tip's stray field parallel to the sample surface to detect $\partial H_x/\partial z$. This can either be done by using MFM tips with high coercive coating and magnetizing the tip perpendicular to it's main axis [Grü90, Sas05], or by manipulating the tip coating by introducing a hole at the apex with a focused ion beam and with this changing the stray field geometry emanating from the tip [Fol00]. *Abraham et al.* [Abr88] used a wire tip and bend it in the preferred direction. All these methods require the modification of the tip and are thereafter restricted solely to the measurement of the in-plane component.

A new MFM method, including both, the in-plane and out-of-plane sensitivity, has been recently introduced by the group of *T. Mühl* and will be referred to as bimodal MFM in the following [Müh12]. The bimodal MFM technique is based on the monopole characteristic of a Fe-CNT probe, which is attached to a cantilever. Contrary to the previously published methods, the advantage of this techniques is the possibility to detect different components of the force gradient independently. The same MFM sensor can be used without further modifications. More precisely, the bimodal technique allows to experimentally detect

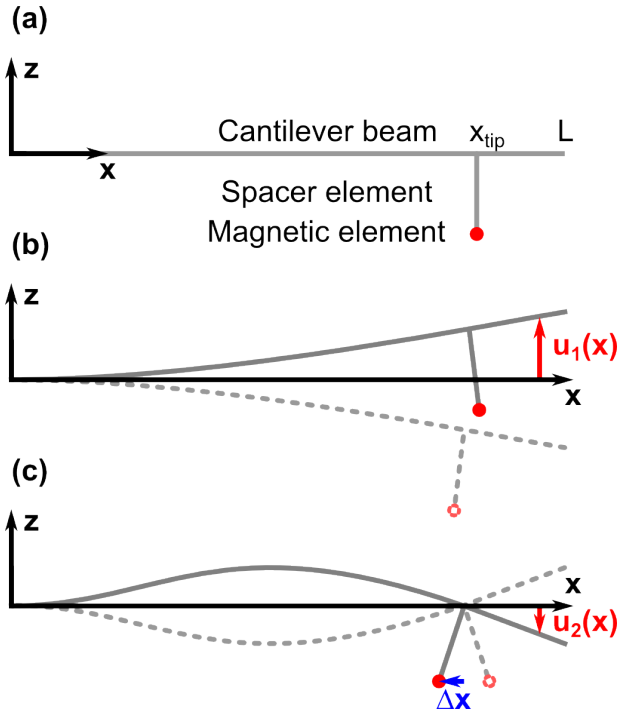


**Figure 4.5:** (a) Sketch of the static cantilever beam of length L. A magnetic element (red dot) is attached to a spacer element at the position $x_{tip}$. (b) first mode vibration - conventional MFM operation mode, out-of-plane sensitivity, (c) second mode vibration - enabling in-plane sensitivity. $u_1(x)$ and $u_2(x)$ denote the displacement of the cantilever at a position $x$. $\Delta x$ is the amplitude of the second mode oscillation (by courtesy of C. Reiche).

$\partial F_x/\partial x$ and $\partial F_z/\partial z$. According to the Maxwell equation $\nabla \mathbf{B} = 0$, the field components are connected, thus the force gradients are also interdependent and can be derived from each other. For quantitative comparison the respective force gradients have to be first calculated from the measured MFM signal according to

$$\Delta f = \frac{f_{mode}}{2c_{mode}} \frac{\partial F_n}{\partial n} \tag{4.3}$$

where $f_{mode}$ denotes the resonance frequency and $c_{mode}$ the dynamic spring constant of the chosen measurement mode. While $f_{mode}$ can be measured in each experiment, $c_{mode}$ has to be calculated for the given measurement mode.

The technical realization of the bimodal MFM method is based on the excitation of higher order flexural vibration. In the conventional MFM setup the cantilever is oscillated in the first flexural vibration mode, that is the vibration direction lies perpendicular to the sample surface (along the z-direction). In higher resonant modes certain locations along the cantilever length don't possess a $z$-displacement. At these nodes only the slope of the cantilever is oscillating. The idea of *Mühl et al.* [Müh12] was to transform such slope oscillations into x-direction oscillations by attaching the Fe-CNT sensor to a spacer element at the selected nodal point as shown in Figure 4.5. The spacer element was prepared by FIB-based deposition of a carbon pillar. SEM images of the spacer with the attached Fe-CNT can be found in Figure 6.9 (a) and (b). The stiffness of the spacer is sufficiently

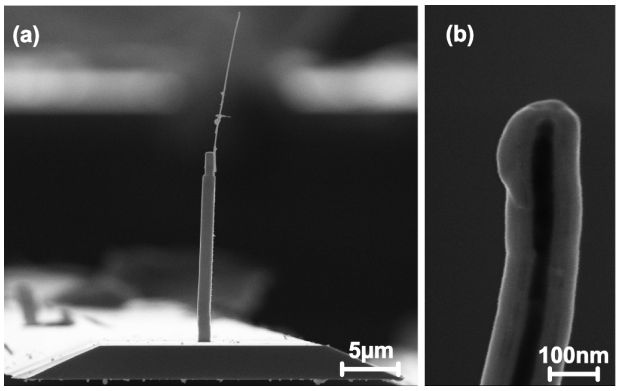


**Figure 4.6:** SEM image of (a) the spacer element and attached Fe-CNT and (b) a higher resolution image of the Fe-CNT sensor end (by courtesy of C. Reiche).

large, so that its resonance frequency exceeds the frequencies of the operated cantilever. This ensures, that the oscillation is fully transfered to the Fe-CNT (method description and more details can be found in [Müh12]).

For a quantitative comparison of the measured MFM signal in both vibrational modes, it is necessary to calculate the respective dynamic spring constant $c_{mode}$. This is done on the basis of the Euler-Bernoulli beam theory and an elastic energy consideration[3]. The approach allows implementing the horizontal displacement of the magnetic sensor along the cantilever length (see Figure 4.5). The resulting equation for the first mode dynamic spring constant at the location $x_{tip}$ of the Fe-CNT tip reads

$$c_{x_{tip},1}^{dynamic} = \frac{(u_1(L))^2}{(u_1(x_{tip}))^2} c_{L,1}^{dynamic} \tag{4.4}$$

where $u_1(L)$ denotes the envelope of the vertical displacement of the cantilever end and $u_1(x_{tip})$ the envelope of the vertical displacement of the cantilever at the tip position.

[3]The derivation was carried out by C. Reiche and T. Mühl, IFW-Dresden, Institute for Solid State Research and is to be published [Rei13]

$c_{L,1}^{dynamic}$ is the dynamic spring constant at the cantilever end. Accordingly, the equation for the second mode dynamic spring constant reads

$$c_{x_{tip},2}^{dynamic} = \frac{\left(u_2(L)\right)^2}{\left(\Delta x\right)^2} c_{L,2}^{dynamic}. \tag{4.5}$$

Again $u_2(L)$ denotes the envelope of the vertical displacement at the cantilever end and $\Delta x$ is the amplitude of the in-plane oscillation. $\Delta x$ is, within a small angle approximation, directly connected to the slope of the cantilever at the position of the tip given that the spacer element is rigid: $\Delta x = l_{dist} \cdot du_2(x_{tip})/dx$, with $l_{dist}$ being the distance of the magnetic element to the cantilever beam. The vertical displacements $u_n(x)$ follow from the Euler-Bernoulli Beam theory for the case of a cantilevered beam [Sar91]. The dynamic spring constants can be calculated from the static spring constants using the relations introduced by *Hähner*: $c_{L,1}^{dynamic}/c_L^{static} = 1.03$ or $c_{L,2}^{dynamic}/c_L^{static} = 40.2$ [Häh10].

With the spring constants given for both modes the force gradients can be calculated from the measured frequency shifts $\Delta f$ by equation (4.3). The precision of the introduced measurement technique for $\partial F_x/\partial x$ detection can be tested by comparing the measured force gradient with a simulated image. As mentioned, the force gradients of both modes can be calculated from each other. To do this in real space, the third component $dF_y/dy$ has to be known. However, as demonstrated in the first chapter (Section 1.2.3, equation (1.28)) the $z$-component of the stray field, and hence also the $z$-component of the force gradient, already contains all information about the other two components. In Fourier space the calculation of the in-plane force gradient $\partial F_x/\partial x$ from the out-of-plane force gradient $\partial F_z/\partial z$ is reduced to a simple multiplication operation. Utilizing equation (1.28) and the Nabla-operator in Fourier space defined as $\nabla = (ik_x, ik_y, -k)$ (see derivation in Section 1.2.3) the components of the Fourier transformed force gradients are connected via:

$$\frac{\partial \hat{F}_x}{\partial x} = -\frac{k_x^2}{k^2} \cdot \left(\frac{\partial \hat{F}_z}{\partial z}\right). \tag{4.6}$$

The inverse Fourier transformation gives the lateral force gradient $\partial F_x/\partial x$. With this the comparison of a complete measured second mode MFM image with a theoretically expected image is possible.

### 4.2.2 Comparison between calculated and measured in-plane contrast

A qualitative comparison between the first- ($z$) and second-($x$) mode MFM measurement can be found in Figure 4.7 (a) and (b). The first mode MFM image shows the well-

known domain contrast for the band-domain state of the Co/Pt reference sample (compare Section 3.5). The second mode contrast is pronounced for domain transitions along the $y$-direction (as indicated in Figure 4.7 a), which lies perpendicular to the Fe-CNT oscillation direction ($x$-direction). For domain transitions parallel (along $x$-direction) to the oscillation direction the contrast vanishes completely. This agrees with the expected signal for such a purely in plane-sensitive measurement.

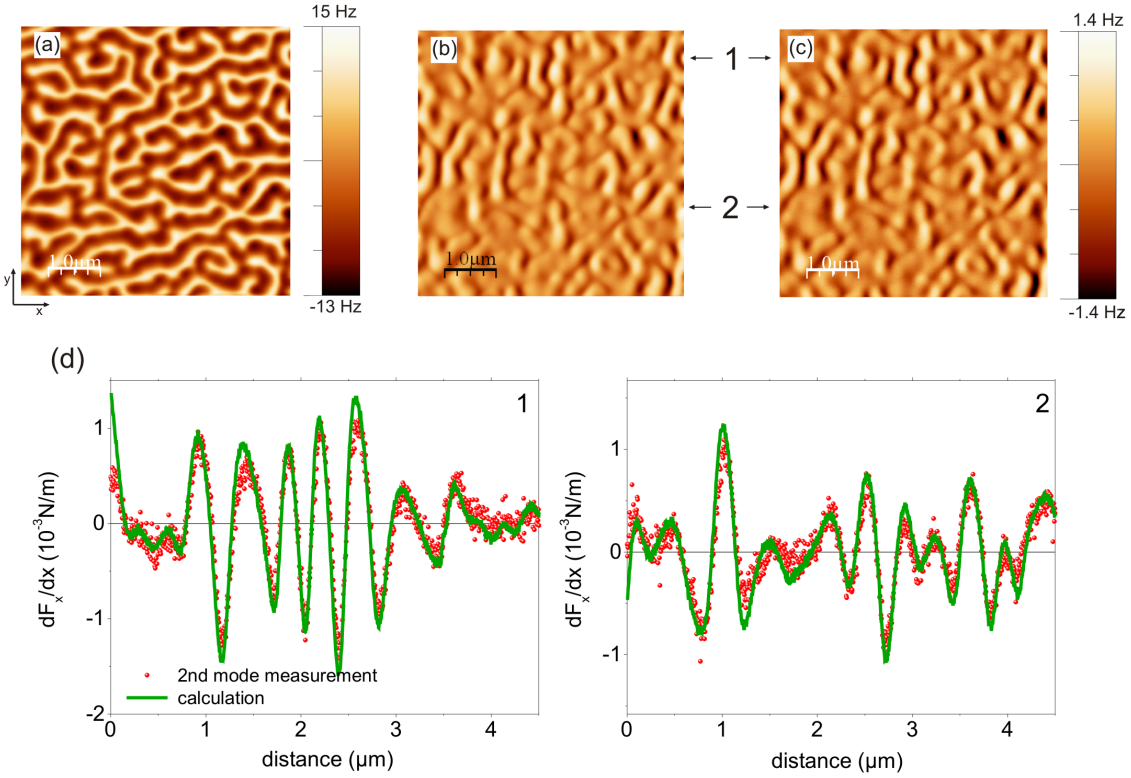


**Figure 4.7:** (a) Measured first mode image and corresponding image scale, (b) measured second mode image (measurements conducted by C. Reiche), (c) calculated second mode image, scale corresponding to (b) and (c), (d) diagrams with line sections through the images at the positions indicated by arrows and numbers in (b) and (c)

For quantitative conclusions the measured contrast is compared with the in plane-contrast calculated according to equation (4.6). The result is given in Figure 4.7 (c). The diagrams in Figure 4.7 (d) show two exemplary line sections through the MFM images, which reveal a very good agreement between in plane measurement and calculated signal. This again proves the monopole-like behavior of the Fe-CNT sensor. Furthermore, the accurate agreement between measurement and calculation proves the theory for the spring constant calculation to correctly relate the first mode and second mode spring constants.

The bimodal MFM technique can be applied to quantify the stray field components of an unknown sample. Therefore the additional knowledge of the Fe-CNT moment is necessary.

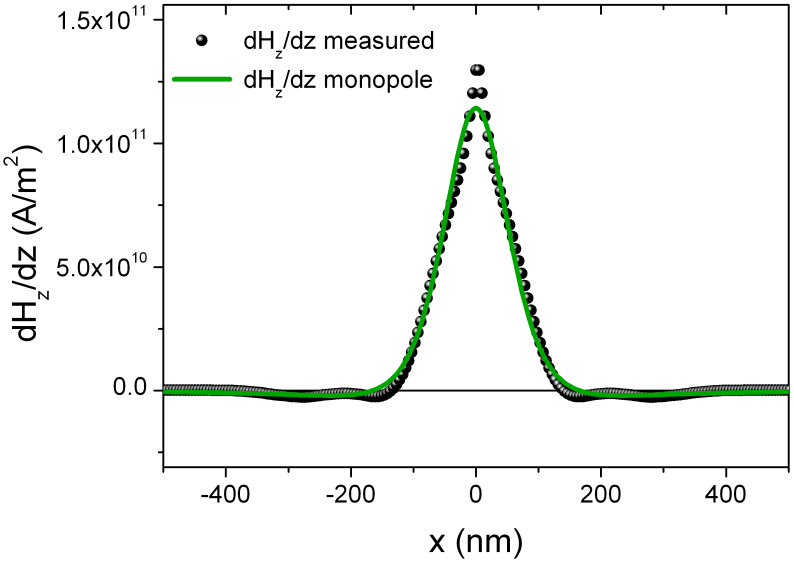


**Figure 4.8:** Stray field gradient of the Fe-CNT tip deduced from the calibration measurement (black circles) in Figure 4.7 (a) and fitted monopole stray field gradient (green solid line).

This can be derived from a calibration measurement as introduced in the previous section as well as by a calibration within the deconvolution approach as described in Section 3.2. The latter one is chosen here to directly determine the stray field gradient of the tip $dH_z/dz$ from the first mode MFM measurement as shown in Figure 4.7 (a). A line section through the maximum of the rotationally symmetric $dH_z/dz$ is plotted in Figure 4.8 (black circles). The result can be compared with the characteristics of a point monopole. The stray field gradient of a monopole is given by *de Lacheisserie et al.* [dL04]:

$$\frac{dH_z(x)}{dz} = \frac{q}{4\pi} \frac{x^2 - 2(z_{lift} + \delta)^2}{(x^2 + (z_{lift} + \delta)^2)^{5/2}} \tag{4.7}$$

where $\delta$ is again the displacement of the moment away from the Fe-CNT end and $z_{lift}$ the scan height in the MFM experiment. The function was fitted with $q$ and $\delta$ as free parameters to the measured $dH_z/dz(x)$. The qualitative comparison of the measured stray field gradient and the monopole fit (Figure 4.8) shows very good agreement. The resulting fit parameters are: $q = (1.2 \pm 0.25 \cdot 10^{-9})$ Am and $\delta = (37 \pm 0.5)$ nm.

Alternatively, the tip parameters can be directly deduced from the SEM image shown in Figure 6.9 (b). The measured diameter of the iron filling is $d_{Fe} = 32 \pm 5$ nm and the remaining carbon shell thickness is $t_c = 40 \pm 5$ nm. With the saturation magnetization of iron $M_s = 1.71 \cdot 10^6$ A/m the resulting monopole moment is given by $q_{geom} = M_s \pi d_{Fe}^2/4 = (1.4 \pm 0.4) \cdot 10^{-9}$ Am. Taking the relatively large error intervals into account, this corres-

ponds very well to the tip parameters obtained by calibration.

Summarizing, the above results additionally underline the conclusions of the previous section. Fe-CNT sensors show a magnetic behavior, which is very close to a real monopole tip. Furthermore, the relation between the calculated dynamic spring constants for the first and second mode is verified by the agreement between MFM measurement and theoretical signal calculation. This might be applied for a fast quantitative analysis of stray field gradients from MFM measurements in a real space approach. Having the deconvolution approach in Fourier space available, however, bears several additional advantages. The calibration has to be performed anyway and is much faster in the Fourier space approach. The quantification of sample stray field gradients or effective surface charges work with the true experimental ICF or RSICF without an additional fitting procedure. In contrast to this, Figure 4.8 reveals, that despite the good agreement between measurement and monopole model, there still exist small differences, which get lost after fitting. In the remaining chapters, the results are derived with the deconvolution approach offering the possibility to apply arbitrary tip types and greater ease of use.

# 5 Quantification of magnetic nanoobjects in MFM measurements

The direct deduction of the magnetic moment of nanoobjects and their size is one of the large challenges in MFM image analysis, which arises from the introduced (Section 3.1) convolution characteristic of the image formation. This chapter focuses on the analysis of the lateral dimensions of nanoobjects. This is done for two different physical problems: the quantification of the bubble domain size in a magnetic multilayer and the quantification of the magnetic penetration depth in a superconductor.

The first section analyses bubble domains, i.e. small cylindrical objects embedded in an inversely magnetized matrix, which are known to exist in magnetic multilayer films with perpendicular anisotropy. Here a $(Co/Pd)_{80}$ multilayer has been investigated in varying perpendicular field to assess the diameter evolution. Theoretical considerations predict a continuous enlargement of the bubble diameter with decreasing field [Bra09a]. This could be verified by the quantitative analysis of the experimental data [Voc11].

A second application concerns vortices in a superconducting iron-pnictide single crystal observed by MFM. Although, physically, bubble domains have little to do with vortices in superconductors, the determination of the correct vortex profile constitutes a very similar problem. For the stray field of a magnetic vortex in a type-II superconductor an exact analytical expression exists [Car00]. This qualifies vortices measured by MFM as suitable model objects to test the quality of the deconvolution procedure as introduced in Section 3.2. The method is compared to existing approaches based on a parameter-dependent model.

The content of this section was part of the diploma work of *F. Rhein* at IFW-Dresden conducted in the group of *Dr. V. Neu* [Rhe13]. The scientific ideas for the model comparisons were supplied by the author of this thesis, while the practical image evaluations were performed in close cooperation. The analysis was based on the deconvolution procedures developed in this thesis with additional software contributions from *F. Rhein* and *H. Stopfel* [Sto11, Rhe13]. The measurements presented in the last subsection (Subsection 5.2.2) were conducted by *F. Rhein* together with the group of *Prof. H.-J. Hug* at the University of Basel. The experimental measurement plan was elaborated in close cooperation with *F. Rhein, Dr. V. Neu, Prof. H.-J. Hug* and with helpful hints of *Prof. Auslaender*

from Technion (Haifa). The single crystal was provided by *Prof. Dr. D. Inosov* (address at that time: Max Planck Institute for Solid State Research, Stuttgart, present address: TU-Dresden, Department of Physics). The results of these investigations were included in this thesis, as they very unambiguously proof the power of a tip calibration and the deconvolution method as developed in this thesis.

## 5.1 Bubble domains in a $[Co/Pd]_{80}$ multilayer

Maze and bubble domain formation is well-known in films with strong perpendicular anisotropy ($Q > 1$) [Thi70, Rus01, Bra09a]. The maze domain pattern is formed in zero field. By applying an external field, the domains transform into isolated bubbles as schematically shown in Figure 5.1. The theory of *Thiele* [Thi70] and *Kooy and Enz* [Koo60] predicts, that the existence of these bubble domains, which are cylindrical domains of inverse magnetization, is restricted to a certain field region. Above the so-called collapse field $H_{bc}$ the bubbles disappear and the film is fully saturated [Thi70, Dav04]. If the external field is decreased below the strip-out field $H_{bs}$ the cylindrical shape of the bubbles is not stable anymore and transforms into isolated stripes. In between these critical fields, the diameter of the bubbles increases with decreasing fields (diagram in Figure 5.1 (c)).

The multilayer system studied has a $[Co(0.4\ nm)/Pd(0.7\ nm)]_{80}$ architecture[1]. The film exhibits strong perpendicular anisotropy with an anisotropy ratio of $Q = K_u/K_d = 1.7$. Global VSM hysteresis measurements reveal an almost zero remanence of the film (Figure 5.2, middle), which is verified by the MFM image[2] in zero magnetic field (Figure 5.2), bottom, left). After out-of-plane saturation in the zero-field state, the multilayer exhibits a random maze domain pattern with an average domain width of 155 nm. By increasing the external magnetic field, the domains, which are aligned parallel to the field, grow, while the oppositely aligned domains get smaller. This process occurs gradually until the domains transform into isolated stripes and, in the end, into a bubble domain structure at higher fields (compare the image series for the increasing branch in Figure 5.2). Reaching the critical field $H_{bc} \approx 450$ mT the collapse of the bubble can be directly observed during the MFM scan.

Decreasing the field again after saturation leads to the formation of new bubble domains. With further decrease the bubble shape and configuration stays stable but the

[1] The film is grown by magnetron sputtering on a 20 nm Pd buffer and is covered with 6 nm Pd. The sample was provided by *O. Hellwig*, HGST - Western Digital. Details for sample preparation are given by *Hellwig et al.* [Hel07].

[2] MFM images were recorded with the DI 3100 instrument under ambient conditions in the tapping/lift mode. The applied field and the magnetization of the tip are parallel in all presented MFM measurements.

MFM contrast arising from the bubble increases gradually down to the strip-out field (at 310 mT) [Bra09a]. This effect can be interpreted as a continuous enlargement of the bubble. The exact bubble size, however, can not be extracted directly from the MFM image, since it strongly depends on the magnetic properties of the tip.

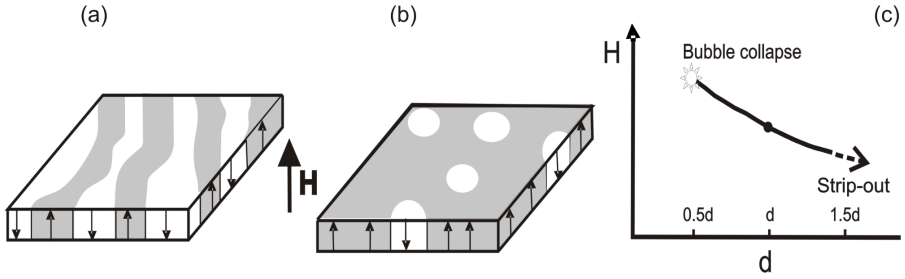


**Figure 5.1:** Schematic representation of (a) the maze or band domain state, (b) isolated bubbles and (c) the bubble diameter evolution in an external magnetic field (from [Bra09a]).

### 5.1.1 Micromagnetic model

For the theoretical description of bubbles in magnetic multilayers[3] with perpendicular anisotropy the theory by *Thiele* [Thi70] has been extended to include the surface charges of each individual magnetic layer in the multilayer architecture [Bra09a]. Following the procedure outlined in [Bra09a] the total energy of a cylindrical bubble in an external field is minimized with respect to the bubble diameter $d$. Additionally, the stability region of cylindrical bubbles with respect to strip-out and collapse is calculated. Input parameters for the calculations are the geometrical data of the multilayer, the measured saturation magnetization $M_S$ and the Bloch wall energy $\gamma = 4\sqrt{AK_u}$. The two latter quantities enter the equations in form of the critical length $l_c = \gamma/2K_d = \mu_o\gamma/J_S^2$. The result for the $[Co/Pd]_{80}$ multilayer (assuming a value $l_c = 4.1$ nm) is shown in Figure 5.5 as symbolized with the red triangles, predicting the bubble diameter as a function of the applied field. The stability range is indicated by the vertical red lines. Below the strip-out field calculations have been extended to possible unstable bubbles (dashed red line).

### 5.1.2 MFM image simulation

For the evaluation of the bubble diameters the following procedure was applied. The RSICF (real space instrument calibration function) can be determined from the zero field

[3]The micromagnetic model and calculations for the given material were derived by *N. S. Kiselev* and *A. N. Bogdanov*. Address at that time: IFW-Dresden, Institute of Theoretical Solid State Physics.

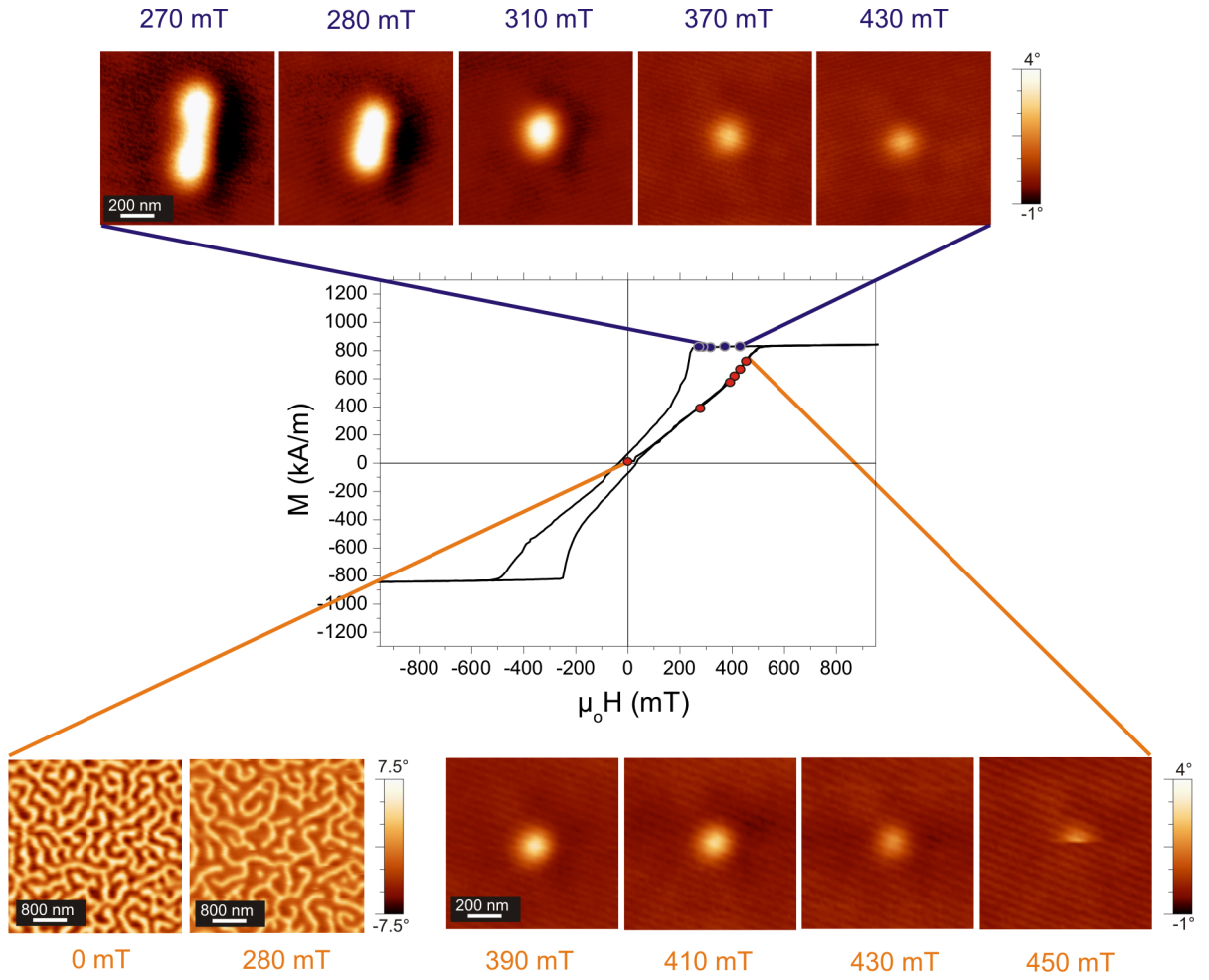


**Figure 5.2:** Hysteresis curve of the $[Co/Pd]_{80}$ multilayer measured by VSM. The MFM images on the bottom display the domain evolution on the increasing branch of the hysteresis curve. Starting with a maze domain pattern at 0 mT the oppositely magnetized bands (bright) shrink and transform into bubbles with increasing external field. The bubble diameters further shrink until they finally collapse at a field of 450 mT (image at the far right). The circles mark the fields at which the MFM images were taken. The images at 0 and 280 mT were recorded on a larger range than the following images at higher fields. The scale bars apply to the images on their left, respectively. The MFM images on the top display the process of bubble strip-out with decreasing external field. According to the first occurrence of deviation from circular symmetry the experimental $H_{bc}$ is determined as 310 mT.

MFM image. In this state the magnetization can be assumed to be almost perpendicular to the sample surface within the domains and the saturation magnetization is known from the global VSM measurement. With this the surface charge map can be deduced, the Bloch-type domain transition included and the RSICF calculated by applying the calibration procedure introduced in Section 3.2.

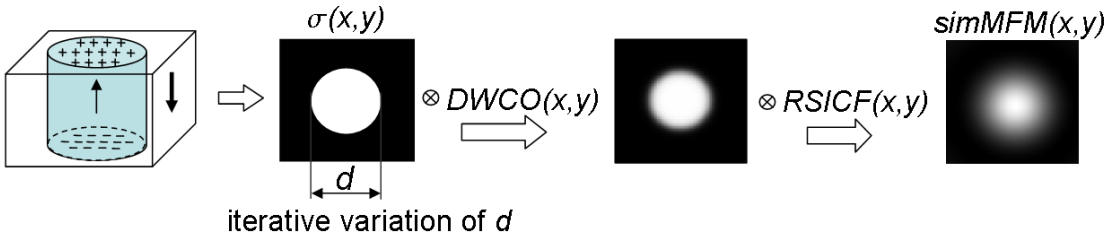


**Figure 5.3:** Schematic representation of the MFM image simulation of isolated bubbles with variable diameter $d$.

The present deconvolution problem has the advantage that additional information about the magnetic object is available. This is the cylindrical form of the bubble with a magnetization along the cylinder axis. As a first approximation it is reasonable to assume the transition between the matrix and the bubble domain to be of Bloch-type [Kis11], even though more complex transitions are known for bubble films [Hub98]. A surface charge distribution for a cylindrical bubble with a starting radius was created and convolved with equation (3.18) to introduce domain walls. The wall width was chosen to be $\delta_w = 23$ nm assuming an exchange constant A = 28 pJ/m according to [Bra09b]. This surface charge pattern is convolved with the RSICF$(x, y)$ and results in a simulated MFM image as schematically shown in Figure 5.3. The bubble diameter is iteratively varied until a minimum deviation from the measured MFM image is found. In Figure 5.4 (a) the comparison between simulated bubble images at 320 and 430 mT and the corresponding measured MFM images are shown. The line profiles through the center of the measured and simulated bubble image displayed in Figure 5.4 (a) at 320 mT are shown exemplary in the diagram in Figure 5.4 (b). The simulated MFM contrast fits the measured contrast very well, both in absolute value and shape. This proves the tip calibration procedure to be adequate and the assumption of a cylindrical bubble shape justified.

### 5.1.3 Results and discussion

The quantitative analysis of the bubble size was carried out for the MFM images recorded on the decreasing branch of the hysteresis loop. The results are summarized in Figure

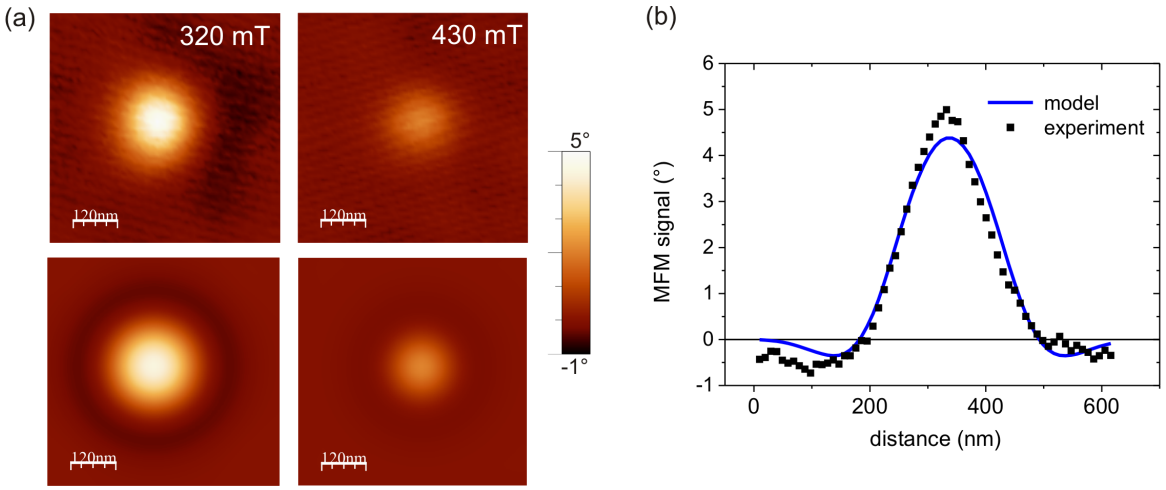


**Figure 5.4:** (a) Bubble domains measured in different fields (top) and the simulated MFM images for the same field values (bottom). (b) Comparison of a single line through the center of the bubble for a measured (black squares) and a simulated bubble (blue line) at 320 mT.

5.5. In agreement with the theoretical model the bubble diameter shrinks with increasing field in a nearly linear manner. Furthermore, the experimentally observed values for the bubble strip-out ($H_{bs}$ = 320 mT) and collapse field ($H_{bc}$ = 450 mT, vertical solid lines) compare well with the predicted values of $H_{bs}$ = 330 mT and $H_{bc}$ = 440 mT (vertical dashed lines). The measured and deconvolved values for the bubble diameters come close to theoretically predicted ones although there is a shift to higher diameters visible for the experimental data. Possible reasons for this discrepancy may lie in the experimental limits for the detection of such small domain sizes. First of all the MFM signal is measured in discrete steps of about 10 nm. This is the reason for the relatively large error bars of ± 20 nm in Figure 5.5. A second reason is the resolution limit, which arises from the combined influence of the tip, the cantilever (hr-MFM Team Nanotec), the MFM electronics and the properties of the measured sample.

A better understanding of the effect of limited tip resolution can be obtained by looking at the Fourier spectra of the ICF and the bubbles in Figure 5.6. There is a large interval, where the ICF amplitude is already decreasing significantly, but where the small bubble (see lower diagram in Figure 5.6) has still large Fourier components and thus the convolution with the ICF is connected to a loss of information. The ICF drops further until a wavelength of about 50 nm. This value can be seen as an estimation of the tip's lower resolution limit at a tip-to-sample distance of 50 nm, which is a reasonable lower limit and a value similar to those determined by *Abelmann et al.* [Abe98]. The subsequent increase of the ICF at higher frequencies is due to the increasing noise with increasing frequency. These experimentally limiting parameters (small object size and limited ICF frequencies) can lead to a deviation from the theoretically predicted values. However, the trend of bubble

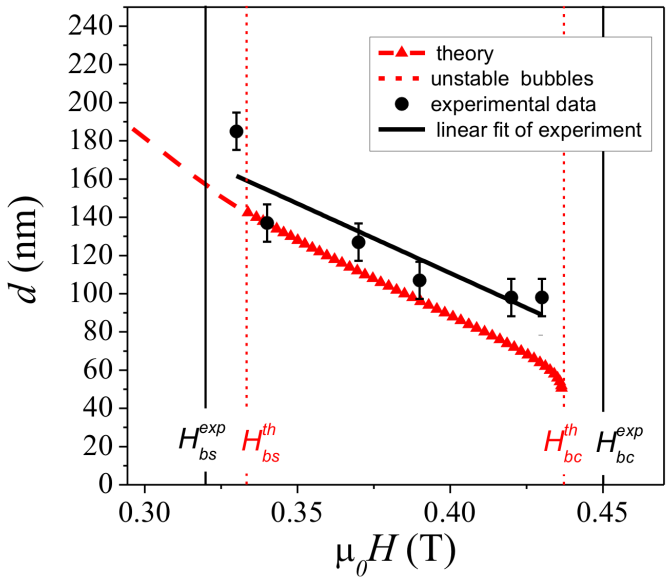


**Figure 5.5:** Dependence of the theoretical and experimental bubble diameter on the applied perpendicular magnetic field. $H_{bs}$ and $H_{bc}$ indicate the strip-out and collapse field for the micromagnetic model and the experimental data, respectively. The micromagnetic calculations were done by N. S. Kiselev.

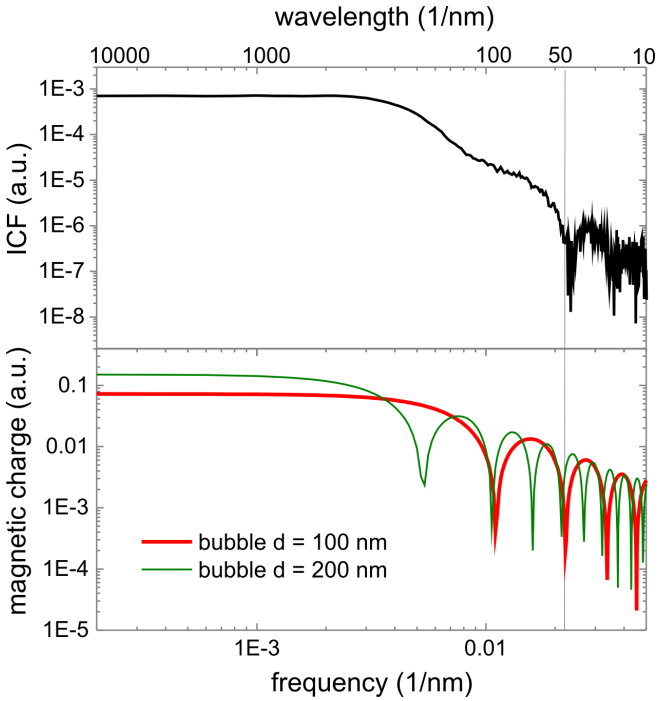


**Figure 5.6:** Power spectrum densities of the ICF (top) and bubble domains of different sizes (bottom).

evolution could be reproduced clearly and the absolute values are within the error interval of the measured bubble diameters.

In summary, the applicability of a deconvolution procedure for the quantitative determination of magnetic bubble domain sizes was shown. This has important implications for the investigation of other magnetic nanoobjects such as nanoparticles or vortices in superconductors.

## 5.2 Quantitative assessment of the magnetic penetration depth in superconductors

The magnetic penetration depth $\lambda$ is a fundamental property that characterizes a superconductor. It defines the distance to which a magnetic field penetrates into a superconductor. More specifically, it denotes the distance at which the magnetic flux of a flux line in a type II superconductor decays to 1/e of its value in the center (see Figure 5.7, for further details it is referred to *Buckel* [Buc08]).

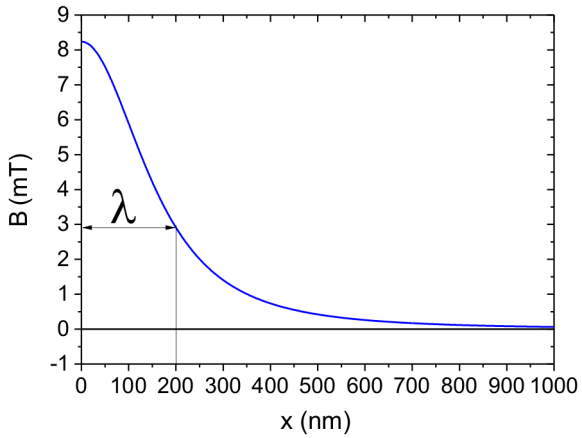


**Figure 5.7:** Spatial variation of the magnetic flux density. $\lambda$ is the distance, where the flux density droped to its 1/e part.

The use of MFM as local probe of $\lambda$ has been introduced recently [Ros01, Str08, Naz09, Lua10, Lua11, Sha11, Kim12]. With a low temperature MFM device (LT-MFM) the temperature dependence of $\lambda$ can be studied. One possibility for the quantification of $\lambda$ is the detection of the Meissner repulsion as a function of distance in a single point above the superconducting state [Lua10, Lua11, Kim12]. The resulting curve is fitted with a theoretically calculated function based on a tip model, which is described as a truncated cone. Another method fits the MFM profiles of vortices [Ros01, Naz09] or two-dimensional vortex images [Sha11] with a theoretically calculated MFM signal. The task is challenging, as both, the influence of the vortex and the a priori unknown tip properties have to be included. All simulation models reported in the references given above contain multiple fitting parameters, which introduce uncertainties in the resulting $\lambda$, additional to the experimental errors. Therefore, in the following the limits of approaches presently used are pointed out and a model free algorithm based on image deconvolution is suggested. Finally, the successful application of the procedure to experimentally measured MFM data of a $BaFe_2(As_{0.24}P_{0.76})_2$ single crystal will be given. As mentioned before, the focus is on testing a frequently applied model and comparing it to the deconvolution approach by

simulations as well as experiment. The equations necessary for that are given within the sections.

### 5.2.1 Comparison of methods

In the following the applicability of methods will be discussed which are based on the extraction of $\lambda$ by fitting the MFM signal of vortices. Such fitting requires an analytical description of both, the vortex and the tip influence.

The full expression of the z-component of the stray field distribution above a vortex in a superconductor is given by *Carneiro and Brandt* [Car00]:

$$H_z(r,z) = \frac{\phi_0}{2\pi\mu_0\lambda^2}\int_0^\infty \frac{J_0(\gamma r)\exp(-\gamma(|z|-d/2))}{k_\gamma[\coth k_\gamma d/2 + k_\gamma/\gamma]}d\gamma \tag{5.1}$$

where r is the lateral distance from the vortex center, $z$ is the distance above the vortex measured from the center of the volume, $k_\gamma = (\gamma^2 + 1/\lambda^2)^{1/2}$ , $d$ the film thickness and $J_0$ is an integral Bessel function of the first kind. It has been stated in the above publication, that for film thicknesses $d > 4\lambda$ at a distance $z > \lambda$ the stray field of the vortex is well approximated by a magnetic monopole of strength $2\phi_0$ ($\phi_0$ being the flux quantum) located at a depth of $1.27\lambda$ below the surface. Under the given preconditions equation (5.1) simplifies to the stray field of a monopole $H_z^m$:

$$H_z^m(r,z) = \frac{\phi_0}{2\pi\mu_0}\frac{z+1.27\lambda}{((r-r_0)^2+(z+1.27\lambda)^2)^{3/2}} \tag{5.2}$$

where $(r-r_0)$ denotes the lateral distance from the vortex center.

As introduced in Section 3.1.2 and discussed in the previous chapter an MFM tip can be described by a magnetic monopole $q_{tip}$, which is located in a distance $\delta$ from the apex of the sharp tip end. With the above equation for the vortex field, the interaction can be described by two monopoles with one representing the tip and the other the vortex. A schematic representation motivating this description is given in Figure 5.8 (a). The force gradient within this so-called **monopole-monopole-model** is given by:

$$\frac{dF_z}{dz}(r,z) = \mu_0 q_{tip}\frac{dH_z^m}{dz}(r,z). \tag{5.3}$$

Finally, the MFM signal in the frequency detection mode (compare equation (2.13)) reads:

$$\Delta f = -\frac{f_0}{2c}\,\frac{q_{\mathrm{tip}}\phi_0}{2\pi}\,\frac{(r-r_0)^2 - 2(z+1.27\lambda+\delta)^2}{((r-r_0)^2+(z+1.27\lambda+\delta)^2)^{5/2}} \tag{5.4}$$

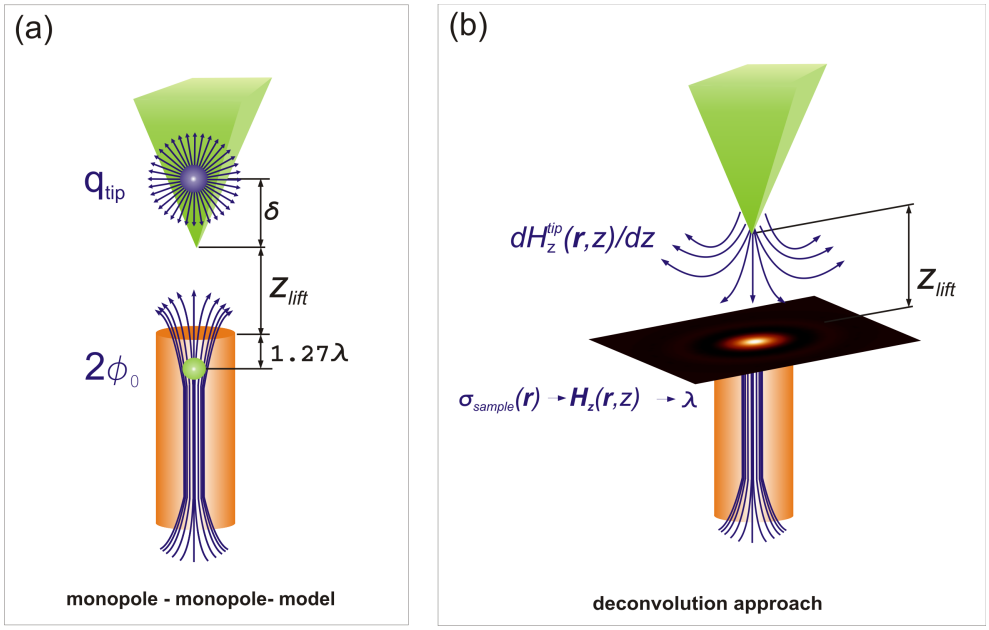


**Figure 5.8:** (a) Sketch of the monopole-monopole model. (b) Sketch of the deconvolution approach, describing the effect of the vortex in terms of equivalent magnetic surface charges.

where $r_0$ again denotes the center of the vortex and $r$ now denotes the lateral position of the tip. This model was applied by *Straver et al.* and *Shapoval et al.* to extract $\lambda$ values from MFM images by fitting vortex profiles [Str08, Sha11]. The images are fitted to a sum of $\Delta f$ terms, one for each vortex, plus $df_{\text{offset}}$ for the Meissner repulsion. The free parameters of the fit are $df_{\text{offset}}, \frac{f_0 q_{\text{tip}}}{2c}$ and $\delta + \lambda$. These parameters are all the same for the vortices in the image.

For the exact and parameter free formulation of the tip-vortex interaction, the full description of both the tip and vortex properties is necessary. According to equation 3.7 the frequency shift in Fourier space reads:

$$\Delta\hat{f}(\mathbf{k}, z) = -\frac{\mu_0 f_0}{2c}\sigma^*_{\text{sample}}(r)\frac{dH_z^{tip}}{dz}(\mathbf{k}, z). \tag{5.5}$$

Here $\sigma^*_{sample}$ can be understood as an effective surface charge distribution including both, the top and the bottom surface. $\sigma^*_{\text{sample}}$ produces a stray field of the form given by equation (5.1). This is not an approximation, but an equivalent description of the vortex in terms of magnetic charges (see Figure 5.8 (b)). The Fourier transform of the stray field produced by the vortex directly follows from equations (1.26) and (1.27):

$$\hat{H}_z(\mathbf{k}, z) = -\frac{1}{2}e^{-kz}\hat{\sigma}^*_{sample}(\mathbf{k}). \tag{5.6}$$

This full description of the tip sample system can be used to extract $\lambda$ from an MFM

image as follows. First, the effective surface charge distribution $\sigma^*_{sample}$ of the vortices is obtained by the **deconvolution approach** introduced in Section 3.2. Second, the stray field of the vortices is calculated by equation (5.6) and the inverse Fourier transformation. Finally, this stray field is fitted with the integral expression of equation (5.1) with $\lambda$ being the sole free parameter.

The applicability of both approaches, the monopole-monopole-model and the deconvolution method, can be tested by simulating MFM images with a given $\lambda_{orig}$. To do so, the reciprocity principle is applied (Subsection 1.2.2), which allows to simply interchange the indices (tip, sample) of $\hat{\sigma}$ and $d\hat{H}_z/dz$ in equation (5.5). The stray field gradient of the sample $dH_z^{\text{sample}}/dz(r,z)$ can be calculated numerically via equation (5.1). The tip property, which is now $\sigma^*_{\text{tip}}$, represents the tip-equivalent surface charge distribution on a plane right at the end of the tip apex, parallel to the sample [Mey04, Pil06]. Again, this formulation contains no approximations but is a full description of the tip's complex three dimensional magnetization structure.

In order to simulate a realistic MFM image $\sigma^*_{\text{tip}}$ is deduced from a calibration measurement, similar to that used for the experiments introduced in the next section. Thereafter, the image is calculated by multiplying the Fourier transforms of $\sigma^*_{\text{tip}}$ and $dH_z^{\text{sample}}/dz(r,z)$ and adding a Gaussian type noise with a standard deviation of 0.02 Hz. A schematic representation of the image simulation is given in Figure 5.9. MFM images for varying

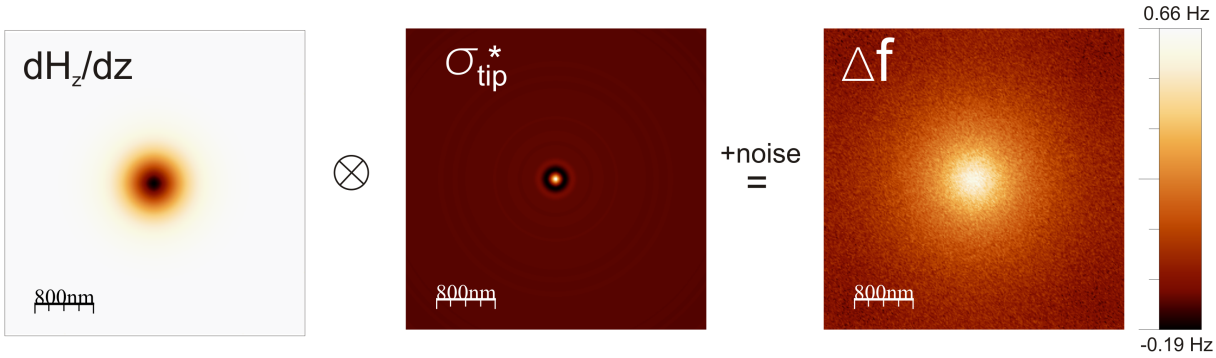


**Figure 5.9:** Visualization of the MFM image simulation. The stray field gradient of a vortex, calculated on the basis of equation (5.1), is convolved with the tip equivalent surface charge. With adding Gaussian type noise a realistic MFM image can be simulated.

sample thicknesses $d$ = 100, 500 and 2000 nm, varying tip lift heights $z_{\text{lift}}$ = 30, 200 and 400 nm and a constant $\lambda_{\text{orig}}$ = 200 nm are calculated. The evaluation methods are then tested for their accuracy, i.e. to how much the result of the $\lambda$-analysis ($\lambda_{re}$) reproduces the original value ($\lambda_{\text{orig}}$ = 200 nm). The $\lambda$ estimation within the monopole-monopole-model was performed in two ways. In one version, the a priori unknown tip parameter $q_{\text{tip}}$ was set as free parameter and $\delta = 0$, according to the procedure introduced by *Straver et al.*

and *Shapoval et al.* [Str08, Sha11]. The second version extracts the values for $q_{\mathrm{tip}}$ and $\delta$ from the calibration measurement[4]. With this $\lambda$ remains as the only fit parameter in the monopole-monopole-model.

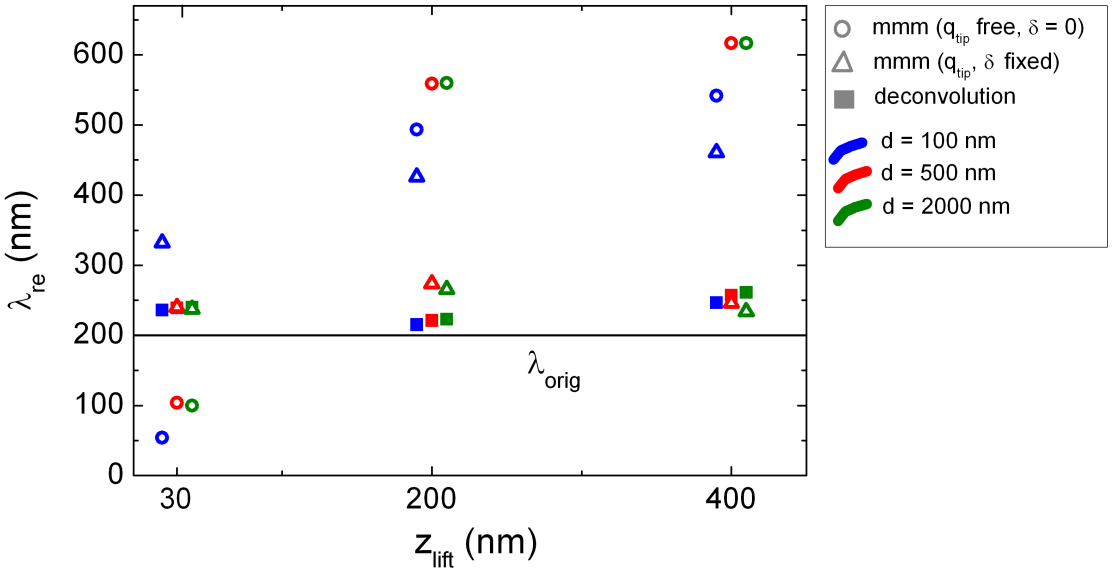


**Figure 5.10:** Accuracy of penetration depth recovery within each approach for varying sample thicknesses d and distance above the sample $z_{\mathrm{lift}}$. The approaches are distinguished by different shapes (triangle, square, circle) and varying sample thicknesses are marked with different colors. The original penetration depth was $\lambda_{\mathrm{orig}} = 200$ nm. (The $z_{\mathrm{lift}}$ values were shifted by 10 nm for better visibility.)

The comparison of the reproduced $\lambda_{re}$ values for each evaluation method (distinguished by the symbol form), for the different $d$-values (distinguished by the symbol color) and different $z_{\mathrm{lift}}$-values (the $x$-axis) is given in Figure 5.10. The original $\lambda_{\mathrm{orig}}$-value is pointed out by the black line parallel to the $x$-axis. The monopole-monopole-model with $q_{\mathrm{tip}}$ free and $\delta = 0$ nm turns out to be not applicable to estimate the original $\lambda_{\mathrm{orig}}$-value. Neither for close, nor for far distances above the sample surface and for none of the $d$-values $\lambda_{re}$ comes closer than 50 % to $\lambda_{\mathrm{orig}}$. The $\lambda_{re}$-values can be regarded as arbitrary fitting results, which arise from too many fitting parameters in the model. A correct analysis with this model may only occur by chance.

The situation clearly changes for the monopole-monopole-model with fixed tip parameters. For larger thicknesses ($d = 500$, 2000 nm) $\lambda_{\mathrm{orig}}$ can be reproduced for each given $z_{\mathrm{lift}}$ with an accuracy between 17 % and 37 %. Apparently, the tip is described decently well with the calibrated monopole model but the monopole model of the vortex fails. The thicknesses

[4]This was done by calculating the stray field of the tip with equation (1.27) and fitting the result with the stray field of a magnetic monopole with $q_{\mathrm{tip}}$ and $\delta$ being fit parameters.

were chosen such, that for $d$ =100 nm and $d$ = 500 nm the limiting condition $d > 4\ \lambda$ is violated. The same holds for $z_{\mathrm{lift}}$ = 30 nm, which does not obey the condition z > $\lambda$.

In contrast to this, the accuracy of the deconvolution approach obviously does neither depend systematically on the sample thickness, nor on the measurement distance. The $\lambda_{\mathrm{orig}}$-value can be reproduced within an accuracy of 8 % to 25 %. The remaining error is caused by the limited resolution of the tip[5].

Summarizing, the monopole-monopole-model only performs well, if the tip has been previously calibrated and with this the parameters can be fixed. The fact that a preceding calibration of the tip is indispensable for a quantitative assessment of magnetic object sizes is underlined with these results. However, even with a calibrated tip, the monopol-monopole-model is not applicable for thin samples with thicknesses smaller than or in the order of $\lambda$. The comparison of the evaluation methods reveals the strength of the deconvolution approach. In contrast to the monopole-monopole-model it is parameter-free and thus independent of sample thickness and measurement distance. Furthermore, it allows to fit two dimensional MFM data, going beyond vortex profile fits as reported by *Nazaretski et al.* and *Roseman et al.* [Naz09, Ros01] and single-point force-distance measurements as reported by *Luan et al.* and *Kim et al.* [Lua10, Kim12].

### 5.2.2 Experimental determination of the temperature dependent penetration depth in a $BaFe_2(As_{0.24}P_{0.76})_2$ single crystal

In the following, the deconvolution approach is applied to extract the temperature dependence of the magnetic penetration depth of a $BaFe_2(As_{0.24}P_{0.76})_2$ single crystal from measured MFM images.

The measurements were performed by *F. Rhein* at the low temperature MFM (LT-MFM) device at the University of Basel under the supervision of *Prof. H.-J. Hug* and the members of his group *Dr. N. Joshi* and *Dr. S. Özer*. The LT-MFM detects the frequency modulation of the cantilever, therefore the measured signal is given in units of Hz. The MFM images, given in Figure 5.11, were taken in varying temperatures $T$ between 6.8 and 27.6 K. For increasing temperatures (from $T$ = 18.6 K on) the pinning force of the vortices decreases under a critical value [Str08,Sha10a], at which the tip partially drags away the vortices. The vortex movement is visible as "cutted" objects in the MFM image. Details on the depinning mechanism of vortices in MFM experiments are given by *Shapoval et al.* [Sha11].

[5]The simulations were performed with a real RSTF, which was calibrated at a quite far distance $z_{\mathrm{lift}}$ = 200 nm. The accuracy of the RSTF can be further improved and with this also the resolution, when calibrating at a closer distance. This is subject of ongoing work and is presumed to result in an even more precise reproduction of the penetration depth.

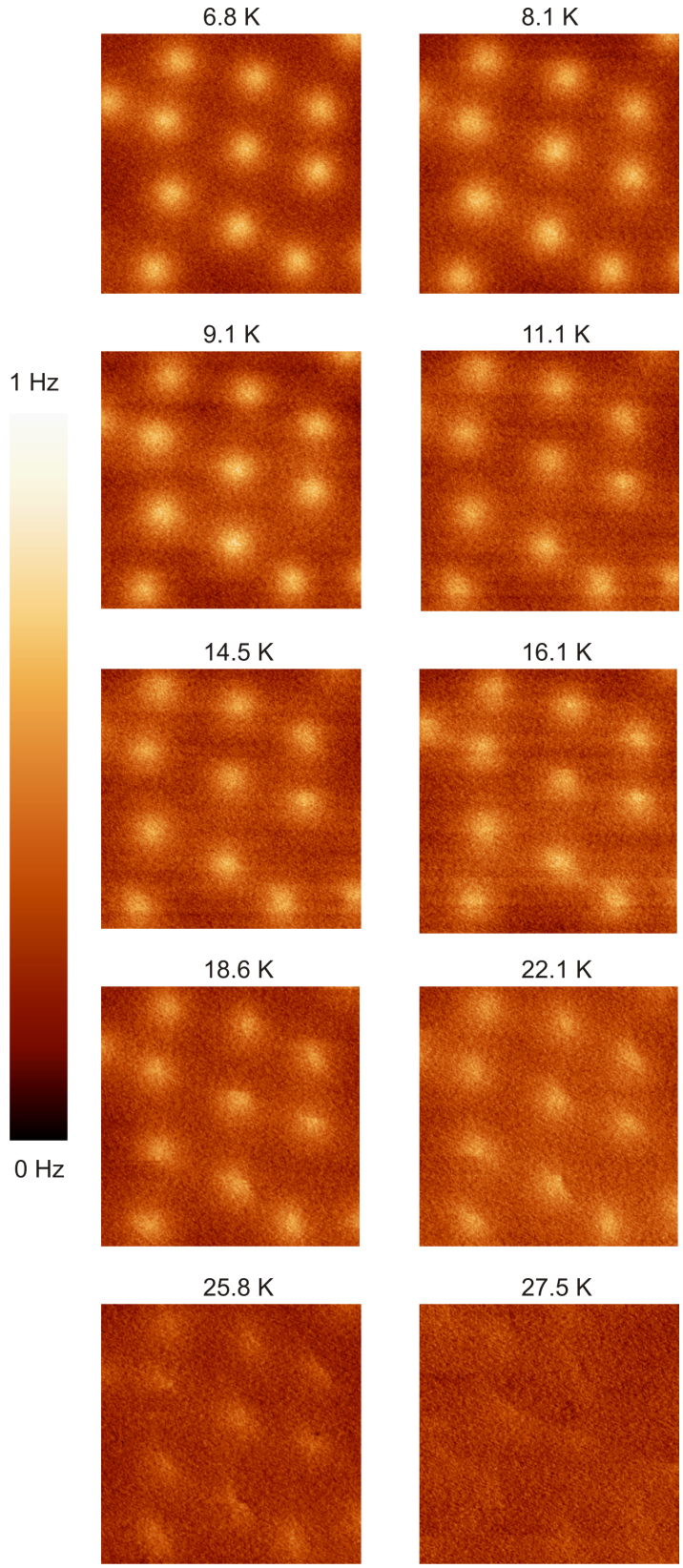


**Figure 5.11:** MFM images at varying temperatures from $T = 6.8$ K to 27.6 K. Scanning distance: 460 nm, scanning area: 4 µm x 4 µm

Prior to the quantitative evaluation a $df_{\text{offset}}$ was subtracted from the images, in order to account for the overall present Meissner repulsion. Finally, the temperature dependence of $\lambda$, as evaluated by the deconvolution approach, is given in Figure 5.12. The obtained values are fitted by the theoretical $\lambda(T)$ function according to [Buc08]:

$$\lambda(T) = \frac{\lambda(0)}{\sqrt{1 - (\frac{T}{T_c})^n}} \tag{5.7}$$

where $\lambda(0)$ and $n$ are material dependent characteristic values and $T_c$ denotes the critical temperature.

The fitting yields an $n$ value of 3.98 and a $\lambda(0)$ of 247 $\pm$ 60 nm. The error value is an upper estimate according to the largest error obtained in the previous section for the deconvolution approach. The determined $n$ value comes close to that of conventional superconductors with an s-wave gap, where $n = 4.0$ [Buc08]. The obtained $\lambda(0)$ value is, within the error interval, consistent with values reported by [Has10] ($\lambda(0) = 200 \pm 30$ nm) and therein cited reference [20] ($\lambda(0) \approx 170$ nm).

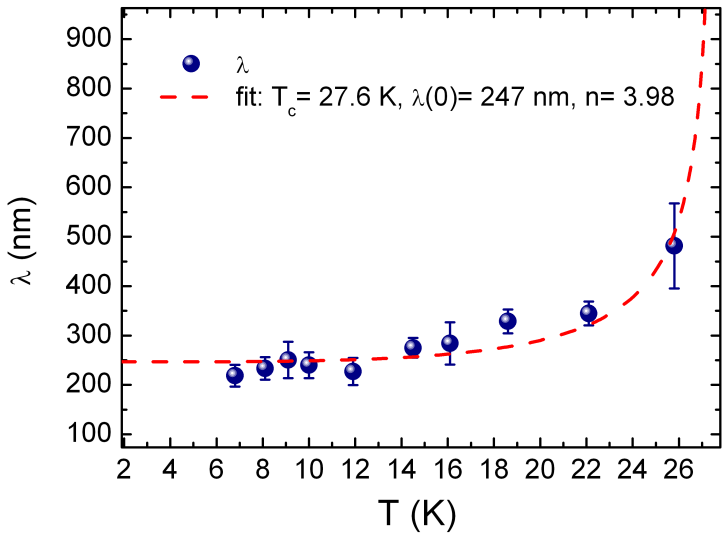


**Figure 5.12:** Temperature dependence of $\lambda$ as obtained from the MFM images given in Figure 5.11 (blue dots). Fitting the experimental results with the theoretical temperature dependence given by equation (5.7) yields the red line with the fit parameters n = 3.98 and $\lambda(0) = 247$ nm. The error bars represent the standard deviation of the $\lambda$ values obtained within one image.

Concluding, the proposed deconvolution method in combination with the full expression for the vortex stray field (equation (5.1)) enables the direct assessment of the magnetic penetration depth in superconductors. In particular, it is the method of choice for

investigations of superconducting thin films with thicknesses d $< 4\lambda$, where the monopole-monopole-model looses its validity.

# 6 Magnetization studies of CoFe nanowire arrays on a local and global scale

Beside the broad application areas [Sch10a], magnetic nanowire arrays are very suitable systems for studying fundamental magnetostatic properties. More precisely, nanowire arrays enable investigating the effect of dipole interaction fields on the magnetization behavior of an individual magnetic particle embedded in an array. Various kinds of nanowire arrays have been extensively studied over the last two decades (see e.g. [Sel01, Sko03, Sun05, Kum06, Sch10a, Hel13] and references therein).

Nevertheless, information about the magnetic status and magnetic reversal mode of a single wire as part of an array is still difficult to obtain, both theoretically as well as experimentally [Viv12, Váz11]. A basic problem is the difficulty to determine the exact stray field characteristics exerted by the surrounding magnetic objects. Furthermore, the effect of this field on the individual particle behavior has to be investigated. Since micromagnetic simulations on complete nanowire arrays exceed standard computational power, numerical calculations are mainly performed on single [Her04] or at most on a few (16) nanowires [Her02].

The first section of this chapter addresses this problem of stray field calculations in a nanowire array. Of interest are both, the short range stray field generated by the close environment of a central wire and the long range field generated by an infinitely large array. To that end, a position dependent expression for the array's stray field along the nanowire axis is derived. The herewith obtained distribution is implemented in a micromagnetic calculation in order to answer the question, what effect the sum of stray fields of surrounding wires has on an individual wire. Finally, the conclusions of these findings enable the calculation of theoretical hysteresis loops and the comparison with globally measured VSM data of $Co_{48}Fe_{52}$ arrays with varying length.

For the experimental part of the nanowire array characterization, MFM again proves to be a very useful tool. The local magnetization structure of individual wires within the array is studied with high resolution. In combination with the calibration procedure introduced in Section 3.2 it is possible to verify the existence of a magnetic vortex at the wire ends. This becomes possible with an approach that extends the two dimensional quantitative MFM approach into the third dimension, making use of the depth sensitivity of MFM.

The focus of the last section is on the short range magnetostatic interactions. These are described by a statistical analysis of the present nearest neighbor configurations of in field MFM measurements.

## 6.1 Revisiting the estimation of demagnetizing fields in magnetic nanowire arrays

### 6.1.1 Available approaches

Relevant for the deduction of intrinsic magnetic properties of the nanowire material within an array is the internal field present in each nanowire. The internal field $\mathbf{H}_{int}$ is the superposition of the externally applied field $\mathbf{H}_{ext}$ and the demagnetizing field $\mathbf{H}_d$. The demagnetizing field, similar to the stray field of a ferromagnetic body (compare equation 1.10) has its source in the particular shape of the magnetic volume. Discontinuities of the magnetization are related to volume and surface charges, which produce a stray field outside and a demagnetizing field inside the sample. The demagnetizing field is oriented anti-parallel to the magnetization and except for ellipsoids $H_d$ is nonuniform. However, also for non-ellipsoidal shapes a demagnetizing factor $N$ can be defined such that the internal field takes the form [Aha96]

$$\mathbf{H}_{int} = \mathbf{H}_{ext} - N\mathbf{M}. \tag{6.1}$$

For non-ellipsoidal bodies this description is only an approximation and gives an average of the internal field. Depending on how this average is calculated $N$ is named either *magnetometric* or *ballistic* demagnetizing factor. The magnetometric $N$ is calculated by averaging over the whole volume of the sample, whereas the ballistic $N$ is obtained by averaging over the middle cross-section of the volume perpendicular to the direction of the applied field [Aha96]. In the present considerations the magnetometric definition of $N$ is applied.

The calculation of $\mathbf{H}_d$ in an array of nanoparticles requires further considerations. Following the analysis by *Kronmüller* [Kro87] the demagnetizing field can be decomposed into the contribution of the self-demagnetizing field of the nanowire and the demagnetizing field of the macroscopic thin film, that is the whole array of nanowires.

$$\mathbf{H}_{macro} = -N_{macro}\mathbf{M}, \quad \mathbf{H}_{wire} = -N_{wire}\mathbf{M}. \tag{6.2}$$

Perpendicular to the plane of the extended array, which is the direction under consideration throughout this section, the value of $N_{macro}$ is that of a thin film: $N_{macro} = 1$. The average

demagnetizing factor of an isolated nanowire with an aspect ratio larger 10 and parallel to the wire axis approximately gives: $N_{wire} = 0$. The total $\mathbf{H}_d$ of the array has to be composed of these two contributions. This has been addressed for different particle arrays by several authors over the last two decades. An overview of the different attempts is given in the following.

If the *Kronmüller* approach is applied to arrays with grains in contact, then the total demagnetizing field is the sum of the two contributions given above. This has been successfully applied to describe the demagnetizing effects in granular hard magnetic media by *Dobrynin et al.* [Dob09, Dob10]. If the nanoparticles are embedded in a nonmagnetic matrix not mediating magnetic exchange, the demagnetizing field scales with the amount of magnetic material in the volume. If the interactions are weak and the particles switch independently of each other, an effective $H_d$ can be calculated, which averages the demagnetizing effect over the whole volume. The approach, first introduced by *Netzelmann*, combines the limiting case of an isolated particle with that of a homogeneously magnetized macroscopic body [Net90]. If $p$ is the volumetric packing fraction of the magnetic particles in the macroscopic body, the first limit is obtained for $p \to 0$, the second for $p = 1$. Assuming a transition between the limiting cases, which is linear in $p$, the demagnetizing field can be written [Net90]:

$$H_d = (1 - p)MN_{wire} + pMN_{macro}. \tag{6.3}$$

A similar approach proposed by *Skomski* and *Sellmyer* defines an effective demagnetizing factor for the special case of triangularly arranged nanowires in an array [Zen00, Sko01]

$$N_{eff} = p = \frac{\pi(D/d)^2}{2\sqrt{3}} \tag{6.4}$$

where $D$ denotes the wire diameter and $d$ the center-to-center distance. Here it is assumed, that the wires are sufficiently long and therefore $N_{wire}$=0. *Skomski* and *Sellmyer* show, that this approach can describe experimental data very well as long as the criterion of uncorrelated switching processes is full-filled. The particular geometry of the cross-section of the wire and the local magnetization structure at the end of the nanowire is not included within this description. It is assumed, that these local effects are negligible in the long range of the array and only sum up to a homogeneous contribution, that is to the demagnetizing field $H_d$.

A conceptually different approach is the calculation of $H_d$ by summing over the stray field contributions of all particles. To this end several authors approximate the particles by dipoles. *Grimsditch et al.* calculate the dipolar field of a planar array of dots (all magnetized in the same direction) on a square lattice by a dipole sum [Gri98] in order to extract

in-plane anisotropies. The point dipole approximation is justified in this case, because the separation of the dots is much larger than their height and their lateral dimension (distance between dots = 400 nm, diameter ≈ 100 nm). The same formula is applied by several authors for the calculation of the dipolar field of nanowire arrays [Str99,Riv02,Gha11,Das12]. The calculation of the preferred magnetization orientation either parallel or perpendicular to the wire axis can be roughly estimated qualitatively with this approximation. However, for high aspect ratio wires on grids with wire-to-wire distances smaller than the wire length, the dipole approximation no longer holds and leads to an overestimation of the field by almost two orders of magnitude.

*Raposo et al.* and *Clime et al.* model the single nanowire as a chain of dipoles [Rap00, Cli06]. This circumvents the large overestimation of the field in short distances, but still leads to deviations from experimental results in the range of 20-50 %. Another approach is offered by *Ishii* and *Sato*, who describe a single high aspect ratio iron column as a magnetic dipole with a certain length and poles at its ends, which are in the units of an area moment [Ish89]. This allows to include the nanowire length in the field calculation. The dipoles are located on a triangular grid extending to infinity. The overall stray field is calculated by summing over all dipole contributions. The summation is approximated by an integration for the area outside a certain radius and carried out numerically for the inner radius. With this the authors could successfully describe the shearing of experimental hysteresis loops of a magnetic iron film with columnar structure from a previous publication by *Masuda et al.* [Mas87]. The approach was later on adapted to calculate the internal field correction in nanowire arrays with triangular lattice by *Samwel et al.* and corrected by a small (1.1) scaling factor [Sam92]. The resulting equation was applied for hysteresis loop calculations of nanowire arrays consisting of $255^2$ wires by *Nielsch* and *Stadler* [Nie07] and for explaining the strength of interaction fields measured by first order reversal curves by *Dobrota* and *Stancu* [Dob13].

*Beleggia et al.* derived general expressions for the magnetostatic energy of magnetized nanoparticles with arbitrary shape in the framework of a Fourier space approach [Bel04]. The authors compare the so-derived full expression for the energy of two interacting nanowires with a pure dipole-dipole interaction and with a model including the poles at the wire surfaces as magnetic charges (monopole description). The comparison reveals that the dipole expression holds for magnetic disks as used by *Grimsditch et al.*, but diverges to arbitrary large errors when the aspect ratio increases. In contrast to this, the monopole description agrees well (with a maximum error of approximately 4 %) with the full expression for two interacting nanowires, producing an error of approximately 20 % only for small aspect ratios below 10 (for center-to-center distances of $d = 4r$, with $r$ being the radius of the wire).

Due to the described shortcomings of the dipolar approaches mentioned above, a monopole approach for the calculation of $H_d$ of the whole nanowire array is derived in the following subsection. The results are compared with a pure dipole approach and the models of *Samwel et al.* [Sam92] and *Clime et al.* [Cli06].

### 6.1.2 Calculation of demagnetizing fields in nanowire arrays

#### Dipole and monopole sums

The stray field of a magnetic dipole with the vector magnetic moment $\mathbf{m}$ in a distance $(\mathbf{r}-\mathbf{r}')$ is given by [dL04]

$$\mathbf{H}(\mathbf{r}) = \frac{1}{4\pi}\left[3\frac{(\mathbf{m}\cdot(\mathbf{r}-\mathbf{r}'))(\mathbf{r}-\mathbf{r}')}{|\mathbf{r}-\mathbf{r}'|^5} - \frac{\mathbf{m}}{|\mathbf{r}-\mathbf{r}'|^3}\right]. \tag{6.5}$$

Equivalently, the stray field of a monopole with the charge $q$ in a distance $(\mathbf{r}-\mathbf{r}')$ is given by [dL04]

$$\mathbf{H}(\mathbf{r}) = \frac{q}{4\pi}\frac{(\mathbf{r}-\mathbf{r}')}{|\mathbf{r}-\mathbf{r}'|^3}. \tag{6.6}$$

The description of an array of nanowires on the basis of the above stray field equations is sketched in Figure 6.1. The quantity to be evaluated is the sum of the $z$ component

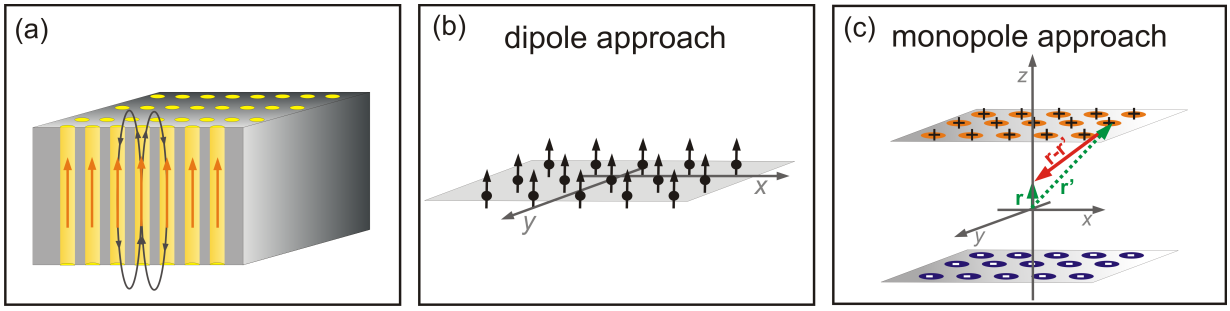


**Figure 6.1:** (a) Sketch of a nanowire array with all wires magnetized parallel. Description of the stray field contributions of the array by means of dipoles (b) and monopoles at the nanowire ends (c).

of the stray field contributions of all wires, denoted as $H_d$ in the following, in the case that each wire is magnetized in the same direction. The dipole approach (Figure 6.1 (b)) approximates the wires as point dipoles located in a plane. The extension of the nanowire in the $z$-direction is neglected in this approach.

Contrary to this, the monopole approach considers also the third dimension by placing the magnetic monopoles at the nanowire ends (Figure 6.1 (c)). This is similar to the stray field

calculation of a ferromagnetic body by means of its surface charges as introduced in the first Chapter (Section 1.2). The only approximation here is that the charges are assumed to be located in one single point, that is the middle of the circular cross section of the wire. This circumvents the need of an integration over the nanowire cross section. The error is expected to be insignificant in distances larger than the diameter of the wire and for an almost parallel wire magnetization. To check the validity of this assumption, the $z$ component of the demagnetizing field within and the stray field outside a single nanowire is calculated by equation (6.6) and compared to calculated fields on the basis of an extended volume[1]. Here, the numerical stray field result is regarded as almost exact, since it takes the three dimensional extension of the wire into account. Errors are only of numerical nature, but are negligible for large enough discretization. The comparison for a CoFe nanowire of 1 µm length, a diameter $D = 70$ nm and a saturation magnetization of $M_s = 1900$ kA/m is shown in Figure 6.2. The demagnetizing field (Figure 6.2 (a)) within the wire is calculated in the center of the wire and parallel to its axis (in the $z$ direction according to the definition of the coordinate system in Figure 6.1 (c)). As expected, the approximation agrees very well in distances larger than 70 nm away from the wire ends (indicated by the vertical black lines in the diagrams). The difference of the $H_z$ values in the middle of the wire ($z = 0$) is only 0.5 % ($H_z = -5.88$ mT for the micromagnetic calculation and $H_z = -5.85$ mT for the monopole approach). Coming closer to the wire ends the result of equation (6.6) diverges. This problem occurs only within the wire, while for positions outside the wire $(\mathbf{r} - \mathbf{r}')$ is nowhere zero. The stray field $H_z$ outside the nanowire in a distance of 100 nm, which is the position of an imaginary second wire, calculated from the monopole approach yields an even better agreement with the micromagnetic calculation. That is, already in a distance of the closest neighbor the monopole approach shows sufficient accuracy. It justifies neglecting the surface integration and it can be presumed, that the error for the stray field calculation of wires further away will play no role at all.

To calculate the sum of the stray field contributions, it is necessary to define the distances in the triangular wire arrangement. A sketch of the lattice is given in Figure 6.3 (a). In the monopole approach also the third dimension has to be taken into account as given in Figure 6.3 (b). Therefore, also the length $L$ is discretized into multiples of $d$. The base

[1] The field was calculated using the software OOMMF [Don99], which will be introduced in Section 6.2. The stray field was taken from the fully magnetized, i.e. non-relaxed state, of the simulation, in which the magnetization points perfectly along the wire axis. It is clear, that this does not represent the real magnetization structure of the wire, but here the aim is to compare a numerically calculated field without approximations concerning the given volume to an analytical model based on a monopole approximation.

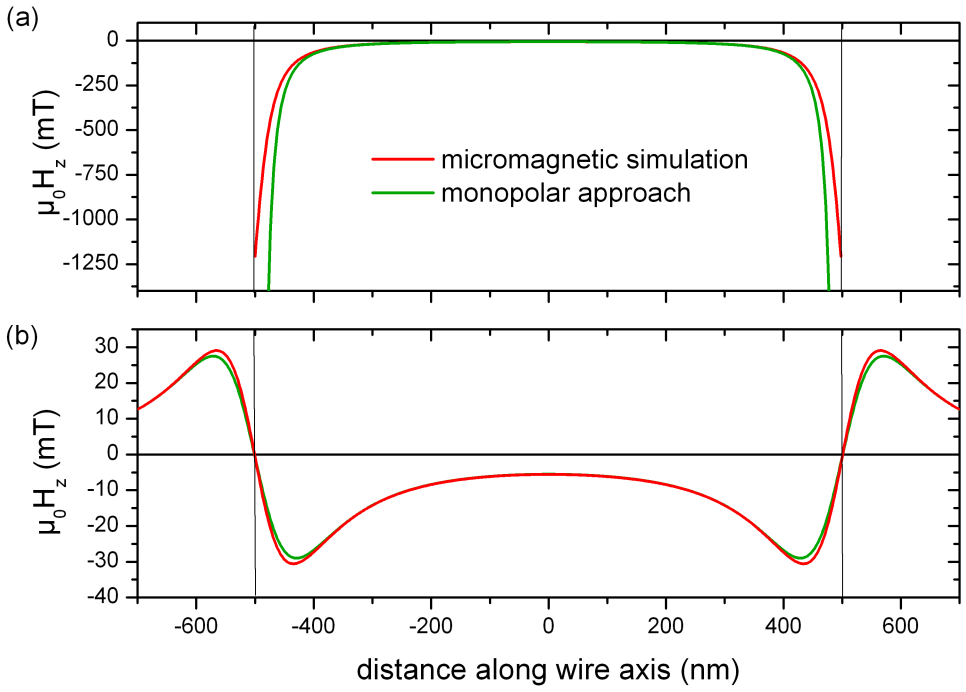


**Figure 6.2:** $H_z$ calculation according to equation (6.6) for a CoFe wire with $L = 1$ µm, $D = 70$ nm and $M_s = 1900$ kA/m. The micromagnetic simulation (red) includes the exact shape into the field calculation, while the analytical monopole approach (green) localizes the magnetic charges of the wire ends in the center of the wire cross section. $H_z$ is given as a function of position parallel to the wire axis for both calculation methods (a) along the center of the wire and (b) outside the wire in a distance $d = 100$ nm at the center of an imaginary second wire. The ends of the nanowire are indicated by vertical black lines at $-500$ and $+500$ nm.

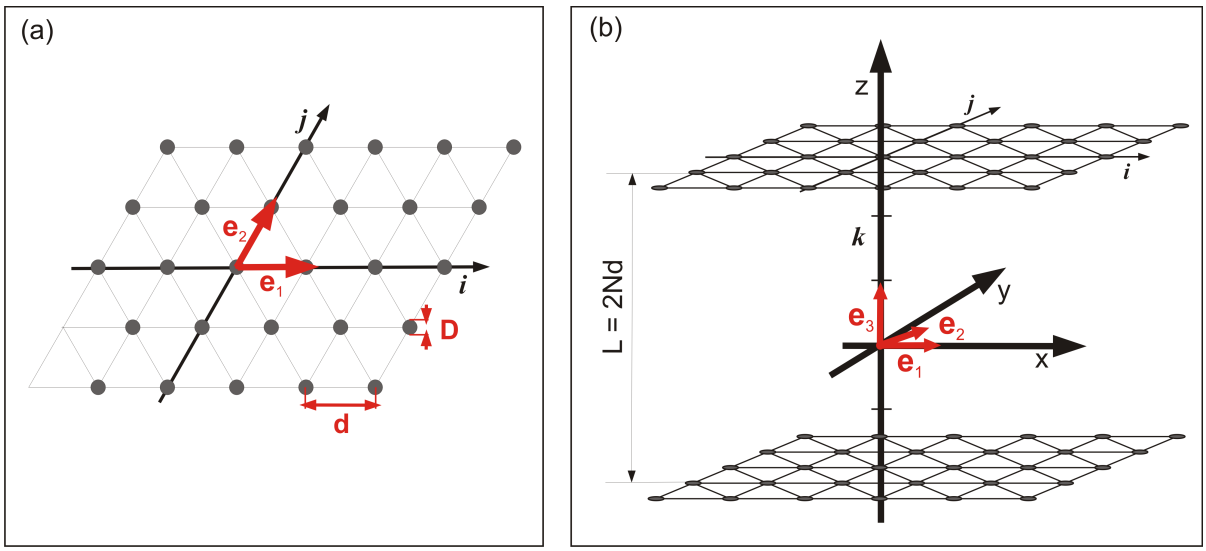


**Figure 6.3:** Definition of the lattice in a triangular nanowire arrangement. (a) Sketch of the top view of the lattice. $\mathbf{e}_1$ and $\mathbf{e}_2$ are the planar base vectors. The indices $i$ and $j$ denote the position within the array. (b) Three dimensional view of the nanowire array, which has been split up in top and bottom side charges. The third dimension is defined parallel to the wire axis and has also been discretized. The index $k$ denotes the position along the wire length. At the top side $k = +N$, at the bottom side $k = -N$and in the middle of the wire $k = 0$.

vectors of the array can be defined as

$$\mathbf{e}_1 = d \begin{pmatrix} 1 \\ 0 \\ 0 \end{pmatrix}, \mathbf{e}_2 = \frac{d}{2} \begin{pmatrix} 1 \\ \sqrt{3} \\ 0 \end{pmatrix}, \mathbf{e}_3 = d \begin{pmatrix} 0 \\ 0 \\ 1 \end{pmatrix}. \tag{6.7}$$

The vector $\mathbf{r}'$, which addresses the positions of the monopoles in the nanowire array (Figure 6.1 (c)), can thus be written as

$$\mathbf{r}' = i\mathbf{e}_1 + j\mathbf{e}_2 + k\mathbf{e}_3 \tag{6.8}$$

with $i, j$ and $k$ being integers. For a certain position $\mathbf{r} = (0, 0, kd)$ along the length of the center wire the distances to the top side and bottom side charges $(\mathbf{r} - \mathbf{r}'_1)$ and $(\mathbf{r} - \mathbf{r}'_2)$ are given by

$$(\mathbf{r} - \mathbf{r}'_2)^2 = d^2(i^2 + ij + j^2 + (k - N)^2) \tag{6.9}$$

and

$$(\mathbf{r} - \mathbf{r}'_1)^2 = d^2(i^2 + ij + j^2 + (k + N)^2) \tag{6.10}$$

where $i$ and $j$ go from $-\infty$ to $+\infty$ and $k$ moves along the wire axis from $-N$ to $+N$. With

the definition of the distances the sum of the monopole contributions $H_d$ along the axis of the center wire can be written as

$$H_d(0,0,kd) = -\frac{q}{4\pi}\frac{1}{d^2}\sum_{j=-\infty}^{+\infty}\sum_{\substack{i=-\infty \\ i=j\neq 0}}^{+\infty}\left(\frac{(k-N)}{(i^2+ij+j^2+(N-k)^2)^{\frac{3}{2}}} - \frac{(k+N)}{(i^2+ij+j^2+(N+k)^2)^{\frac{3}{2}}}\right) \tag{6.11}$$

where $q$ is the strength of the monopole and is calculated by: $q = M_s\pi D^2/4$. There exists no simple closed expression for this sum [Sas13a]. Thus, the above equation is evaluated numerically by setting the lower and upper limits $i, j = -M$ and $i, j = +M$, respectively.

As a first step the convergence is evaluated for varying a nanowire length in an array with $d = 100$ nm. The result is shown in Figure 6.4 (a). The longer the wire, the later convergence is reached. However, for the lengths under consideration here ($L \leq 25$ µ), it is sufficient to set $M = 8000$, which corresponds to approximately $16000^2$ wires and an area of approximately 2 mm$^2$. In Figure 6.4 (b) the development of $H_d$ along the axis of the center wire for an increasing number of surrounding wires is illustrated. The field is calculated here for an array with $L = 6$ µm, $D = 70$ nm and $d = 100$ nm. For small $M$ the stray field characteristic is similarly inhomogeneous as for a single wire (compare Figure 6.2). With an increasing number of wires, the field is increasing and develops a more and more homogeneous plateau in the middle of the wire. For a sufficiently large $M$ ($= 10000$) $H_d$ becomes almost homogeneous along the wire axis. The diagram further reveals, that the influence of the close environment of the center wire contributes only very little to the overall field (Figure 6.4 (c) and (d)). $M = 1$ corresponds to 8 surrounding wires. Relating this field to the field produced for $M = 10000$ (approximately $10^8$ wires) gives a factor of 0.17 at the peak positions and a factor of 0.001 in the center of the wire.

For comparison additionally the sum over dipole stray field contributions is given in the following. The planar distances can be calculated by equation (6.9) and setting $k = 0$ and $N = 0$. The wires are all magnetized parallel to the wire axis so that $\mathbf{m}$ in equation (6.5) can be set to $m_z$ and again only the $z$ component of the stray field is considered. The dipole sum reads

$$H_d(0,0,0) = -\frac{1}{4\pi}\frac{m_z}{d^3}\sum_{j=-\infty}^{+\infty}\sum_{\substack{i=-\infty \\ i=j\neq 0}}^{+\infty}(i^2+ij+j^2)^{-\frac{3}{2}} \tag{6.12}$$

with $m_z = \pi D^2 L M_s/4$. In contrast to the monopole sum, a closed analytical expression exists and has been derived for example by *Hucht* and by *Lambin et al.* [Lam93, Huc99].

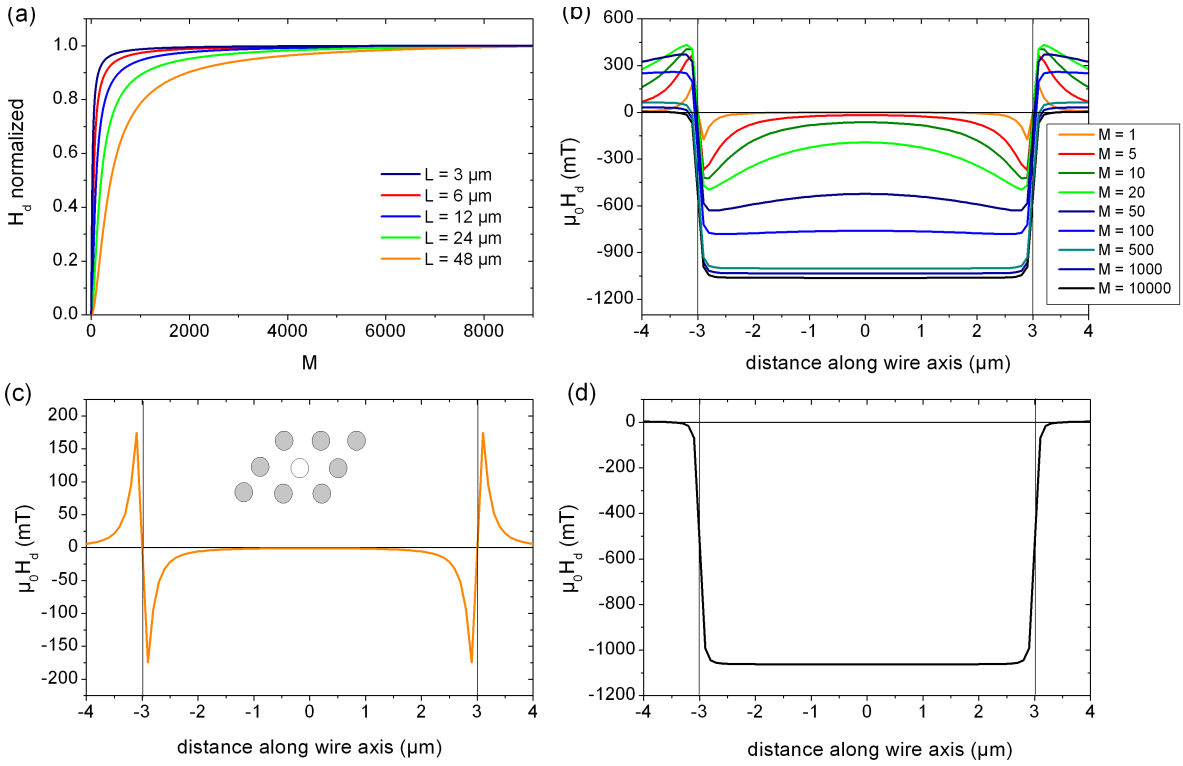


**Figure 6.4:** (a) The dependence of the $_d$ value in the middle ($z = 0$) of the center wire in an array is plotted as a function of $M$, the limit of the sums given in equation (6.11). Convergence is reached for increasing $M$, when the length $L$ of the nanowires is increased. (b) $_d$ for a wire length of $L = 6$ µm is plotted as a function of the position along the center wire axis. The number in the legend denotes the respective $M$ values. For large enough $M$s $H_d$ becomes homogeneous. For better visibility the stray field contribution is plotted separately (c) for $M = 1$ corresponding to 8 surrounding wires as given by the sketch and (d) for $M = 10000$ corresponding to approximately $10000^2$ wires.

The analytically calculated dipole sum is given as 11.034176. With this the above equation can simply be written as [Huc99]:

$$H_d(0,0,0) = -\frac{11.034176}{4\pi}\frac{m_z}{d^3}. \tag{6.13}$$

### Comparison with previous calculations

In order to be able to compare the calculations presented above with existing calculations, it is first necessary to clarify at which position within the wire the values of $H_d$ were obtained. Calculations are carried out either at the wire ends [Nie07, Dob13], in the center of the wires [Ish89, Sam92, Str99, Riv02, Kum06, Sch10a, Gha11, Das12] or the averaged value was considered [Cli06]. Applying the mean field approach by *Netzelmann* and *Skomski* and *Sellmyer* (equations (6.3, 6.4)) also implies an averaged view of $H_d$ [Net90, Zen00, Sko01].

The calculations showed, that for nanowires with aspect ratios larger than 10, the averaged $H_d$ is almost identical with the center $H_d$ value. In contrast to this the $H_d$ value at the wire ends is only half of the value in the wire center (see e.g. Figure 6.4 (d) with $H_d(\text{end}) = -530$ mT). In the following only the $H_d$ value at the center is considered.

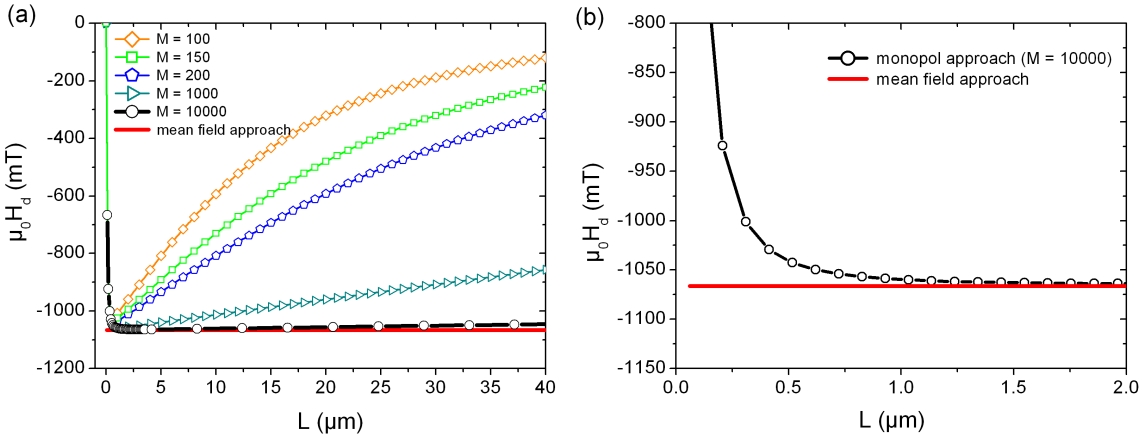


**Figure 6.5:** (a) Dependence of $H_d$ on the length of the nanowires (with $D = 70$ nm and $d = 100$ nm). The dependency is plotted for varying $M$ values, corresponding to varying numbers of nanowires in the array. The solid red line represents the value obtained from the mean field approach by *Skomski* and *Sellmyer* (equation (6.4)). (b) The enlargement of the curve for $M = 10000$ reveals, that for wire lengths below 1 µm $H_d$ differs from the length independent mean field approach.

The length dependency of $H_d$ for varying array sizes is given in Figure 6.5. Arrays with $M = 10000$, for which $H_d$ reached convergence, show only a slight length dependency above a length of 1 µm (an aspect ratio of 14). The $H_d$ value is almost identical to the value obtained from equation (6.4). This is reasonable, when considering the small

error between a monopole approximation and the extended surface charge distribution as calculated numerically (compare Figure 6.2). The calculations for smaller $M$ values demonstrate that calculating too small arrays can have a huge impact on the obtained dependency.

In Figure 6.6 (a) a comparison of the dipole chain approach by *Clime et al.* [Cli06], the mean field approach by *Skomski* and *Sellmyer* [Sko01], the dipole sum and the monopole sum are shown. The increase of the absolute value of $H_d$ is similar, although not identical, for the monopole sum and the dipole chain calculation until a value $L = 17$ µm. Here the *Clime* approach has an inflexion point and intersects with the mean field approach. As mentioned before $H_d$ is expected to converge to the result of equation (6.4) for increasing $L$. The inflexion point in the dipole chain calculation is very likely caused by disregarding the convergence criteria. Convergence was only defined for $L = 10$ µm and not reevaluated for increasing wire length $L$. That this can have a large influence is shown in Figures 6.4 (a) and 6.5. However, in the calculations of *Clime et al.* the effect of a neglected convergence is just opposite to the monopole approach. The absolute value of $H_d$ increases, while smaller arrays in the monopole sum lead to a decrease of $|H_d|$ with $L$. The reason for this is, that *Clime et al.* use a dipole description of the stray field outside a certain region. This is justified only for regions further away than $L$. If this is not fullfilled $|H_d|$ is largely overestimated. The huge overestimation becomes apparent, when calculating the dipole sum after equation 6.13 (Figure 6.6 (a), red symbols and line). For the choice of the dipole approach the limits must be carefully considered, because already slightly too large aspect ratios produce completely unphysical results.

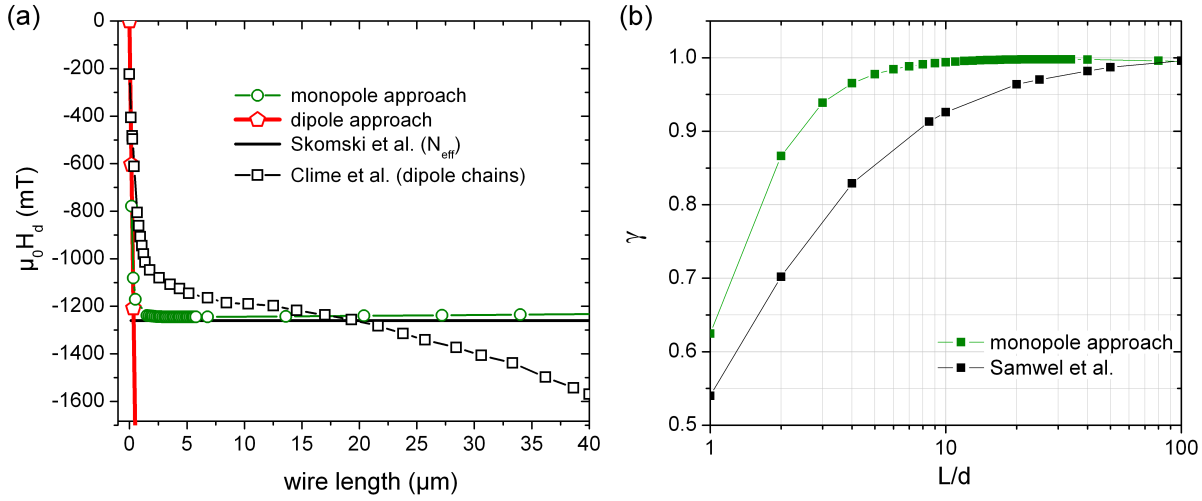


**Figure 6.6:** (a) Comparison of the dipole chain approach of *Clime et al.*, the averaging approach by using $N_{eff}$, the monopole sum and the dipole sum. (b) Comparison of the correction factor $\gamma$ as defined by *Samwel et al.* [Sam92] and from the monopole approach.

Finally, the results of the monopole approach derived above are compared to the calculations of *Samwel et al.* [Sam92], who define a correction factor $\gamma$, which describes the deviation of $H_d$ from a value calculated for an effective magnetization or demagnetizing factor as given by equations (6.3) and (6.4)

$$H_d = \gamma \frac{\pi (D/d)^2}{2\sqrt{3}} M_s. \tag{6.14}$$

With this definition the correction factor of the monopole approach reads

$$\gamma = \frac{\sqrt{3}}{8\pi} \frac{L}{d} \sum_{j=-\infty}^{+\infty} \sum_{\substack{i=-\infty \\ i=j\neq 0}}^{+\infty} \left( \frac{1}{(i^2 + ij + j^2 + (L/2d)^2)^{\frac{3}{2}}} \right). \tag{6.15}$$

A comparison of the $\gamma$ characteristics depending on the $L/d$ ratio is given in Figure 6.6 (b). The monopole approach converges faster to 1. That is the value, where the approximation of an effective magnetization after *Netzelmann et al.* [Net90] and *Skomski* and *Sellmyer* [Sko01] becomes identical with the monopole approach.

## 6.2 Micromagnetic Simulations

Micromagnetic calculations are based on the interaction between magnetic moments on sub-micrometer length scales. They aim to find the lowest energy configuration of magnetic moments in a magnetic volume. Therefore, the sum of several competing energy terms has to be minimized. This is the dipole energy, which is the resultant energy from the interaction of magnetic moments with each other. The exchange energy attempts to align the atomic magnetic moments in the close surrounding to lie parallel to one another (if the material is ferromagnetic). The magnetocrystalline anisotropy energy is low when the magnetic moments are aligned along a particular crystal direction. And the Zeeman energy is at its lowest when magnetic moments lie parallel to an external magnetic field. The competition of these energies under different conditions is responsible for the overall behavior of a magnetic system [Aha96].

The object-oriented micromagnetic framework OOMMF [Don99], which was applied for all micromagnetic calculations presented in the following, allows to find a stable magnetization configuration for given geometry and material parameters by minimizing the four competing energy terms. The OOMMF simulations were carried out by *C. Hengst* and *Dr. M. Wolf* (both IFW Dresden, Institute for Metallic Materials). The problem is solved numerically by subdividing the magnetic volume into three-dimensional cells, which must be smaller than the magnetic exchange length but still large enough to avoid a long

computation time. The magnetic exchange length is defined as $l_{ex} = \sqrt{\frac{2A}{\mu_0 M_s^2}}$ [Hub98]. According to the material properties of CoFe the exchange constant [Bra09b] and saturation magnetization [Coo05] are $A = 26 \cdot 10^{-12}$ J/m and $M_s = 1900$ kA/m, respectively. With this the exchange length becomes 3.4 nm. To simulate a nanowire with similar dimensions to those of the experiment a cylinder (diameter: 70 nm and length: 1 µm) was discretized into (2 x 2 x 2)-nm$^3$ cells. Starting from a fully saturated wire with $M$ along the wire axis the magnetization was relaxed for different magnetic fields until the convergence criterion of $\frac{\delta m}{\delta t} = 0.01$ was reached.

## 6.3 Combination of demagnetizing field calculations and micromagnetic simulation

A combination of the micromagnetic simulation of a single nanowire and the $H_d$ calculation with the monopole approach as derived in Section 6.1.2 is applied in the following to judge the effect of the dipolar fields on the reversal behavior of nanowires embedded in an array. In Section 6.1.2 it was mentioned, that the approaches to calculate the demagnetizing effect in arrays presently available in literature, concentrate on the calculation of a single $H_d$ value at one distinct position along the wire axis. It is not immediately obvious, at which position the value is more reasonable to consider for a deshearing of hysteresis loops. It is in principle questionable, if it is justified to use a single value for the description of the effect of an inhomogeneous field. However, to the authors knowledge, there were no attempts addressing the inhomogeneity effect of $H_d$.

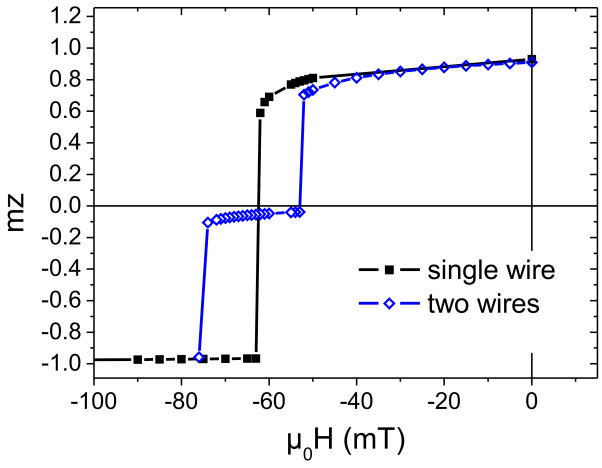


**Figure 6.7:** Hysteresis curves obtained by micromagnetic simulation of a single wire (closed squares) and two neighboring wires (open squares) with a center-to-center distance of 100 nm.

A first simple way to test the effect of an inhomogeneous field on the switching behavior of a nanowire is to compare the hysteresis loop simulation for a single wire and for two neighboring wires ($D$ = 70 nm, $d$ = 100 nm, $L$ = 1 µm). The results are summarized in Figure 6.7. The single wire reverses its magnetization direction at an external field of −62.5 mT. Two neighboring wires influence the hysteretic behavior of each other by destabilizing the parallel and stabilizing the anti-parallel configuration. This results in a step-like demagnetization curve with a first wire switching at approximately −52.5 mT. The now present anti-parallel configuration stabilizes the second wire, which switches at a larger field of about −75 mT. That suggests that the effective field experienced by one wire in the presence of the other is in the order of approximately 10 mT. This value comes closer to the average field value of −12 mT produced by a single wire at the center of an imaginary second wire along the wire axis (compare the $H_z$ calculation for a single wire in Figure 6.2 (b)) than the field at the wire ends, which is only 0.7 mT.

To explore the effect of the stray field of an extended nanowire array on a central nanowire, the micromagnetic hysteresis loop calculation of a single wire is combined with the results of the demagnetizing field calculations. The $H_d$ values for a nanowire array with $L$ = 1 µm were calculated along the axis of the central wire according to equation (6.11) (see Figure 6.8 (a)). The $H_d$ value at the wire end is here −573 mT and in the center −1008 mT. The whole $H_d(kd)$ characteristic was then included in the micromagnetic hysteresis loop calculation of a nanowire with $L$ = 1 µm. Therefore, the inhomogeneous $H_d$(z) and the homogeneous external field $H_z^{ext}(z)$ are superimposed. Hereby, the $x$ and $y$ components of the array's stray field are neglected and it is assumed, that $H_d$ is homogeneous across the wire cross section. The resulting hysteresis loop is given in Figure 6.8 (b)[2]. Assuming symmetry of the hysteresis loop, the resulting switching field of the wire is approximately $H_c \approx 62.5$ mT. The obtained shift of the single wire hysteresis is then 1030 mT. This shift can be regarded as the demagnetizing effect on a central wire caused by the surrounding array in which all nanowires are magnetized parallel. This means, that on the decreasing branch of the hysteresis the first nanowire of the array switches at a value of 967.5 mT. If it is assumed, that $H_d$ scales linearly with the magnetic moment of the array ($H_d \propto M$), then this value is responsible for the shearing of a hysteresis loop of the macroscopic nanowire array. The shift of the field, where the first wire of the array reverses its magnetization on the decreasing branch of the hysteresis loop as obtained from the micromagnetic simulation (967.5 mT) comes very close to the average demagnetizing field (965 mT) of the array along the central wire axis. Concluding, for the estimation of the shearing it is more reasonable to take the average value rather than the value at the wire ends as proposed by *Nielsch et al.* [Nie07].

[2]The particular shape of the hysteresis loop is neglected here, as the main focus is on the demagnetizing field effect by means of delaying or accelerating the switching of a single wire. Nevertheless, the underlying domain processes are of great interest and are investigated at present.

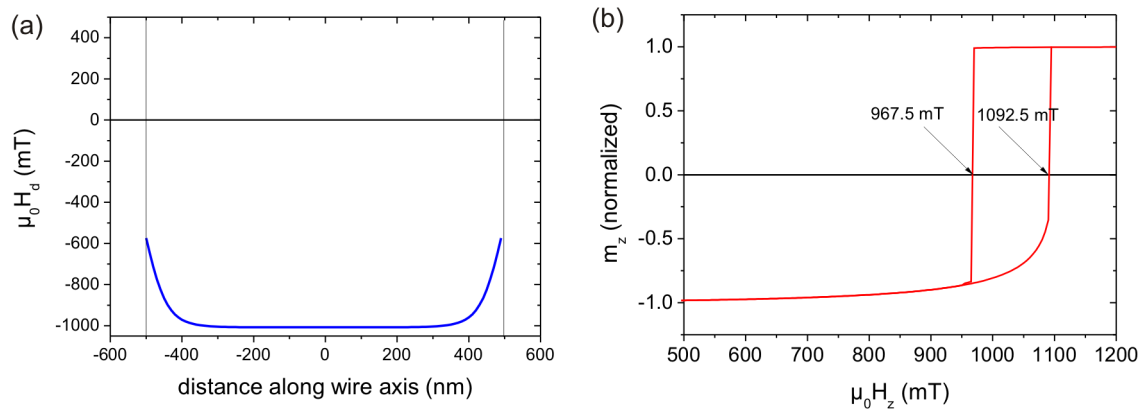


**Figure 6.8:** (a) $H_d$ characteristic, which was superpositioned to obtain (b) the hysteresis loop of a single wire under the influence of a surrounding nanowire array.

## 6.4 Experimental details

Nanowires with a $Co_{48}Fe_{52}$ composition were electrochemically deposited into an anodized aluminum oxide template[3]. Through this procedure a well ordered triangular arrangement of wires with a diameter $d$ of about 70 nm, an inter-pore distance $D$ of about 100 nm and a length of 6 µm is obtained (see Figure 6.9 (a) and (b)). A nearly complete filling of the

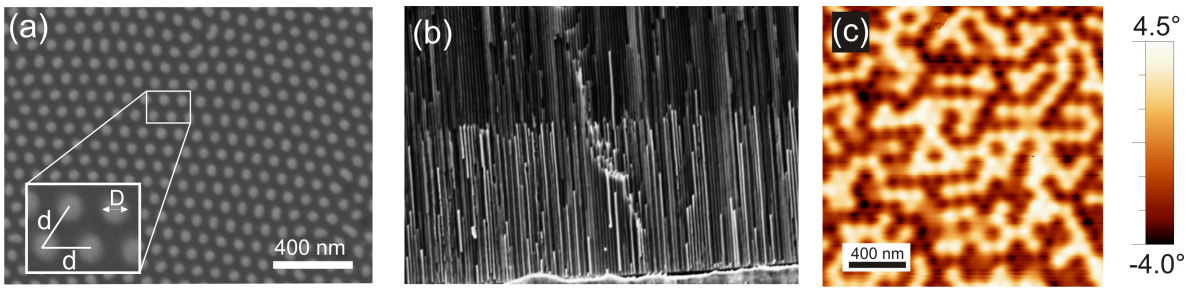


**Figure 6.9:** (a) SEM top view and (b) cross section of the filled $Co_{48}Fe_{52}$ array. (c) MFM overview of the CoFe nanowire array in remanent state.

template could be achieved. The filled template was then ground and polished using a diamond lapping film (Buehler) with decreasing grain sizes from 3 µm to 0.1 µm. The final average roughness is 1.2 nm and the root mean square roughness is 1.7 nm as confirmed by AFM measurements given in Figure 6.10. For MFM analysis the polished CoFe/AAO sample was covered additionally with carbon to avoid electrostatic charging. An exemplary MFM overview image can be found in Figure 6.9 (c). For the given composition a saturation magnetization of $M_s = 1900$ kA/m is expected [Sun05]. To verify this an extended film of

[3]Prepared by Dr. M. Uhlemann, IFW-Dresden, Institute for Complex Materials.

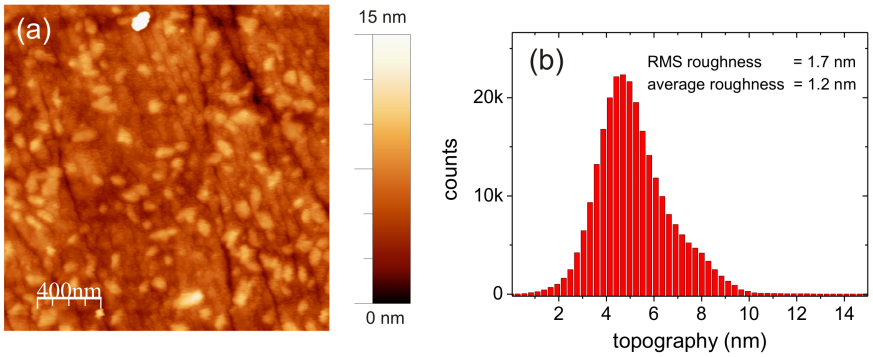


**Figure 6.10:** (a) Topography image of the CoFe-array surface after polishing. (b) Roughness estimation from the histogram of the topography image.

3.5 µm was deposited as reference and the hysteresis curves in in-plane and out-of-plane direction were measured (Figure 6.11). The saturation found in the measurement exactly matches the expected value.

The local magnetization measurements were carried out with the DI 3100 instrument in tapping/lift mode. Perpendicular magnetic fields from 0.05 up to 0.5 T were applied by the additional field option (Section 2.2). The MFM tip used for the presented measurements is a hr-MFM tip (Section 3.4). As these tips provide high resolution and low stray fields, one can easily resolve positively and negatively magnetized wires (Figure 6.9 (c)).

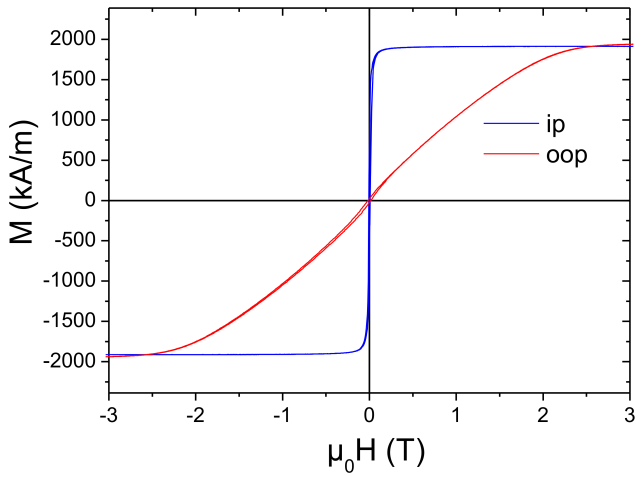


**Figure 6.11:** Parallel (in-plane: ip) and perpendicular (out-of-plane: oop) to the film plane measured hysteresis cycles. $M_s$ of 1900 kA/m can be extracted.

All MFM measurements presented in this chapter are performed at a lift height of 15 nm. The test for mutual influence of tip and sample as introduced in Section 3.6, showed only negligible perturbations. Nevertheless, the MFM tip comes much closer to the surface

during the previous topographic scan, which is in a height of about 15 nm (for a used amplitude setpoint of 1 V) according to the microscope manufacturer. This height adds up to the set lift height during the magnetic measurement and gives a total lift height of 30 nm.

The RSTF (real space tip function) was determined according to the procedure described in Section 3.2 and using the CoPt reference (for details see Section 3.5). The calibration measurement and the determined RSTF at 15 nm lift height are shown in Figure 6.12. The corresponding stray fields $H_z(x)$ of the tip at a distance of 15 nm (during the AFM scan) and 30 nm (during the MFM scan) are given in the diagram in 6.12 (c).

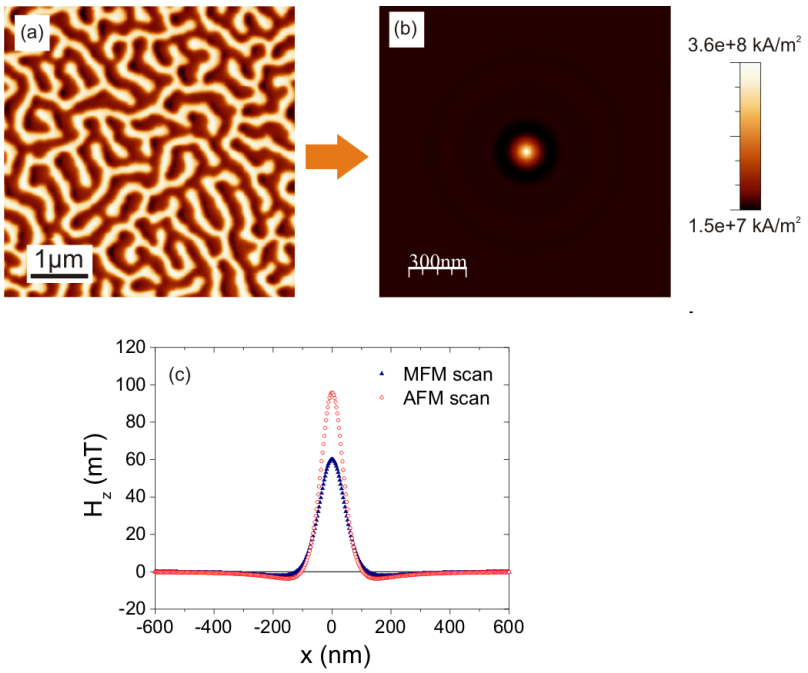


**Figure 6.12:** (a) MFM image of the Co/Pt mulitlayer reference sample used for the tip calibration in a lift height of 15 nm, (b) circular averaged RSTF of the used hr-MFM tip in a distance of $z = 30$ nm (15 nm topographic scan + 15 nm lift height) away from the tip apex, (c) line profiles of the approximate stray field of the tip at a distance of 15 nm during the topographic scan (AFM-open circles) and magnetic (MFM-closed circles) scan at a distance of 30 nm.

## 6.5 Global hysteresis measurements of CoFe nanowire arrays with varying length

Together with the micromagnetic simulation of the hysteresis loop of a single wire presented in Section 6.3 hysteresis loops of arrays are calculated and compared to global VSM measurements.

From the results presented in Section 6.3 it can be concluded, that the field value responsible for the shearing of the array's hysteresis loop is in the order of the $H_d$ value in the center of the nanowire axis. Therefore this value is chosen to shear the hysteresis of a single wire.

Results for CoFe nanowire arrays with varying wire length $L$, but otherwise identical parameters ($D = 70$ nm, $d = 100$ nm, $M_s = 1900$ kA/m) are shown in Figure 6.13. For a wire length up to 6 µm the calculations agree reasonably well with the measurements. From 6.5 µm on an increasing deviation becomes apparent, which can not be explained by the length dependency of $H_d$. In this length range $H_d$ is expected to be constant for large enough arrrays.

Only changing $M$ (upper and lower limit of the sum in equation (6.11)), that is connected to the array size, causes a dependency on the wire length similar to that observed in the experiment. However, as the area of the CoFe arrays was larger than 2 mm$^2$ a finite size effect can be excluded. The change of other parameters, such as $M_s$, $d$ and $D$ in equation (6.11) only leads to an overall shift of $H_d$ and can not explain a wire length dependency, either. *Vázquez et al.* showed that the geometrical disorder present in the nanowire arrays can have a significant influence on the resulting $H_d$ values [Váz04, Váz05]. This aspect has to be further investigated by detailed SEM image analysis of the nanowire arrays.

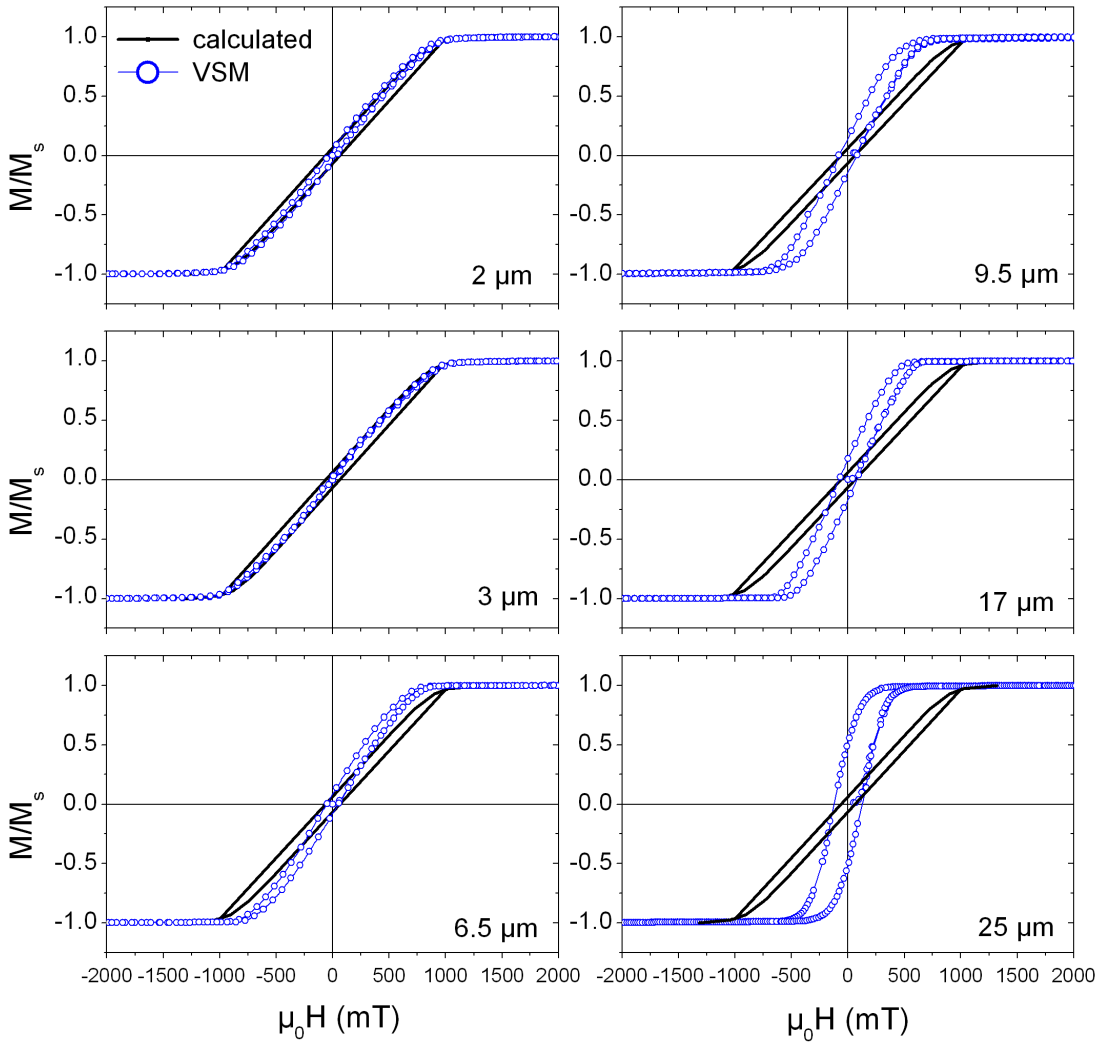


**Figure 6.13:** Measured (VSM) and calculated hysteresis loops for CoFe nanowire arrays with varying length.

## 6.6 Local magnetic characterization of a CoFe nanowire array by quantitative MFM

The MFM studies presented in this section were all carried out for a $Co_{48}Fe_{52}$ nanowire array with the following geometry: $D = 70$ nm, $d = 100$ nm and $L = 6.5$ µm. The experiments of the first part focus on the observation of the magnetization structure at the end of individual nanowires. The second part discusses an in-field MFM study of the switching behavior of nanowires depending on their local environment in order to conclude on the strength of the magnetostatic interaction in the nearest neighborhood.

### 6.6.1 Magnetic structure of individual nanowires

The particular challenge in the case of nanowires arises from the fact that a three dimensional magnetization structure is to be deduced from a single two dimensional MFM measurement. It is not possible to unambiguously solve this problem without additional constraints. For the evaluation method applied in the present case a forward MFM image simulation method was chosen for which two suitable magnetization patterns were assumed and compared with the measurements. To find a realistic magnetization structure, micromagnetic simulations of a single nanowire with the given geometrical parameters were performed.

#### Homogeneous magnetization

For the local quantitative magnetization study a reasonable guess of the effective surface charges is taken and subsequently convolved with the RSTF to obtain a simulated MFM image, which can be compared to the measurement. Two surface charge models of the wires have been considered, which will be discussed in the following.

The wires have an aspect ratio of 114 and the shape anisotropy $K_{sh} = 1/4\mu_0 M_s^2[1 - 3N_z] = 1130$ kJ/m$^3$ (with $N_z = 0.00036$) is more than one order of magnitude larger than the crystalline anisotropy of bcc-Fe ($K_1 = 48$ kJ/m$^3$). Furthermore the wires are polycrystalline with grain sizes of 30 nm, which renders the magnetocrystalline anisotropy of the grains an overall isotropic contribution. All this would suggest a predominantly homogeneous magnetization along the wire axis and a homogeneous effective surface charge distribution (compare Section 1.2.3) of the order of $M_s$ across the wire surface. Thus, the charge profile for a single wire was set constant to a value of 1900 kA/m. Two discrete orientations of the wire magnetization are expected, either pointing upwards (dark MFM contrast, parallel to tip and external field) or downwards (bright MFM contrast, antiparallel

to tip and external field). To come closer to the MFM image of the array, the wire arrangement in the simulation was based on the geometrical data of the porous alumina matrix and the particular direction of each wire magnetization was assigned according to the given MFM image section. The result can be seen in Figure 6.16 (red frame).

### Vortex structure

A more realistic magnetization structure can be predicted with the help of micromagnetic simulations of a single wire as introduced in Section 6.2. A simulated CoFe nanowire in an external field of $H_{ext} = 0$ mT shows the presence of a magnetic vortex at the wire ends (Figure 6.14 (a)). In single domain nanowires the magnetostatic energy at the wire ends is reduced by forming a vortex type configuration of the magnetic moments. In this configuration the moments tend to have a large in-plane component at the wire ends in order to reduce stray field energy on the cost of exchange energy. To avoid surface poles at the sides of the nanowire, the moments rotate circumferentially around the wire axis achieving a radial flux closure and herewith a minimization of the stray field energy. With increasing $z$-distance from the wire ends the moments align gradually parallel to the wire axis (the $z$-component of the magnetization increases) and show a homogeneous magnetization throughout the wire ($m_z = M_s$, Figure 6.14 (b)). A magnetic vortex is a well-known configuration for confined magnetic objects and has already been qualitatively observed with MFM in permalloy dots [Shi00]. Micromagnetic simulations have been published showing a similar vortex-type structure for Ni and Co based nanowires (see e.g. [Her02, Her04, Váz11]).

In order to include the vortex in the MFM image simulation it has to be exactly quantified utilizing the given simulation results. Therefore the vortex is described in terms of effective surface charges $\sigma_{eff}(x, y)$. Magnetic surface charges are defined as $\sigma = \mu_0 \mathbf{nM}$, where $\mathbf{n}$ is the outward directed surface normal and volume charges are given by $\rho = div\mathbf{M}$. Since MFM is a depth-sensitive method, it is not sufficient to analyze only the charges generated by the discontinuity at the surface itself. As the magnetization's $z$-component is inhomogeneous along the $z$-axis (compare Figure 6.14 (b)) internal charges have to be taken into account, since they also contribute to the MFM signal, even though they possess a smaller influence being further away than the actual surface charges (see sketch in Figure 6.15). Using the known exponential decay behavior of stray fields [Ber94, Hug98, vS00, Mey04] and the corresponding charges, the effective surface charge is calculated by summing up the surface charges and the volume contributions (Figure 6.14 (d)):

$$\tilde{\sigma}_{eff}(\mathbf{k}) = \bar{m}_z^0(\mathbf{k}) + \sum_{n=2}^{N} (\bar{m}_z^n(\mathbf{k}) - \bar{m}_z^{n-1}(\mathbf{k})) \cdot e^{-kn\Delta z} \tag{6.16}$$

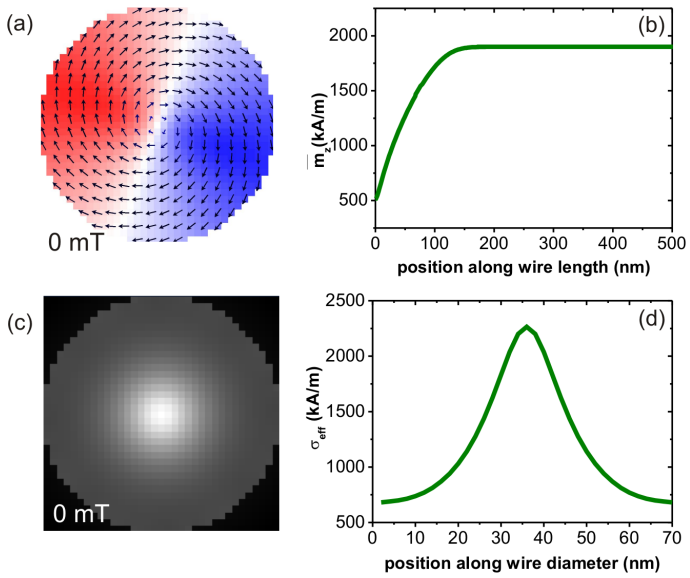


**Figure 6.14:** Visualization of the vortex: (a) top view at 0 mT; (b) depth extension of the vortex: $\sigma_{avrg}$ as a function of position along the wire length (until the wire center at 500 nm); (c) $\sigma_{eff}(x, y)$ of the vortex in 0 mT; (d) line profile of $\sigma_{eff}$

with the average magnetization $\bar{m}_z^n = \frac{1}{2}(m_z^{n-1} + m_z^n)$ within a defined cell volume depending on the chosen degree of discretization $N$. The term $\bar{m}_z^n(\mathbf{k}) - \bar{m}_z^{n-1}(\mathbf{k})$ describes the $z$-contribution of the volume charges. The level of sufficient discretization is given by $N$ at which $\tilde{\sigma}_{eff}$ runs into saturation. The volume of interest is limited to the part where $M_z$ is not constant. The so obtained $\sigma_{eff}$ of the micromagnetically simulated nanowire is characterized by a peaked profile with a maximum value larger than $M_s$ (see Figures 6.14 (c) and (d) for two- and one-dimensional representation). Implementing $\sigma_{eff}(x, y)$ into the nanowire arrangement as described for the homogeneous magnetization and convolving it with the RSTF leads to the results in Figure 6.16 (c) (green profiles).

Test simulations with a longer wire (2 µm) showed no influence of the wire length on the vortex. The demagnetizing energy at the wire end is dominant and in competition with the exchange energy responsible for the vortex geometry and therefore not influenced by increasing aspect ratios, which for the 1 µm wire is already 14.

### Comparison

The measured MFM image and the corresponding simulated MFM images are shown in Figure 6.16 (a) and (b), respectively. The arrows and numbers on the left indicate different line profiles through the images. The comparison of the simulated (for the homogeneous

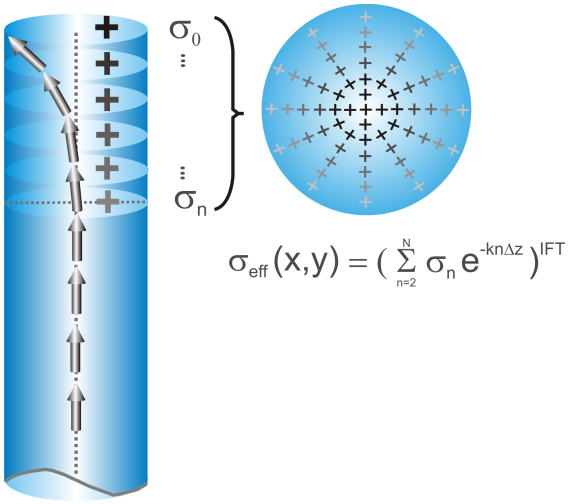


**Figure 6.15:** Schematic representation of the calculation of $\sigma_{eff}$ by discretizing the volume close to the wire end. Starting from a quasi-continuous configuration given by the micromagnetic simulation, the volume is discretized and inner "surface" charges are deduced by averaging the magnetization within each cell and calculation of the charge by $\sigma = \mathbf{nM}$. $\sigma_{eff}$ results from summing up the surface charges after having been weighted by the distance to the surface.

magnetization, red) and measured (black) line profiles clearly shows a large overestimation of the present effective surface charges in the nanowires.

In a next step, the $\sigma_{eff}(x, y)$ distribution calculated from the OOMF simulation was implemented into the nanowire arrangement. Convolving this with the RSTF leads to the results in Figure 6.16 (c) (green frame and green profiles). The obtained profiles fit the measurement much better, than in the previous approach. The simple assumption of a homogeneously magnetized wire is obviously wrong and leads to a huge overestimation of the magnetic stray field produced by the nanowires. Thus, one can conclude, that the presence of a magnetic vortex with the given configuration is very likely for most of the imaged wires. The experiment clearly demonstrates, that the applied quantitative MFM procedure is able to prove the existence of a magnetic vortex state at the end of the nanowires. Furthermore the depth sensitivity of MFM could be correctly included by taking the volume contributions of the magnetic charges into account. The micromagnetic simulations of a single wire were proven to be representative for the wires assembled in the array in the as-prepared state without external field.

### 6.6.2 Magnetization reversal of the nanowire array

That the arrangement of nanowires into an array leads to strong long range magnetostatic interactions has already been shown in the first part of this chapter (Sections 6.3, 6.1.2 and

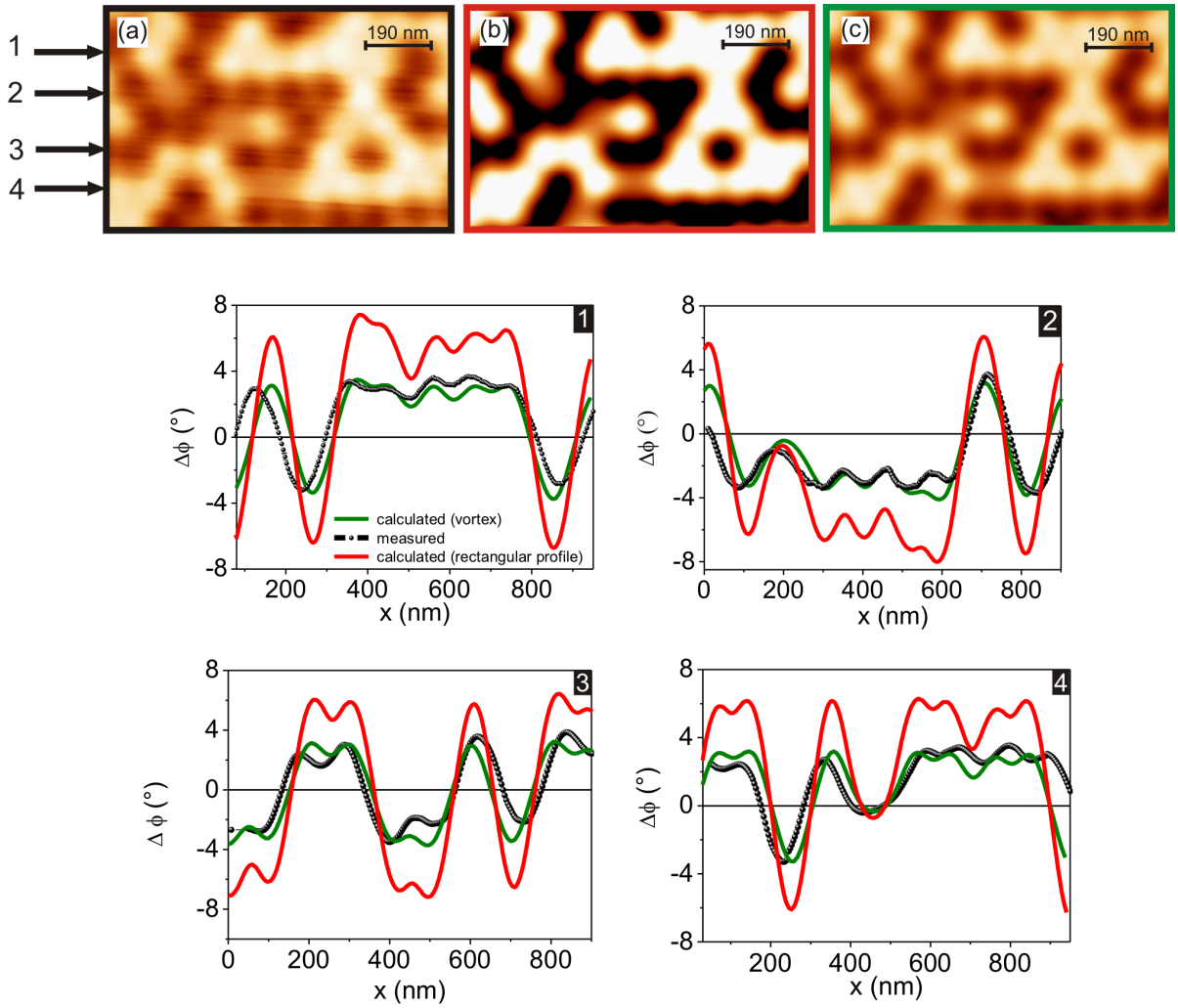


**Figure 6.16:** The images show a section of the measured MFM data (black frame) and the simulated data for the case of homogeneous magnetization with $\sigma_{eff} = M_s$ (red frame) and the $\sigma_{eff}$ profile calculated by micromagnetic simulation (green frame). The arrows indicate the positions of the profiles shown in the diagrams below. The line colors are chosen corresponding to the images above.

6.5). Whether this magnetostatic interaction is large enough to influence the magnetization reversal also on a local scale can not be deduced from a measurement of the overall moment. Therefore, MFM measurements in increasing fields were analyzed to reveal, if the wire reversal takes place in an uncorrelated or correlated manner. The first question to answer is, whether the imaged section of the array represents the global magnetic moment.

### Comparison of global and local magnetization measurements

The global VSM measurement is shown in Figure 6.17. A coercivity of $\mu_0 H_c = 53$ mT and a remanence ratio of $M/M_r = 0.1$ can be extracted from the data of the parallel field measurement. The $\mu_0 H_c$ value is close but not identical to the value obtained by micromagnetic simulations (62.5 mT; compare Section 6.2). It is clear that the simulation of a perfect cylindrical object can never describe the reversal in a real nanowire accurately. Furthermore, the arrangement of the wires in an array and the magnetic interaction among them can influence the coercive field [Her02,Esc08,Lim10][4], which may explain the observed discrepancy.

MFM images in varying external fields from 0 to 500 mT along the initial magnetization curve were recorded (Figure 6.18, left column). Wires appearing bright are magnetized anti-parallel and dark wires are magnetized parallel to the external field. Therefore, the number of bright wires decreases, while the number of dark wires increases with increasing field.

In order to compare the globally measured results with the local MFM measurement, the number of bright and dark wires in the MFM images has been counted and the resulting initial curve calculated by

$$\frac{M}{M_s} = \frac{N_{dark} - N_{bright}}{N_{dark} + N_{bright}} \tag{6.17}$$

where $N_{dark}$ and $N_{bright}$ stand for the number of bright and dark wires, respectively. The black line and black open circles in Figure 6.17 represent the counting result, whereas the solid red line shows the VSM data. Except for 0 and 50 mT, the local data matches exactly the global curve, proving that the relation between bright and dark wires equals the overall magnetic moment of the array. This is a strong indication for a single domain and bistable magnetization configuration of the wires. Similar results have been published earlier [Nie01, Ase06, Jaa08]. Based on these findings it will be presumed, that the sign of the detected MFM signal is representative for the global wire moment. From this follows that the measured area of 4 µm$^2$ is large enough to conclude on the overall behavior of the

[4] This is also in accordance with the results in Section 6.3, where a coercive field of approximately $H_c = 48.5$ mT was obtained, which is 14 mT lower than the value resulting from the simulation of the single wire.

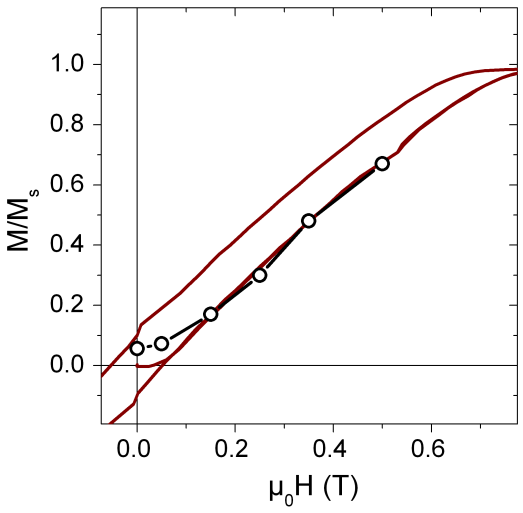


**Figure 6.17:** Global hysteresis loops as measured by VSM with the external field applied parallel (red) to the wire axis. The black open circles visualize the counting result as explained in the text.

sample. Nevertheless, the deviations in the lower part (Figure 6.17) are too large to be neglected. A very likely reason for the non-zero magnetization at zero field is the presence of the tip field. That this can have a large influence on the switching in a magnetic array was also shown by other groups [Nie02, Ase06, Esc07]. The tip field during the topographic scan (compare Figure 6.12), where the tip is as close as 15 nm to the surface of the array, reaches a maximum value of 96 mT, which is large enough to overcome the field necessary to switch the magnetization of a number of nanowires according to the hysteresis curve (Figure 6.17). Lifting the tip in the subsequent MFM scan 15 nm further away, leaves the nanowire array in a remanent state, close to the overall remanence value.

### Influence of magnetostatic interactions on local switching events

Both, from a fundamental and applied point of view, it is interesting to understand the switching behavior of individual wires depending on their closest surrounding. In the presence of a global homogeneous demagnetizing field without local short range interaction, the switching processes of the individual nanowires are expected to be fully uncorrelated. Switching would take place completely statistically and the local magnetic arrangement would exhibit random nature along the magnetization curve.

Due to the stray field influence of the nearest neighbors in the present dense nanowire array, however, a non-statistical switching behavior can occur, if the nearest neighbor influence

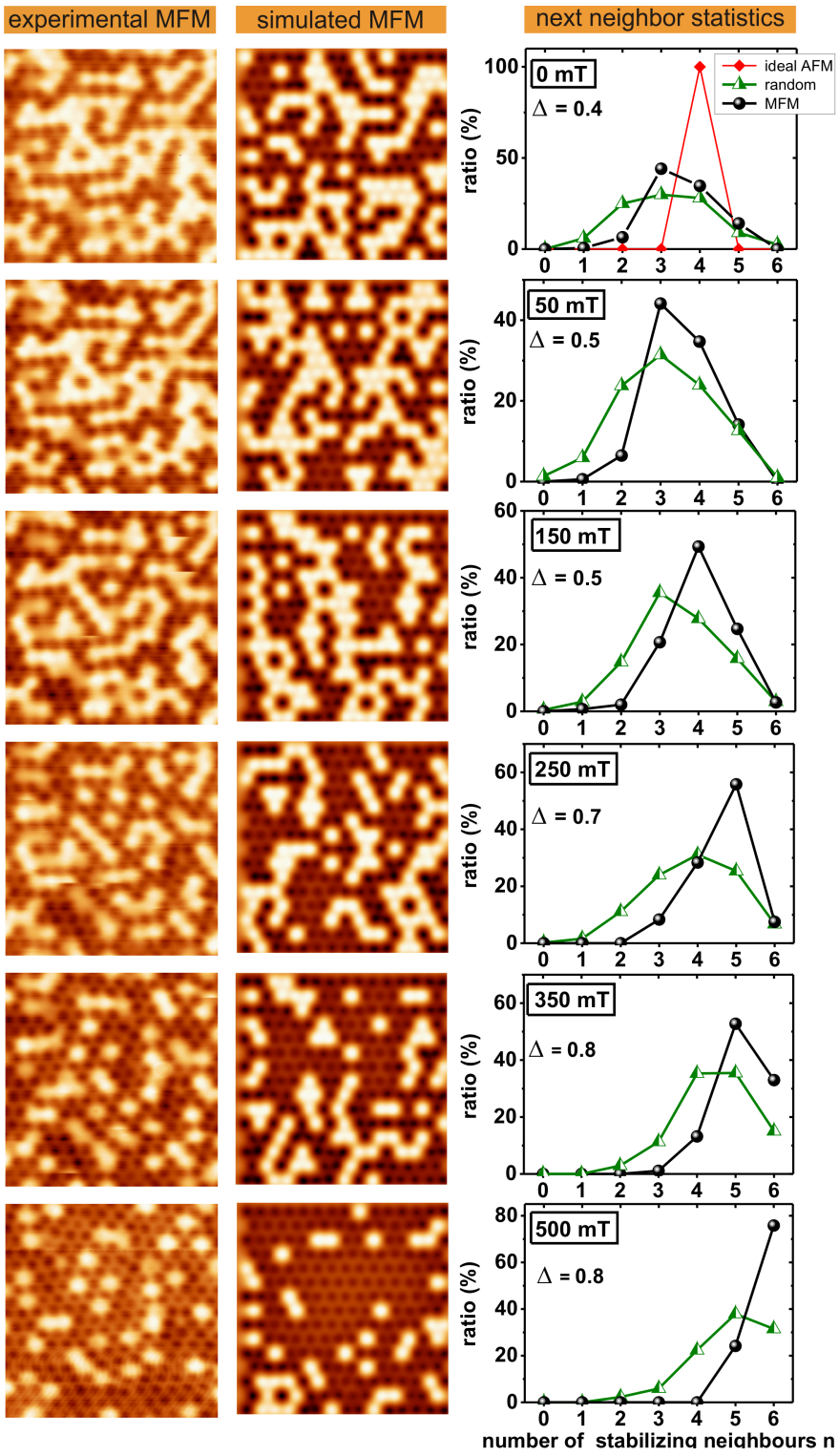


**Figure 6.18:** Overview over the MFM images (left row), their statistical simulations (middle row) and the result of the nearest neighbor quantification (right row) for the measured and the statistical distribution. All images are 1.5 µm x 1.5 µm. The diagram gives the ratio of each nearest neighbor configuration, which is quantified by the number $n$ of anti-parallel (dark) wires around each bright wire. In an increasing external field (anti-parallel to the bright wires) this number denotes a "degree of stabilization" of the anti-parallel magnetized center wire. The value $\Delta$ quantifies the difference between the configuration in the random distribution ($\Delta$) and the measured MFM ($\circ$). It is calculated from the difference of the mean $n$ values of both distributions.

is no longer negligible compared to the certainly present switching field distribution of the nanowires. During the course of magnetization, already switched wires (dark contrast, Figure 6.18, first column) are expected to stabilize neighboring non-switched wires (bright contrast) and will shift their switching event to higher external fields.

The in-field MFM observation allows to directly quantify correlated versus uncorrelated wire switching by a statistical analysis of the switching events [Suc09]. Thus for every field the nearest neighbors of each bright wire have been analyzed and the number of dark wires $n$ was counted. The corresponding histograms are displayed in the right column of Figure 6.18 (black dots and line). As the dark wires are always oriented anti-parallel to the bright center wire, their number $n$ can be considered as a degree of stabilization of the center wire against switching in the external field. For example $n = 0$ means, that all surrounding wires exhibit parallel magnetization. This is the case where magnetostatic interaction destabilizes and accelerates the switching of the center wire. The opposite situation occurs for $n = 6$, where the surrounding wires are all magnetized anti-parallel and, therefore, have a stabilizing effect and the switching of the center wire is retarded (compare Figure 6.7).

For comparison the histogram of the configuration occurring for a statistical wire switching was considered as well. Here the magnetization of each wire has been assigned randomly (dark and bright). The overall magnetic moment in increasing external fields has been accounted for by shifting the random distribution probabilities according to the ratio of dark and bright contrast in the measured images (middle column of Figure 6.18). The present nearest neighbor configurations are summarized in the diagrams (green triangles and line in the diagrams in Figure 6.18). For the quantification of the nearest neighbor configuration a larger area than shown in the image has been evaluated to achieve better statistics.

In the zero field MFM image (Figure 6.18 first row, left image) the overall magnetic moment is close to zero. One observes a pattern comparable to the maze domains of continuous films with perpendicular magnetic anisotropy. Similar MFM images of nanowire arrays and other perpendicular bit patterned media with hexagonal lattice have been published by other authors [Nie02, Ase06, Hel13].

Strong dipolar interactions on a local scale should result in a specific antiferromagnetic (AFM) state of the neighboring wire magnetizations [Bis02], that represents the lowest energy magneto-static configuration. For the simple case of a square lattice the energetically most favorable distribution is a checkerboard pattern. As in the present case the lattice is triangular, the situation becomes more complicated. This kind of lattice is known as a typical frustrated system for AFM ordering, where the geometric frustration is present

even for the simplest nearest-neighbor interaction [Kir12]. It is not obvious which configuration will constitute the ground state. In fact there are six energetically equal states found by Kireev et al. [Kir12]. All the minimal energy states show a periodic distribution of moments, where the nearest neighbors are of the 4-2 type (2 of one and 4 of the other population, see Figure 6.19). The optimal situation for an AFM state would clearly be the 3-3 type (equal amount of bright and dark neighboring wires), but this is not possible due to frustration in the system.

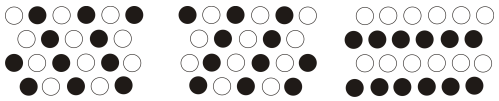

**Figure 6.19:** Different energetically equal 4-2 type magnetization configurations as given by Kireev et al. [Kir12].

In contrast to the predicted periodic 4-2 type ordering, the measured zero field MFM image does not reveal a periodicity of this type (Figure 6.18, first row, left image). In addition, the amount of the different nearest neighbor configurations (black symbols and line) for 0 mT (Figure 6.18, first row, diagram) reveals the 3-3 type ($n = 3$) as the most probable type, shortly followed by the 4-2 type state ($n = 4$). Only few states exist with $n < 3$, whereas states with $n > 4$ have a higher amount (compare ideal AFM state in Figure 6.18, red curve).

From the artificial MFM image for 0 mT (first image in second column of Figure 6.18) one can see, that the random configuration does not lead to a more homogeneously distributed bright and dark contrast. In fact, chains and larger areas of only one population are very likely to form. The quantitative comparison of measurement and random distribution is shown in the diagrams (black circles and green triangles). The measured histogram obviously deviates from the 4-2 ground state (see red square), and is much closer to the random 3-3 distribution. Nevertheless the experimentally analyzed nearest neighbor histogram is shifted to higher values of $n$ with respect to a pure statistical distribution. The interpretation on hand agrees with the already mentioned destabilizing effect of parallel magnetized wires. A logical consequence of such an interaction is a depletion of parallel wires in the next neighborhood of a center wire and thus an increase in n. To this end the mean value $\bar{n}$ of the statistical $\bar{n}_{stat}$ and the experimental $\bar{n}_{exp}$ configuration have been calculated from the histograms for all field values and their difference was denoted as $\Delta = \bar{n}_{exp} - \bar{n}_{stat}$. As expected, with increasing magnetization, $\bar{n}_{stat}$ moves to higher values simply from the fact, that with progressive switching the number of dark wires and with it $n$ increases. The same trend is valid for $\bar{n}_{exp}$, just that $\bar{n}_{exp}$ increases even faster with applied field, as is obvious from the difference $\Delta$, which increases from $\Delta = 0.4$ for $H = 0$ to $\Delta = 0.8$ for H = 500 mT, exactly as one expects from the local magnetostatic interaction: with increasing field and thus larger average number of positively magnetized wires

the stray field acting on the center wire increases progressively, leading to the observed growing gap between statistical and experimental configuration histogram. Qualitatively this effect is also visible in a larger (non-statistical) number of isolated bright wires in the MFM experiment at higher fields.

From the above findings one can conclude, that the local nearest neighbor magnetostatic interaction (which deviates from the globally averaged stray field interaction), has a measurable effect on the switching statistic of the individual nanowires. On the other hand, the theoretical ground state of strongly interacting nanowires (4-2 type arrangement) on a triangular grid is not observed. Considering, that the statistical state is energetically only a few % above the ground state, as e.g. demonstrated by Escrig et al. with Monte Carlo Simulations for a Ni nanowire array ($d = 500$ nm, $D = 180$ nm, $L = 6$ µm) [Esc07], and also considering that additional small fluctuations in the inter-pore distance may exist, it is clear, that other configurations than the 4-2 type can be favored as well. Despite that, the local nearest neighbor interaction is clearly observable in the switching statistics. This points towards a distribution of intrinsic switching fields of the wire array of similar magnitude as the effect of the interaction field. The close surrounding ($M = 1, 8$ nanowires) has been shown to contribute to the overall field by an average value of $-15$ mT (compare Figure 6.4 (c)). This demonstrates a rather good homogeneity of magnetic properties within the array.

## 6.7 Summary

A theoretical description of the demagnetizing fields in a nanowire array was derived by approximating the magnetization of an individual wire with monopoles located at their ends. This monopole approach allows a length- and position-dependent calculation of the stray fields present in an array. Combining the so calculated stray field distribution with a micromagnetic simulation of a single wire, revealed the effect of an extended array on a single nanowire, without the need of simulating the whole wire arrangement. The result shows, that the stray field responsible for the shearing of the global hysteresis loop is the averaged field along the central nanowire's length, rather than the value at the nanowire ends as reported earlier [Nie07, Kum06, Sch10a, Dob13]. Comparison of calculated and experimental hysteresis loops of CoFe nanowire arrays with different wire length showed a good agreement for aspect ratios below 100. The increasing difference for larger aspect ratios can not be explained in the framework of the monopole approach.

MFM imaging of a CoFe nanowire array with wire lengths of 6.5 µm allowed a detailed characterization of the magnetic structure of individual wires and the analysis of the nanowire switching behavior. By combining experiment and micromagnetic simulation a magnetic

vortex could be observed at the ends of the nanowires. The method requires the application of a quantitative MFM procedure including a preceding tip calibration. The perfect agreement between measurement and micromagnetic calculation leads to the conclusion, that a magnetic vortex has to be present at the wire ends to be able to understand the signal strength in the MFM experiment. The micromagnetic simulations of a single wire were proven to be representative for the wires assembled in the array in the abscence of an external field.

In-field MFM measurements gave insight into the local ordering of the nanowires' magnetic moments. In the demagnetized as-prepared state and in small external fields the arrangement of the approximately equal number of positively and negatively magnetized nanowires obeys a statistical distribution demonstrating that the fully ordered ground state is not accessible due to the competition of positional disorder and weak local interactions. At higher fields an increasing role of local interactions is observed in a non-statistical nearest neighbor configuration of switching wires. Nanowires in a less stable magnetostatic environment switch preferably into the external field direction.

# Conclusions and Outlook

In this work the problem of quantitative MFM image evaluation was addressed and successfully solved for different physical problems. Two approaches were utilized for this purpose. While a model based real space description was applied to describe the behavior of Fe-CNT probes, a special deconvolution algorithm based on the Fourier transform approach introduced by *Hug et al.* [Hug98] was developed to enable fast quantitative MFM with arbitrary probe shapes. With this algorithm on hand it became possible to globally characterize MFM tips (as opposed to tip model based approaches), to estimate the resolution in MFM experiments and to gain insight into the nanomagnetism of different materials. In the following the explicit results of the quantitative MFM analyses are given in detail.

Fe-CNT as novel MFM probes enable a straightforward real space quantification of MFM data. It was shown, that these probes can be well described by a magnetic monopole approximation. The advantage of such a monopole behavior is the independence of tip parameters on the measured domain size. This could be confirmed by calibrating the tip on patterned (Co/Pt) stripes with varying width. While commercial probes showed a clear dependency on the stripe width, the model parameters of the Fe-CNT probes remained constant. Applying this knowledge for a quantitative investigation of a multilayer, a deviation of the remanent magnetization in the domains from the expected perfectly perpendicular orientation could be resolved, which is otherwise not accessible with global averaging measurement methods.

For the following work the more generally applicable and tip independent deconvolution approach was utilized. Its application enabled to remove the tip influence on measured magnetic object sizes. This was shown for two different physical problems. First, the bubble domain diameter evolution in a $[Co/Pd]_{80}$ multilayer as a function of an applied field was quantitatively described. The results are in excellent agreement with a micromagnetic model for equilibrium bubble domain sizes in multilayer structures introduced by *Kiselev* and *Bogdanov* [Bra09a]. Secondly, the evaluation of the magnetic penetration depth in a superconducting $BaFe_2(As_{0.24}P_{0.76})_2$ single crystal was realized. The performance of the frequently used monopole monopole model and the deconvolution approach was tested on simulated MFM images. The inaccuracy of a monopole description of the magnetic stray field of vortices in superconducting thin films was pointed out. Furthermore, the results

verified the robustness of the deconvolution approach to retrieve accurate values for the penetration depth independent of the measurement distance in MFM experiments.

A large part of the thesis is devoted to a thorough understanding of the magnetism in $Co_{48}Fe_{52}$ nanowire arrays on a local and global scale. To be able to quantify the internal magnetic fields in such an array, a theoretical model was derived. This allows, in contrast to presently available models the position dependent calculation of the internal field along the length of an individual wire. The so derived inhomogeneous stray field and a micromagnetic calculation could be superimposed in order to calculate the effect of the stray field of an extended array on the individual nanowire. The result showed, that the stray field averaged along the wire length is responsible for the globally measured demagnetizing effect in a nanowire array. On the basis of these findings, the hysteresis loops were calculated for arrays with varying nanowire lengths. The comparison with experimentally measured hysteresis curves was in good agreement for wire aspect ratios up to 10. The dependence of the demagnetizing field on larger aspect ratios could, however, not be explained within this approach. Detailed micromagnetic simulations with varying nanowire length are necessary for further investigations on this topic. The idea of combining analytical calculations of internal fields and micromagnetic simulations are suggested for a general use in micromagnetism of nanoparticle arrays and particulate media. This hybrid approach will avoid the limits of standard computational power, when it comes to simulation of whole ensembles of magnetic nanoparticles.

The local quantitative MFM study in combination with the micromagnetic simulation of a single $Co_{48}Fe_{52}$ nanowire enabled the experimental verification of a vortex at the nanowire ends. At the same time, this proves the power of MFM for depth resolved imaging. This result motivates further efforts to develop a deconvolutional approach including the third dimension. In principle, the direct deconvolution should be applicable in three dimensions in a similar manner as introduced in this work. The implementation of such an approach would have great importance for resolving e.g. the magnetic structure in [(Co/Pt)/Ir] multilayers as presented in the work of *Bran* [Bra10].

The statistical analysis of MFM images in varying external magnetic fields could evidence that a nearest neighbor interaction is present in dense CoFe nanowire arrays. This means that the switching events of individual nanowires are correlated to their neighborhood, which is particularly pronounced in increasing external fields.

Quantitative MFM based on a tip calibration procedure and deconvolution method opened the path for new local investigations of the inhomogeneous magnetization structure of magnetic nanoobjects and will find numerous important applications in magnetism and materials development.

# Bibliography


[Abe98] L. Abelmann, S. Porthun, M. Haast, C. Lodder, A. Moser, M.E. Best, P.J.A. Van Schendel, B. Stiefel and H.J. Hug. Comparing The Resolution Of Magnetic Force Microscopes Using The Camst Reference Samples. *J. Magn. Magn. Mater.* **190**, 135 (1998)

[Abr88] D. W. Abraham, C. C. Williams and H.K. Wickramasinghe. Measurement of in-plane magnetization by force microscopy. *Appl. Phys. Lett.* **53**, 1446 (1988)

[Aha96] A. Aharoni. *Introduction to the theory of ferromagnetism.* Clarendon Press - Oxford (1996)

[Ase06] A. Asenjo, M. Jaafar, D. Navas and M. Vázquez. Quantitative magnetic force microscopy analysis of the magnetization process in nanowire arrays. *J. Appl. Phys.* **100**, 023909 (2006)

[Bán05] A. Bányasz, E. Mátyus and E. Keszei. Deconvolution of ultrafast kinetic data with inverse filtering. *Radiat. Phys. Chem.* **72**, 235 (2005)

[Bán06] A. Bányász and E. Keszei. Model-free deconvolution of femtosecond kinetic data. *J. Phys. Chem. A* **110**, 6192 (2006)

[Bel04] M. Beleggia, S. Tandon, Y. Zhu and M. De Graef. On the magnetostatic interactions between nanoparticles of arbitrary shape. *J. Magn. Magn. Mat.* **278**, 270 (2004)

[Ber94] H. N. Bertram. *Theory of Magnetic Recording.* Cambridge University Press (1994)

[Ber95] M. Bertero, P. Boccacci and F. Maggio. Regularization methods in image restoration: An application to HST images. *Int. J. Imag. Syst. Tech.* **6**, 376 (1995)

[Ber98] M. Bertero and P. Boccacci. *Introduction to inverse problems in imaging.* IOP Publishing Ltd (1998)

[Bin82] G. Binning, H. Rohrer, Ch. Gerber and E. Weibel. Surface Studies by Scanning Tunneling Microscopy. *Phys. Rev. Lett.* **49**, 57 (1982)

[Bis02] J. E. L. Bishop, A. Yu. Galkin and B. A. Ivanov. Ground states of an array of magnetic dots with Ising-type anisotropy and subject to a normal magnetic field. *Phys. Rev. B* **65**, 174403 (2002)

[Bra09a] C. Bran, A. B. Butenko, N. S. Kiselev, U. Wolff, L. Schultz, O. Hellwig, U. K. Rößler, A. N. Bogdanov and V. Neu. Evolution of stripe and bubble domains in antiferromagnetically coupled $[(Co/Pt)_8/Co/Ru]_{18}$ multilayers. *Phys. Rev. B* **79**, 024430 (2009)

[Bra09b] J. Brandenburg, R. Hühne, L. Schultz and V. Neu. Domain structure of epitaxial Co films with perpendicular anisotropy. *Phys. Rev. B* **79**, 054429 (2009)

[Bra10] C. Bran. *Domain structure and magnetization processes of complex magnetic multilayers.* PhD Thesis, Technical University Dresden, Faculty of Mathematics and Natural Sciences (2010)

[Buc08] W. Buckel and R. Kleiner. *Supraleitung: Grundlagen und Anwendungen.* John Wiley & Sons (2008)

[Can04] F. M. Candocia, E. B. Svedberg, D. Litvinov and S. Khizroev. Deconvolution processing for increasing the resolution of magnetic force microscopy measurements. *Nanotechnology* **15**, 575 (2004)

[Car00] G. Carneiro and E. H. Brandt. Vortex lines in films: Fields and interactions. *Phys. Rev. B* **61**, 6370 (2000)

[CLA10] *internet source: http://c/ismm.cs.unc.edu/resources/software-manuals/clarity-deconvolution-library* (2010)

[Cli06] L. Clime, P. Ciureanu and A. Yelon. Magnetostatic interactions in dense nanowire arrays. *J. Magn. Magn. Mat.* **297**, 60 (2006)

[Coo05] E. I. Cooper, C. Bonhote, J. Heidmann, Y. Hsu, P. Kern, J. W. Lam, M. Ramasubramanian, N. Robertson, L. T. Romankiw and H. Xu. Recent developments in high-moment electroplated materials for recording heads. *IBM J. RES. DEV.* **49**, 103 (2005)

[Dan06] H.-U. Danzebrink, L. Koenders, G. Wilkening, A. Yacoot and H. Kunzmann. Advances in Scanning Force Microscopy for Dimensional Metrology. *Annals of the CIRP* **55**, 841 (2006)

[Das12] B. Das, K. Mandal, P. Sen, A. Bakshi and P. Das. Directional change of magnetic easy axis of arrays of cobalt nanowires: Role of non-dipolar magnetostatic interaction. *Physica B: Condensed Matter* (2012)

[Dav04] J. E. Davies, O. Hellwig, E. E. Fullerton, G. Denbeaux, J. B. Kortright and K. Liu. Magnetization reversal of $Co/Pt$ multilayers: Microscopic origin of high-field magnetic irreversibility. *Phys. Rev. B* **70**, 224434 (2004)

[dL04] E. d. T. de Lacheisserie, D. Gignoux and M. Schlenker. *Magnetism: Materials and applications*, Vol. 2. Springer (2004)

[Dob09] A.N. Dobrynin, V.M.T.S. Barthem and D. Givord. Revisiting magnetization processes in granular hard magnetic materials. *Appl. Phys. Lett.* **95**, 052511 (2009)

[Dob10] A.N. Dobrynin, V.M.T.S. Barthem, F. Ingwiller and D. Givord. Influence of dipolar collective effects on coercivity and demagnetizing factors in hard magnetic materials. *Phys. Rev. B* **81**, 172403 (2010)

[Dob13] C.-I. Dobrota and A. Stancu. What does a first-order reversal curve diagram really mean? A study case: Array of ferromagnetic nanowires. *J. of Appl. Phys.* **113**, 043928 (2013)

[Don99] M. Donahue and D.G. Porter. *OOMMF User's Guide, Version 1.0, Interagency Report NISTIR, National Institute of Standards and Technology, Gaithersburg, MD* **6376**, http://math.nist.gov/oommf (1999)

[EH06] R. Engel-Herbert, D. M. Schaadt and T. Hesjedal. Analytical and numerical calculations of the magnetic force microscopy response: A comparison. *J. Appl. Phys.* **99**, 113905 (2006)

[Esc07] J. Escrig, D. Altbir, M. Jaafar, D. Navas, A. Asenjo and M. Vázquez. Remanence of Ni nanowire arrays: Influence of size and labyrinth magnetic structure. *Phys. Rev. B* **75**, 184429 (2007)

[Esc08] J. Escrig, R. Lavin, J.L. Palma, J. C. Denardin, D. Altbir, A. Cortes and H. Gomez. Geometry dependence of coercivity in Ni nanowire arrays. *Nanotechnology* **19** (2008)

[Fol00] L. Folks, M. E. Best, P. M. Rice, B. D. Terris, D. Weller and J. N. Chapman. Perforated tips for high-resolution in-plane magnetic force microscopy. *Appl. Phys. Lett.* **76**, 909 (2000)

[Gar01] J. M. Garcia, A. Thiaville, J. Miltat, K. J. Kirk, J. N. Chapman and F. Alouges. Quantitative interpretation of magnetic force microscopy images from soft patterned elements. *Appl. Phys. Lett.* **79**, 656 (2001)

[Gar02] R. Garcia and R. Pérez. Dynamic force microscopy methods. *Surf. Sci. Rep.* **47**, 197 (2002)

[Gha11] A. Ghaddar, F. Gloaguen, J. Gieraltowski and C. Tannous. Magnetic crossover effect in Nickel nanowire arrays. *Physica B* **406**, 2046 (2011)

[GM04] J.M. Garcia-Martin, A. Thiaville, J. Miltat, T. Okuno and L. Vila. Imaging magnetic vortices by magnetic force microscopy: experiments and modelling. *J.Phys. D: Appl. Phys.* **37**, 965 (2004)

[Gri98] M. Grimsditch, Y. Jaccard and I.K. Schuller. Magnetic anisotropies in dot arrays: Shape anisotropy versus coupling. *Phys. Rev. B* **58**, 11539 (1998)

[Grü90] P. Grütter, D. Rugar, H.J. Mamin, G. Castillo, S.E. Lambert, C.-J. Lin, R.M. Valletta, O. Wolter, T. Bayer and J. Greschner. Batch fabricated sensors for magnetic force microscopy. *Appl. Phys. Lett.* **57**, 1820 (1990)

[Grü92] P. Grütter, H. J. Mamin and D. Rugar. *Scanning Tunneling Microscopy II.* Springer Series in Surface Sciences 2nd edn. Springer-Verlag (1992)

[Häb12] T. Häberle, F. Hering, H. Pfeifer, L. Han, B. Kuerbanjiang, U. Wiewald, U. Herr and B. Koslowski. Towards quantitative magnetic force microscopy: theory and experiment. *New Journ. Phys.* **14**, 043044 (2012)

[Häh10] G. Hähner. Dynamic spring constants for higher flexural modes of cantilever plates with applications to atomic force microscopy. *Ultramicroscopy* **110**, 801 (2010)

[HAN98] *Handbook Dimension 3100.* Digital Instruments Inc. (1998)

[Har89] U. Hartmann. The point dipole approximation in magnetic force microscopy. *Phys. Lett. A* **137**, 475 (1989)

[Har90] U. Hartmann. Manifestation of zero-point quantum fluctuations in atomic force microscopy. *Phys. Rev. B* **42**, 1541 (1990)

[Har91] U. Hartmann. Van der Waals interactions between sharp probes and flat sample surfaces. *Phys. Rev. B* **43**, 2404 (1991)

[Har94] U. Hartmann. Fundamentals and Special Applications of Non-contact Scanning Force Microscopy. In: P. W. Hawkes (Ed.), *Advances in Electronics and Electron Physics*, Vol. 87. Academic Press Inc. (1994)

[Has06] C. Hassel, M. Brands, F. Y. Lo, A. D. Wieck and G. Dumpich. Resistance of a Single Domain Wall in $(Co/Pt)_7$ Multilayer Nanowires. *Phys. Rev. Lett.* **97**, 226805 (2006)

[Has10] K. Hashimoto, M. Yamashita, S. Kasahara, Y. Senshu, N. Nakata, S. Tonegawa, K. Ikada, A. Serafin, A. Carrington and T. Terashima. Line nodes in the energy gap of superconducting $BaFe_2(As_{1-x}P_x)_2$ single crystals as seen via penetration depth and thermal conductivity. *Phys. Rev. B* **81**, 220501 (2010)

[Hel07] O. Hellwig, A. Berger, J. B. Kortright and E. E. Fullerton. Domain structure and magnetization reversal of antiferromagnetically coupled perpendicular anisotropy films. *J. Magn. Magn. Mater.* **319**, 13 (2007)

[Hel13] O. Hellwig, L. J. Heyderman, O. Petracic and H. Zabel. *Magnetic Nanostructures*, Vol. 246. Springer-Verlag (2013)

[Her02] R. Hertel. Computational micromagnetism of magnetization processes in nickel nanowires. *J. Magn. Magn. Mater.* **249**, 251 (2002)

[Her04] R. Hertel and J. Kirschner. Magnetization reversal dynamics in nickel nanowires. *Physica B* **343**, 206 (2004)

[Hub97] A. Hubert, W. Rave and S. L. Tomlinson. Imaging Magnetic Charges with Magnetic Force Microscopy. *Phys. Status Solidi B* **204**, 817 (1997)

[Hub98] A. Hubert and R. Schaefer. *Magnetic Domains*. Springer-Verlag (1998)

[Huc99] A. Hucht. *Temperaturabhängigkeit magnetischer Anisotropien in ultradünnen Filmen*. Dissertation, Universität Duisburg-Essen, Fakultät für Physik (1999)

[Hug98] H. J. Hug, B. Stiefel, P. J.A. van Schendel, A. Moser, R. Hofer, S. Martin, H. J. Güntherodt, S. Porthun, L. Abelmann, G. Bochi and R. C. O'Handley. Quantitative magnetic force microscopy on perpendicularly magnetized samples. *J. Appl. Phys.* **83**, 5609 (1998)

[Ish89] Y. Ishii and M. Sato. Magnetic behavior of a film with columnar structure. *J. Magn. Magn. Mat.* **82**, 309 (1989)

[Jaa08] M. Jaafar, A. Asenjo and M.Vázquez. Calibration of coercive and stray fields of commercial magnetic force microscope probes. *IEEE Trans. Nanotech.* **7**, 245 (2008)

[Jac75] J.D. Jackson. *Classical Electrodynamics*. J. Wiley and Sons, New York (1975)

[Kap03] P. Kappenberger, S. Martin, Y. Pellmont, H. J. Hug, J. B. Kortright, O. Hellwig and E. E. Fullerton. Direct imaging and determination of the uncompensated spin density in exchange-biased CoO/(CoPt) multilayers. *Phys. Rev. Lett.* **91**, 267202 (2003)

[Kap05a] P. Kappenberger. *Exchange bias effect and hard disk media studied by means of quantitative magnetic force microscopy.* PhD Thesis, University of Basel, Faculty of Science (2005)

[Kap05b] P. Kappenberger, I. Schmid and H. J. Hug. Investigation of the exchange bias effect by quantitative magnetic force microscopy. *Adv. Eng. Mater.* **7**, 332 (2005)

[Keb04] Th. Kebe and A. Carl. Calibration of magnetic force microscopy tips by using nanoscale current-carrying parallel wires. *J. Appl. Phys.* **95**, 775 (2004)

[Kim12] J. Kim, L. Civale, E. Nazaretski, N. Haberkorn, F. Ronning, A.S. Sefat, T. Tajima, B.H. Moeckly, J.D. Thompson and R. Movshovich. Direct measurement of the magnetic penetration depth by magnetic force microscopy. *Supercond. Sci. Technol.* **25**, 112001 (2012)

[Kir12] V. Kireev, R.S. Khymyn, B.A. Ivanov and C.E. Zaspel. Ground states and magnetization process for a triangular lattice array of magnetic dots with perpendicular anisotropy. *arXiv:1201.1747v1[cond-mat-mtrl-sci]* (2012)

[Kis08] N.S. Kiselev, I.E. Dragunov, V. Neu, U.K. Rößler and A.N. Bogdanov. Theoretical analysis of magnetic force microscopy contrast in multidomain states of magnetic superlattices with perpendicular anisotropy. *Journ. Appl. Phys.* **103**, 043907 (2008)

[Kis11] N. Kiselev. private communications (2011)

[Kli01] B. Klingen. *Fouriertransformation für Ingenieur- und Naturwissenschaften.* Springer-Verlag (2001)

[Kon97] L. Kong and S. Y. Chou. Quantification of magnetic force microscopy using a micronscale current ring. *Appl. Phys. Lett.* **70**, 2043 (1997)

[Koo60] C. Kooy and U. Enz. Experimental and theoretical study of the domain configuration in thin layers of $BaFe_{12}O_{19}$. *Philips Res. Rep.* **15**, 181 (1960)

[Kro87] H. Kronmüller. Theory of nucleation fields in inhomogeneous ferromagnets. *Phys. Status Solidi B* **144**, 385 (1987)

[Kum06] A. Kumar, S. Fähler, H. Schlörb, K. Leistner and L. Schultz. Competition between shape anisotropy and magnetoelastic anisotropy in Ni nanowires electrodeposited within alumina templates. *Phys. Rev. B* **73**, 064421 (2006)

[Lam93] Ph. Lambin and P. Senet. Ewald summation of multipolar interactions at an arbitrary order on a two-dimensional lattice. *Int. J. Quant. Chem.* **46**, 101 (1993)

[Lim10] S.L. Lim, F. Xu, N.N. Phuoc and C.K. Ong. Length dependence of coercivity in $CoFe_2$ nanowire arrays with high aspect ratios. *J. Alloys Compd.* **505**, 609 (2010)

[Loh99] J. Lohau, S. Kirsch, A. Carl, G. Dumpich and E. F. Wassermann. Quantitative determination of effective dipole and monopole moments of magnetic force microscopy tips. *J. Appl. Phys.* **86**, 3410 (1999)

[Loh00] J. Lohau, S. Kirsch, A. Carl and E. F. Wassermann. Quantitative determination of the magnetization and stray field of a single domain Co/Pt dot with magnetic force microscopy. *Appl. Phys. Lett.* **76**, 3094 (2000)

[Loh01] J. Lohau, A. Carl, S. Kirsch and E. F. Wassermann. Magnetization reversal and coercivity of a single-domain Co/Pt dot measured with a calibrated magnetic force microscope tip. *Appl. Phys. Lett.* **78**, 2020 (2001)

[Lua09] L. Luan, O. M. Auslaender, D. A. Bonn, R. Liang, W. N. Hardy and K. A. Moler. Magnetic force microscopy study of interlayer kinks in individual vortices in the underdoped cuprate superconductor $YBa_2Cu_3O_{6+x}$. *Phys. Rev. B* **79**, 214530 (2009)

[Lua10] L. Luan, O. M. Auslaender, T. M. Lippman, C. W. Hicks, B. Kalisky, J.-H. Chu, J. G. Analytis, I. R. Fisher, J. R. Kirtley and K. A. Moler. Local measurement of the penetration depth in the pnictide superconductor $Ba(Fe_{0.95}Co_{0.05})_2As_2$. *Phys. Rev. B* **81**, 1–4 (2010)

[Lua11] L. Luan, T. M. Lippman, C. W. Hicks, J. A. Bert, O. M. Auslaender, J.-H. Chu, J. G. Analytis, I. R. Fisher and K. A. Moler. Local Measurement of the Superfluid Density in the Pnictide Superconductor Ba $(Fe_{1-x}$ Co $_x)_2As_2$ across the Superconducting Dome. *Phys. Rev. Lett.* **106**, 067001 (2011)

[Mad96] R. Madabhushi, R. D. Gomez, E. R. Burke and I. D. Mayergoyz. Magnetic Biasing and MFM image reconstruction. *IEEE Trans. Magn.* **32**, 4147 (1996)

[Mag97] S.N. Magonov, V. Elings and M.-H. Whangbo. Phase imaging and stiffness in tapping-mode atomic force microscopy. *Surface Science* **375**, L385 (1997)

[Mam88] H. J. Mamin, D. Rugar, J. E. Stern, B. D. Terris and S. E. Lambert. Force microscopy of magnetization patterns in longitudinal recording media. *Appl. Phys. Lett.* **53**, 1563 (1988)

[Mar06] M. A. Marioni, N. Pilet, T. V. Ashworth, R. C. O'Handley and H. J. Hug. Remanence due to wall magnetization and counterintuitive magnetometry data in 200 nm films of Ni. *Phys. Rev. Lett.* **97** (2006)

[Mas87] M. Masuda, S. Shiomi and M. Shiraki. Magnetostatic perpendicular anisotropy in iron films with columnar structure. *Jpn. J. Appl. Phys. 1* **26**, 1680–1689 (1987)

[MAT] software: Wolfram Mathematica. *1998-2009 Wolfram Research Inc.* **7.0**

[McV01a] S. McVitie, R. P. Ferrier, J. Scott, G. S. White and A. Gallagher. Quantitative field measurements from magnetic force microscope tips and comparison with point and extended charge models. *J. Appl. Phys.* **89**, 3656 (2001)

[McV01b] S. McVitie, G. S. White, J. Scott, P. Warin and J. N. Chapman. Quantitative imaging of magnetic domain walls in thin films using Lorentz and magnetic force microscopies. *J. Appl. Phys.* **90**, 5220 (2001)

[Mey04] E. Meyer, H. J. Hug and R. Bennewitz. *Scanning Probe Microscopy.* Springer-Verlag Berlin Heidelberg (2004)

[Müh12] T. Mühl, J. Körner, S. Philippi, C. F. Reiche, A. Leonhardt and B. Büchner. Magnetic force microscopy sensors providing in-plane and perpendicular sensitivity. *Appl. Phys. Lett.* **101**, 1124011 (2012)

[Nan11] NanoScan AG, Switzerland. *High-Resolution Magnetic Force Microscope* (2011)

[Naz09] E. Nazaretski, J. P. Thibodaux, I. Vekhter, L. Civale, J. D. Thompson and R. Movshovich. Direct measurements of the penetration depth in a superconducting film using magnetic force microscopy. *Appl. Phys. Lett.* **95** (2009)

[Net90] U. Netzelmann. Ferromagnetic resonance of particulate magnetic recording tapes. *J. Appl. Phys.* **68**, 1800 (1990)

[Nie01] K. Nielsch, R.B. Wehrspohn, J. Barthel, J. Kirschner, U. Gosele, S.F. Fischer and H. Kronmüller. Hexagonally ordered 100 nm period nickel nanowire arrays. *Appl. Phys. Lett.* **79**, 1360 (2001)

[Nie02] K. Nielsch, R.B. Wehrspohn, J. Barthel, J. Kirschner, S.F. Fischer, H. Kronmüller, T. Schweinböck, D. Weiss and U. Gösele. High density hexagonal nickel nanowire array. *J. Magn. Magn. Mat.* **249**, 234 (2002)

[Nie07] K. Nielsch and B.J. H. Stadler. Template-based Synthesis and Characterization of High-density Ferromagnetic Nanowire Arrays. *Handbook of Magnetism and Advanced Magnetic Materials* (2007)

[Oti93] J. O. Oti. Numerical micromagnetic techniques and their applications to magnetic force microscopy calculations. *IEEE Trans. Magn.* **29**, 2359 (1993)

[Ovc01] D. V. Ovchinnikov and A. A. Bukharaev. Computer simulation of magnetic force microscopy images with a static model of magnetization distribution and dipole-dipole interaction. *Tech. Phys.* **46**, 1014 (2001)

[Pil06] N. Pilet. *The relation between magnetic hysteresis and the micromagnetic state explored by quantitative magnetic force microscopy.* PhD Thesis, University of Basel, Faculty of Science (2006)

[Pil07] N. Pilet, T. V. Ashworth, M. A. Marioni, H. J. Hug, K. Zhang and K. P. Lieb. Effect of ion irradiation on domain nucleation and wall motion in Ni films. *J. Magn. Magn. Mater.* **316**, 583 (2007)

[Por98] S. Porthun, L. Abelmann and C. Lodder. Magnetic force microscopy of thin film media for high density magnetic recording. *J. Magn. Magn. Mater.* **182**, 238 (1998)

[Pre92] W. H. Press, S. A. Teukolsky, W. T. Vetterling and B. P. Flannery. *Numerical Recipes in C-The art of scientific computing.* Cambridge University Press (1992)

[Rap00] V. Raposo, J.M. Garcia, J.M. González and M. Vázquez. Long-range magnetostatic interactions in arrays of nanowires. *J. Magn. Magn. Mat.* **222**, 227 (2000)

[Rei13] C.F. Reiche, S. Vock, T. Mühl, V. Neu, D. Makarov, L. Schultz and B. Büchner. Monopole type behavior of iron filled carbon nanotubes confirmed in two dimensions by bimodal quantitative magnetic force microscopy. *to be published* (2013)

[Rhe13] F. Rhein. *Direkte Bestimmung physikalischer Eigenschaften supraleitender Materialien mittels Entfaltung magnetkraftmikroskopischer Bilddaten.* Diploma-Thesis, Fachbereich Physik, Fakultät Mathematik und Naturwissenschaften, Technische Universität Dresden (2013)

[Riv02] J. Rivas, A. Kazadi Mukenga Bantu, G. Zaragoza, M.C. Blanco and M.A. López-Quintela. Preparation and magnetic behavior of arrays of electrodeposited Co nanowires. *J. Magn. Magn. Mat.* **249**, 220 (2002)

[Ros01] M Roseman and P Grütter. Estimating the magnetic penetration depth using constant-height magnetic force microscopy images of vortices. *New J. Phys.* **3**, 24 (2001)

[Rot12] T. Rothman. Die Physik - ein baufälliger Turm von Babel. *Spektrum der Wissenschaft* **12**, 61 (2012)

[Rug90] D. Rugar, H.J. Mamin, P. Guethner, S.E. Lambert, J.E. Stern, I. McFadyen and T. Yogi. Magnetic force microscopy: General principles and application to longitudinal recording media. *J. Appl. Phys.* **68**, 1169 (1990)

[Rus01] A.W. Rushforth, P.C. Main, B.L. Gallaghera, C.H. Marrows, B.J. Hickey, E.D. Dahlberg and P. Eames. Magnetic force microscopy studies of the domain structure of CoPd multilayers in a magnetic field. *J. Appl. Phys.* **89** (2001)

[Sae87] J. J. Saenz, N. Garcia, P. Grütter, E. Meyer, H. Heinzelmann, R. Wiesendanger, L. Rosenthaler, H. R. Hidber and H. J. Güntherodt. Observation of magnetic forces by the atomic force microscope. *J. Appl. Phys.* **62**, 4293 (1987)

[Sam92] E.O. Samwel, P.R. Bissell and J.C. Lodder. Internal field corrections in perpendicular columnar structured aluminite films. *J. Magn. Magn. Mat.* **115**, 327 (1992)

[Sar91] D. Sarid. *Scanning Force Microscopy With Applications to Electric, Magnetic, and Atomic Force.* Oxford series in optical and imaging sciences. Oxford University Press Inc., New York (1991)

[Sas05] S. Sasvári. *Bestimmung komplexer Magnetisierungsverteilungen mittels vektorieller Magnetkraftmikroskopie.* Diploma-Thesis, Fakultät Maschinenwesen, Technische Universität Dresden (2005)

[Sas13a] Z. Sasvári. *private communications* (2013)

[Sas13b] Z. Sasvári. internet source: SigMath. *http://sig.math.tu-dresden.de/index-german.shtml* **1.070** (2013)

[Sch90] C. Schönenberger and S. F. Alvarado. Understanding magnetic force microscopy. *Z. Phys. B: Condens. Matter* **80**, 373 (1990)

[Sch08] I. Schmid. *The role of uncompensated spins in exchange biased systems.* PhD Thesis, University of Basel, Faculty of Science (2008)

[Sch10a] H. Schlörb, V. Hähnel, M. Singh Khatri, A. Srivastav, A. Kumar, L. Schultz and S. Fähler. Magnetic nanowires by electrodeposition within templates. *Phys. Status Solidi B* **247**, 2364 (2010)

[Sch10b] I. Schmid, M.A. Marioni, P. Kappenberger, S. Romer, M. Parlinska-Wojtan, H.J. Hug, O. Hellwig, M. J. Carey and E.E. Fullerton. Exchange bias and domain evolution at 10 nm scales. *Phys. Rev. Lett.* **105**, 197201 (2010)

[Sel01] D. J. Sellmyer, M. Zheng and R. Skomski. Magnetism of Fe, Co and Ni nanowires in self-assembled arrays. *J. Phys.: Condens. Matter* **13**, R433 (2001)

[SH94] A. Kikukawa S. Hosaka and Y. Honda. High Resolution of Magnetic Force Microscope Image using a Just-on-Surface Magnetic Force Microscope. *Jpn. J. Appl. Phys.* **33**, 3779 (1994)

[Sha10a] T. Shapoval. *Local imaging of magnetic flux in superconducting thin films*. Dissertation, Fachbereich Physik, Fakultät Mathematik und Naturwissenschaften, Technische Universität Dresden (2010)

[Sha10b] T. Shapoval, V. Metlushko, M. Wolf, V. Neu, B. Holzapfel and L. Schultz. Enhanced pinning of superconducting vortices at circular magnetic dots in the magnetic-vortex state. *Physica C* **470**, 867 (2010)

[Sha11] T. Shapoval, H. Stopfel, S. Haindl, J. Engelmann, D.S. Inosov, B. Holzapfel, V. Neu and L. Schultz. Quantitative assessment of pinning forces and magnetic penetration depth in NbN thin films from complementary magnetic force microscopy and transport measurements. *Phys. Rev. B* **83**, 214517 (2011)

[Shi00] T. Shinjo, T. Okuno, R. Hassdorf, K. Shigeto and T. Ono. Magnetic Vortex Core Observation in Circular Dots of Permalloy. *Science* **289**, 930 (2000)

[Sib05] J. B. Sibarita. Deconvolution microscopy. *Microscopy Techniques* **95**, 201–243 (2005)

[Sko01] R. Skomski and D. J. Sellmyer. Cooperative magnetism and the Preisach model. *J. Appl. Phys.* **89**, R841 (2001)

[Sko03] R. Skomski. Nanomagnetics. *J.Phys.:Condens.Matter* **15**, 7263 (2003)

[Sti10] H. Stillrich, C. Menk, R. Fromter and H. P. Oepen. Magnetic anisotropy and spin reorientation in Co/Pt multilayers: Influence of preparation. *J. Magn. Magn. Mater.* **322**, 1353–1356 (2010)

[Sto11] H. Stopfel. *Quantitative magnetische Kraftmikroskopie zur Untersuchung von Flusslinienanordnung und deren Eigenschaften*. Diploma-Thesis, Fachbereich Physik, Fakultät Mathematik und Naturwissenschaften, Technische Universität Dresden (2011)

[Str99] G.J. Strijkers, J.H.J. Dalderop, M.A.A. Broeksteeg, H.J.M. Swagten and W.J.M. De Jonge. Structure and magnetization of arrays of electrodeposited Co wires in anodic alumina. *J. Appl. Phys.* **86**, 5141 (1999)

[Str08] E. W. J. Straver, J. E. Hoffman, O. M. Auslaender, D. Rugar and K. A. Moler. Controlled manipulation of individual vortices in a superconductor. *Appl. Phys. Lett.* **93**, 172514 (2008)

[Suc09] S. Y. Suck, V. Neu, U. Wolff, S. Bahr, O. Bourgeois and D. Givord. Magnetic force microscopy analysis of magnetization reversal in exchange-biased Co/CoO nanostructure arrays. *Appl. Phys. Lett.* **95**, 162503 (2009)

[Sun05] L. Sun, Y. Hao, C.-L. Chien and P.C. Searson. Tuning the properties of magnetic nanowires. *IBM J. Res. Dev.* **49**, 79 (2005)

[Thi70] A. A. Thiele. Theory of Static Stability of Cylindrical Domains in Uniaxial Platelets. *J. Appl. Phys.* **41**, 1139 (1970)

[Tip00] P.A. Tipler. *Physik*. Spektrum Akademischer Verlag Heidelberg Berlin Oxford (2000)

[Tom97] S. L. Tomlinson and A. N. Farley. Micromagnetic model for magnetic force microscopy tips. *J. Appl. Phys.* **81**, 5029 (1997)

[Váz04] M. Vázquez, K. Nielsch, P. Vargas, J. Velázquez, D. Navas, K. Pirota, M. Hernández-Vélez, E. Vogel, J. Cartes, R.B. Wehrspohn u.ã. Modelling hysteresis of interacting nanowires arrays. *Physica B: Condensed Matter* **343**, 395–402 (2004)

[Váz05] M. Vázquez, K. Pirota, J. Torrejon, D. Navas and M. Hernandez-Velez. Magnetic behaviour of densely packed hexagonal arrays of Ni nanowires: Influence of geometric characteristics. *Journal of magnetism and magnetic materials* **294**, 174–181 (2005)

[Váz11] M. Vázquez and L.G. Vivas. Magnetization reversal in Co-base nanowire arrays. *Phys. Stat. Sol. B* **248**, 2368 (2011)

[Vel98] B. Vellekoop, L. Abelmann, S. Porthun and C. Lodder. On the determination of the internal magnetic structure by magnetic force microscopy. *J. Magn. Magn. Mater.* **190**, 148 (1998)

[Viv12] L.G. Vivas, M. Vázquez, J. Escrig, S. Allende, D. Altbir, D.C. Leitao and J.P. Araujo. Magnetic anisotropy in CoNi nanowire arrays: Analytical calculations and experiments. *Phys. Rev. B* **85**, 035439 (2012)

[Voc10] S. Vock, F. Wolny, T. Mühl, R. Kaltofen, L. Schultz, B. Büchner, C. Hassel, J. Lindner and V. Neu. Monopolelike probes for quantitative magnetic force microscopy: Calibration and application. *Appl. Phys. Lett.* **97**, 252505 (2010)

[Voc11] S. Vock, Z. Sasvári, C. Bran, F. Rhein, U. Wolff, N. S. Kiselev, A.N. Bogdanov, L. Schultz, O. Hellwig and V. Neu. Quantitative Magnetic Force Microscopy Study of the Diameter Evolution of Bubble Domains in a Co-Pd Multilayer. *IEEE Trans. Magn.* **47**, 2352 (2011)

[vS99] P. J. A. van Schendel. *Investigation of magnetization structures in ferromagnetic and superconducting samples by magnetic force microscopy.* PhD Thesis, University of Basel, Faculty of Science (1999)

[vS00] P. J. A. van Schendel, H. J. Hug, B. Stiefel, S. Martin and H. J. Güntherodt. A method for the calibration of magnetic force microscopy tips. *J. Appl. Phys.* **88**, 435 (2000)

[VSM13] http://www.qdusa.com/products/ppms.html. (2013)

[Was02] E. F. Wassermann, C. Bürgel, A. Carl and J. Lohau. Magnetization measurements on the nanometer-scale. *J. Magn. Magn. Mater.* **239**, 220 (2002)

[Wei08] T. Weis, I. Krug, D. Engel, A. Ehresmann, V. Hoink, J. Schmalhorst and G. Reiss. Characterization of magnetic force microscopy probe tip remagnetization for measurements in external in-plane magnetic fields. *J. Appl. Phys.* **104**, 123503 (2008)

[Wha98] M.-H. Whangbo, G. Bar and R. Brandsch. Description of phase imaging in tapping mode atomic force microscopy by harmonic approximations. *Surface Science* **411**, L794 (1998)

[Wie42] N. Wiener. *The interpolation, extrapolation and smoothing of stationary time series'.* Report of the Services 19, Research Project DIC-6037 MIT (1942)

[WIK13] http://de.wikipedia.org/wiki/Heaviside-Funktion. (2013)

[Wil49] H. J. Williams, R. M. Bozorth and W. Shockley. Magnetic Domain Patterns on Single Crystals of Silicon Iron. *Phys. Rev.* **75**, 155 (1949)

[Win06] A. Winkler, T. Mühl, S. Menzel, R. Kozhuharova-Koseva, S. Hampel, A. Leonhardt and B. Büchner. Magnetic force microscopy sensors using iron-filled carbon nanotubes. *J. Appl. Phys.* **99**, 104905 (2006)

[Wol08] F. Wolny, U. Weissker, T. Mühl, A. Leonhardt, S. Menzel, A. Winkler and B. Büchner. Iron-filled carbon nanotubes as probes for magnetic force microscopy. *J. Appl. Phys.* **104**, 064908 (2008)

[Wol10] F. Wolny, T. Mühl, U. Weissker, K. Lipert, J. Schumann, A. Leonhardt and B. Büchner. Iron filled carbon nanotubes as novel monopole-like sensors for quantitative magnetic force microscopy. *Nanotechnology* **21**, 435501 (2010)

[Wri95] C. D. Wright and E. W. Hill. Reciprocity in magnetic force microscopy. *Appl. Phys. Lett.* **67**, 433 (1995)

[Zen00] H Zeng, M Zheng, R Skomski, DJ Sellmyer, Y Liu, L Menon and S Bandyopadhyay. Magnetic properties of self-assembled Co nanowires of varying length and diameter. *J. Appl. Phys.* **87**, 4718 (2000)

[Zhu98] J.-G. Zhu, X. Lin and R. C. Shi. Magnetic force microscopy image restoration technique for removing tip dependence. *J. Appl. Phys.* **83**, 6223 (1998)

[Zie82] A. Zieba and S. Foner. Detection coil, sensitivity function, and sample geometry effects for vibrating sample magnetometers. *Rev. Sci. Instrum.* **53**, 1344 (1982)

[Zue99] E. Zueco. *Magnetic Domain Studies by combined Kerr/Magnetic Force Microscopy.* PhD thesis, Technical University Dresden, Faculty of Mathematics and Natural Sciences (1999)

## Acknowledgements

First of all, I thank Prof. Ludwig Schultz for giving me the opportunity to carry out my Phd work at the IFW Dresden. His passion for science caught me already as a young pupil and continued to inspire me during my academic and scientific studies. He continuously supported and encouraged me throughout the years. I acknowledge very much that he, despite his time consuming position as a director of the IFW, still took the time to listen and to think about the different kind of problems, which occurred during my work.

I would like to express my thanks to my direct supervisor Dr. Volker Neu for his scientific guidance. His open office door always conveyed the feeling that scientific discussions were welcome, even if they were of unpredictable length. I can not remember a single occasion where I had to wait with the communication of an exciting idea or an unsolvable problem. In the same time I would like to thank my father Prof. Zoltán Sasvári, who not only provided the powerful development environment SigMath used for all numerical applications in this work but also contributed with numerous programming hints and mathematical suggestions.

I thank Prof. Manuel Vázquez for the interest in my work and his readiness to co-referee this thesis.

I would like to thank Dr. Marietta Seifert and Dr. Ulrike Wolff for the critical proofreading of the manuscript. Fabian Rhein and Henry Stopfel I would like to thank for the good collaboration concerning the evaluation of MFM data of vortices in superconductors. Additionally, I would like to thank Fabian Rhein for helping me with time consuming measurements and evaluations during his time as a student assistant in our group. I also thank all the other past and present members of the SFM group who contributed to this work with discussions, suggestions and by creating a nice working environment: Katja Berger, Dr. Cristina Bran, Benjamin Schleicher and Dr. Tanya Shapoval.

I thank our head of the department Dr. Rudolf Schäfer and all past and present members of the department 24 who contributed with critical questions and ideas during our monday meeting.

I would like to thank Claudia Hengst and Dr. Manfred Wolf for conducting the micromagnetic simulations and for the fruitful discussion of the results.

I thank Dr. Nikolai Kiselev for his patience in explaining to me how magnetostatic expressions can be derived in Fourier space. I thank Dr. Ulrich Rößler for helpful discussions concerning the demagnetizing fields in nanowire arrays.

The cooperation with the group of Dr. Thomas Mühl at the IFF I experienced as very valuable for my work. I would especially like to thank Dr. Franziska Wolny and Christopher Reiche for the good collaboration.

I would like to thank all those, who provided interesting samples and physical questions for the investigation by quantitative MFM: Dr. Olav Hellwig (Co/Pd multilayers), Dr. Denys Makarov (Co/Pt multilayers for use as reference samples), Dr. Christoph Hassel (patterned Co/Pt stripes as reference samples), Prof. Dmytro S. Inosov (superconducting iron pnictides), Dr. Margitta Uhlemann, Dr. Kristina Tschulik and Kerstin Hennig (CoFe nanowires).

I thank Prof. Hans-Josef Hug for his hospitality in Basel and Dübendorf, the opportunity for low temperature MFM measurements at his institute together with the members of his group and for coming to Dresden for detailed discussions. He shared his knowledge about MFM theory with me and gave useful methodological hints for my work.

Dr. Sebastian Fähler I wish to thank for discussions and hints concerning the evaluation of magnetostatic interactions in nanowire arrays.

I am very grateful to my close friend and colleague Dr. Karin Leistner for accompanying me trough the depths and heights of scientific work. My dear office mates Cristina Bran and Elena Lopatina are also acknowledged for the pleasant working environment which was always present in our room.

Finally, this is the part where I would like to thank my family, especially my husband Alexander and my parents Evelyne and Zoltán Sasvári. However, I feel that I am lacking the words to really express my gratitude for their help and support throughout the years.